Irradiation and nanostructuration of piezoelectric polymers for nano-sensoring and harvesting energy applications.

Giuseppe Melilli

NNT : 2017SACLX072

Thèse de doctorat de l'Université Paris-Saclay préparée École polytechnique

Ecole doctorale n°573
Approches inderdisciplinares, fondements, applications et innovation
Spécialité de doctorat : physique

par

Giuseppe Melilli

Piezoelectric nanostructured Ni/PVDF hybrid film synthesized from swift-heavy ions irradiation:
direct and indirect piezoelectric response study

Thèse présentée et soutenue à "Palaiseau", le 26 octobre 2017.

Composition du Jury :

M.	Emmanuel Balanzat	Doctor CIMAP-GANIL	(Président du jury)
Mme.	Sylvie Tencé-Girault	Doctor ESPCI Paris	(Rapporteur)
M.	Xavier Coqueret	Professor Université de Reims	(Rapporteur)
M.	Marco Sangermano	Professor Politecnico di Torino	(Examinateur)
Mme.	Marie-Claude Clochard	Doctor CEA saclay	(Directrice de thèse)
M.	Jean-Eric Wegrowe	Professor École polytechnique	(Co-Directeur de thèse)
M.	Giancarlo Rizza	Doctor CEA Saclay	(Invité)

Contents

ii

List of Figures

List of Tables

Chapter 1

Context

1.1 Piezoelectric polymers

Poly(vinylidene fluoride) (PVDF), is one of the most attractive semi-crystalline polymer owing to its remarkable ferroelectric properties. Piezoelectric phenomenon represents one of the most important peculiarities of the ferroelectric materials; it is defined as the aptitude to convert mechanical strain in electrical charge (direct piezoelectric effect) and vice versa (inverse piezoelectric effect).

Since the discovery of the piezoelectric properties of PVDF in 1969, [1] many sensors and actuators have been developed. In the recent years the direct piezoelectric effect in PVDF has experienced a resurgence of interest for energy harvesting. The main purpose of energy harvesting is to involve energy source, naturally replenished, to recover electrical energy. Using piezoelectric PVDF, the primary sources are represented by any form of mechanical deformation or vibration. The vibrational energy may have various origins such as body movements, sound, hydraulic movements, wind, friction.[2–7] Piezomaterials based on polymers such as PVDF can offer flexibility and robustness that is required to develop portable microelectronic devices. Indeed, the advent of extremely low power electrical and mechanical devices (e.g., microelectromechanical systems or MEMS) makes such generators attractive in several applications where remote power is required. Such applications are referred to as power scavenging, including *in vivo* sensors and embedded MEMS devices. [8, 9] Although PVDF energy conversion efficiency is generally lower than that of other piezoelectric materials (e.g. PZT), it has the advantage that it can generate an electric signal under large reversible elastic deformation. Most of techniques used to make PVDF more competitive involving multilayer of PVDF films,[4, 10] or nanostructuration. As examples we may cite semiconductor nanowires (NWs) presenting piezoelectric properties embedded in a PVDF matrix.[2] Recent studies in PVDF composite materials suggest to exploit the interfacial polarization i.e. the Maxwell-Wagner-Sillars effect. Indeed, heterogeneity in polymer matrix introduces additionally

interfacial polarization. As a result the dielectric permittivity increases.[11] Typical examples are composite PVDF- PZT, [12] PVDF-NiO nanosheet.[13]
High irradiation energy may be another competitive way to modify the structure of the piezoelectric polymer to enhance the piezoelectric response.

1.2   Irradiation in piezoelectric PVDF and P(VDF-TrFE)

High irradiation energy lead to large modifications in the physical and chemical properties of polymers. Ionizing radiations are composed of photons (gamma or X-rays, bremsstrahlung), accelerated particles (electrons, light ions, swift heavy ions (SHI)), and particles ejected from radioactive emitters (α and $\beta-$ particles). The deposited energy in the target material through various interaction processes depends on the radiation type and its energy. [14] The energies deposited by ionizing radiations are several orders of magnitude higher than that of any chemical bond. Therefore any molecule present in the material can absorb radiation energy. Consequently, in contrast with ultraviolet radiations, there are neither sensitive nor specific absorbing chemical groups. The amount of modifications related to the high energy irradiation involves i) radioactive decay, ii)production of new reactive species (radicals, gas) and defects (unsaturations chain, scissions, crosslinking). [15] The first studies, about polymer irradiation, have been mostly motivated by nuclear plants (NPPs) concerns about degradation, corrosion and ageing. The radiation chemistry of polymers was founded in 1940s by the pioneering works of Magat and Chapiro on radiation induced polymerization and grafting in France, and of Charlesby on polyethylene irradiation in United Kingdom. For a following decade, the radiation crosslinking of polyethylene was intensively investigated by Karpov in USSR and by Dole in the USA. These depth studies have put the foundations of a science still active today including radiation processes into industry. Technological applications are nowadays numerous exploiting the irradiated polymer properties such as crosslinking, post-synthesis molecular weight control of thermoplastic polymers, polymerization and curing, grafting, ion track technology, polymer-based pharmaceutical systems and medical devices and art conservation science. [14]
In this study, two types of ionizing radiations will be used: e-beam and SHI. As a general rule, whatever the ionizing radiation type, two different interactions should be considered: i) electronic interaction and ii) nuclear interaction. Excited molecules created either by direct effect of the irradiation or after charge recombination undergo homolytic bond ruptures to give radicals. These radicals can

migrate along the polymer chains. This migration is fast and occurs in the microseconds to second timescale. [16] Radicals can readily recombine or react with the polymer to give stables products (mostly unsaturations) or other radicals. In case of semi-crystalline PVDF and related compounds such as poly(vinylidene difluoride-co-trifluoroethylene) P(VDF-TrFE), radical migration stop in the crystalline regions where they are trapped. [17] PVDF and P(VDF-TrFE) are the most industrially used piezoelectric polymers. P(VDF-TrFE) improves the piezoelectric response by improving the crystallinity of the material. d_{33} values for P(VDF-TFE) have been recorded to be as high as -38 pC.N^{-1} versus -33 pC.N^{-1}in pure PVDF.

E-beam processing has been used to irradiate piezoelectric polymers. In 1998, Zhang *et al.* reported an exceptionally high electrostrictive response after e-beam irradiation of P(VDF-TrFE) copolymer. [18] They claimed that the breaking of polar regions into nanopolar ones was responsible of this effect. The expanding and contracting of these polar regions under external fields, coupled with a large difference in the lattice strain between the polar and non-polar phases, generate an ultrahigh strain response. Of course, a poling step was added after e-beam irradiation at high doses (between 4.10^5 to 10^6 Gy - 1Gy = 100 rad -). Two years later, another team proposed other explanations in the change in ferroelectric behaviour upon e-beam irradiation of PVDF. Giegerich *et al.* have shown by electron spin resonance that a large number of radicals and trapped electrons remained after irradiation (~ 1 *per* crystallite), and that the electric conductivity increased from 0.11pS.m^{-1} in the non-irradiated but poled PVDF sample to 1.1pS.m^{-1} at 450kGy. The increase in conductivity with dose resulted in the enhancement of polarization. The same group reported also an interesting behavior: the creation of crosslinks upon irradiation allowed to slow down the reduction of polarization with time or at elevated temperature. [19]

Despite these beneficial effects of e-beam irradiation on the piezoelectric response in case of piezoelectric PVDF and related polymers, no industrial application has been developed using radiation treatment prior poling. The introduction of a third monomer has been industrially preferred to disrupt the long-range ordering of the ferroelectric polar phase, resulting in nanopolar domains as commercialized by Piezoech SA (Arkema group). At that time (around 20 years ago) piezoelectric polymers performances were most interesting for low-cost electrostrictive applications (strain gauges, tactile sensor arrays and transducers). Additional treatment such as radiation needs additional investment for industrials. For high-value components such as capacitors, FRAM chips, STM/AFM actuators and some ultrasound-transducers, the piezoelectric ceramics, such as the

PZT (Lead Zirconate Titanate) are preferred. Indeed, the piezoelectric ceramics have succeeded in achieving a high electromechanical coupling coefficient. However, these materials generally have a problem of mechanical breakdown that limits their lifetime and application in nowadays mobile equipment. Electric power generation using the piezoelectricity of PVDF is drawing much interest recently owing to its prospective features of high robustness, high flexibility, and easy formability. [20] Various attractive methods of harvesting energy generated from human motion such as walking [21] and the use of wind and raindrops [22] have been demonstrated and industrial objectives are now evolved. Notably, output electric energy can be increased by inducing a higher mechanical strain in PVDF. [10] Although e-beam processing generates defects inside the PVDF with a consequent deterioration of its mechanical properties, under certain dose range, it could increase the crystallinity content in PVDF. [23] A competitive mechanism, opposite to the increase of crystallinity, is the crosslinking. The critical dose range (dose gel) was found in the interval between 19.9, 35.11 kGy and 9.8, 34.11 kGy for the PVDF and the P(VDF/TrFE), respectively. [24] Further investigations in PVDF have shown a decrease of the melting temperature combined with an increase of the crosslinks, function of the radiation doses.[25, 26] However, the reported results, particularly those related to crystallinity, crosslinking and melting temperature are still contradictory and, as a result, further clarification studies are needed.

Before this PhD study, the few SHI irradiation on piezoelectric PVDF reported works were mainly from Betz's team (GANIL, France) [27] and Neumann's team (GSI, Germany). [28] The work of betz team in 1996 was focused on a dielectric study with and without radiografting of non-poled ferroelectric PVDF and P(VDF-co-TrFE) copolymers. The dielectric constant was strongly affected both by the SHI irradiation at high doses from 10^{10} cm^{-2} up to $1.4.10^{11}$ cm^{-2} (final dose of 994 kGy for Kr ion of kinetic energy of 10.7 MeV.amu^{-1} and, even more, by subsequent radiografting with polymethylmethacrylate. As the dielectric constant is directly link to dipole density, the latter results suggested a detrimental effect of SHI on the potential piezoelectric behaviour of PVDF and P(VDF-co-TrFE) materials. Three years later, in the work of Hillenbrand et al, the depolarization radii of latent heavy-ion tracks in PVDF has been clearly evidenced in poled ferroelectric PVDF films in comparable dose range and ion kinetic energies from a fluence of $0.5.10^{11}$ cm^{-2} to $4.5.10^{11}$ cm^{-2}. The basic processes induced by SHI are identical to those initiated by gamma-rays or electron beams. At ion kinetic energies high enough to preponderantly induce electronic interactions with the target material

instead of nuclear ones (typically at energies higher than 1 MeV.amu^{-1}), SHI deposit their energy through electronic processes occurring close to the ion path. SHI induce a continuous trail of excitations and damages all along the ion path. [29] Figure 1.1 shows an example of simulation of a track structure formed by the passage of a 5 MeV He^{2+} in in polyethylene. [30]
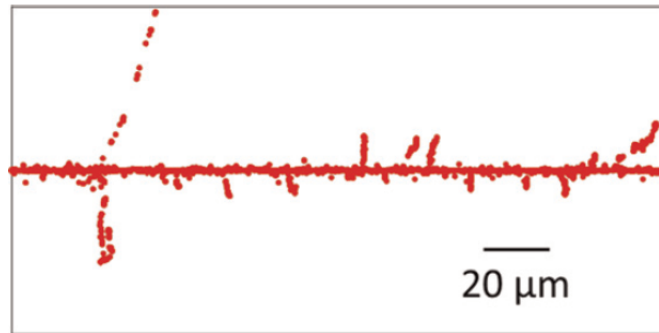
FIGURE 1.1: Calculated track formed by the passage of a 5 MeV He^{2+} ion in in polyethylene. [30]

While the track core corresponds to a more or less densely populated aggregation of extended defects and has a diameter of around 10 nm, corresponding to the range of the atomic collision-cascade, the track halo corresponds to the radiation damages of the electronic collision-cascade, the diameter of which depends on the ion velocity and may reach 1μm. However, most of the electron energy is deposited quite close to the projectile trajectory. The homogeneous damaged region surrounding the ion path has often been called a "nuclear track". Since tracks in some materials (such as polymer) can be chemically revealed, the initial damage is also referred to as the "latent track". [31] Numerous studies have been realized on latent tracks in PVDF. Ion track grafting was first described by Natacha Betz in 1995. [32] Grafted track-etched PVDF membranes have been subsequently developed [33] and have found many applications in fuel cell field [34] and in sensing devices. [35] Track etched membrane are also used as a template for nanostructured composites.[36, 37]

From literature, the reported dose range, in case of piezoelectric PVDF and related polymers, was high enough to diminish seriously the mean distance between two tracks (lowest fluence of GSI team was around 10^{11} tracks.cm^{-2}). The resulting track overlapping leads to a homogenization of the damages through the target polymer. It is worth investigating, in the case of poled PVDF, lower fluencies and measuring its piezoelectric response. In case of piezoelectric response preservation, it opens new perspectives in the fabrication of novel nanostructured composite devices based on track-etched PVDF membranes embedding

inorganic nanowires or nanotubes in the actual trend of developing piezoelectric hybrid nanogenerators. [38–41] A comparison study in equivalent low dose range with e-beam irradiation is also planned as these low doses in poled ferroelectric polymers were not deeply explored.

1.3   Objective of the work

Piezoelectric PVDF and its copolymer are good candidates for harvesting energy and actuators application. The objective of my work is to enhance the piezoelectric effect (direct and inverse) in PVDF and its copolymer exploiting radiation as a primary source to modify the structure and properties of the polymers.

The thesis work is divided in three parts. The first part is grouping the background theory necessary to support the experimental work. The second part is focused on the measurement of the inverse piezoelectric effect through a nanocomposite material based on PVDF and Ni NWs.

In the third part of the work, I will explore two different strategies to enhance the direct piezoelectric effect by i)radiation sources and ii) nanostructuration.

Part I

Background theory

Chapter 2

Piezoelectric PVDF

In this chapter, I will introduce the background theory related with the piezo-electricity and dielectric properties of the PVDF film. In particular, I will focus on interfacial polarization to show how the filler in nanostructured polymeric is able to increase the dielectric permittivity (section 2.5). The linear theory of the piezoelectric material is briefly introduced in section 2.8. The correlation between piezoelectricity and PVDF polymorphism is also presented in section 2.9. Finally, the piezoelectric formalism is applied to the bi-oriented piezoelectric film in section 2.10.

2.1 Dielectric polarization

At the atomic level, all matter consists ultimately of positive and negative charges balancing each other microscopically or macroscopically. In the case of metal, *i.e.*, the cloud of negative charge is neutralized by the fixed positive charge of the atomic cores constituting the lattice itself. Even though the positive and negative charges do not separate completely in space to give two separate free particles of opposite sign, the charge distribution within a neutral molecule may be distorted to create a local molecular charge imbalance in which the "centers of gravity" or the first moments of the positive and negative charges, $\pm q$, become separated by a finite distance l, thus creating a *dipole* with a dipole moment $\mu=ql$. The dimension of the dipole moment in SI unit are $[\mu]$=C.m. The relative shift of the positive and negative charges in matter is referred to as *dielectric polarization*. Despite the absence of an external field, there are many examples where the finite polarization is present, *i.e.*, the *permanent polarization* in *ferroelectrics* (more details in section 2.7). Our interest will be devoted entirely to the phenomenon of polarization produced by an electric field. The general relation between the polarization P and the electric field E can be written:

$$P = \epsilon_0 \chi E + \text{Higher terms in E} \tag{2.1}$$

The first term proportional to the field is of dominant importance in most system, ϵ_0 is the *permittivity of free space* and χ is the *susceptibility*. The higher terms give rise to phenomenon know as *hyperpolarization*. The linear permittivity of a homogeneous material is usually given relative to that of free space, as a *relative permittivity* ϵ_r (also called *dielectric constant*). The actual permittivity is then calculated by multiplying the relative permittivity by ϵ_0:

$$\epsilon = \epsilon_0 \epsilon_r = (1 + \chi)\epsilon_0 \tag{2.2}$$

The susceptibility of a medium is related to its relative permittivity ϵ_r by:

$$\chi = \epsilon_r - 1 \tag{2.3}$$

Let us consider a planar capacitor consisting of two parallel metallic electrodes filled with a material medium with susceptibility χ. If an uniform electric field is applied between the electrodes, the total charge (called *electric displacement* D) on the electrodes becomes the sum of the contributions of the free space and the contribution due to the material medium polarization:

$$D = \epsilon_0 E + P = \epsilon_0 (1 + \chi)E = \epsilon_r \epsilon_0 E \tag{2.4}$$

We conclude that a finite relative displacement of positive and negative charges produces a dipole moment throughout a given volume space in which these charges are present and the effect of this dipole moment is to produce a charge density at the external boundaries, assumed to be normal to the displacement, which is equal to the dipole moment per unit volume.

2.2   Frequency domain of dielectric response

The static response of dielectric system to a steady electric field represent only one facet of the complete problem. Much more important is the time-dependent response to time-varying electric fields. The most obvious physical reason for the time-dependence of dielectric response is the inevitable "inertia" of the physical system. If we consider a capacitor with two plane parallel electrodes and we apply a time-dependent electric field E(t), the expression 2.4 becomes:

$$D(t) = \epsilon_0 E + P(t) \tag{2.5}$$

Here D(t) denotes the *dielectric induction*.
The resulting current flowing in the system is:

$$I = \sigma_0 E + \frac{\partial D}{\partial t} \tag{2.6}$$

This current, so-called *polarization current* is characteristic of the adjustment of the polarizing species, and it arises from continuous movement of "free" charges across the dielectric material. This current should not be confused with the mechanism of dc conductivity related to the parameter *conductivity* σ_0. A powerful alternative to the time-dependent response is the frequency domain. Taking the Fourier transform of the equation 2.6, we get the corresponding frequency-domain response:

$$I(\omega) = \sigma_0 E(\omega) + i\omega D(\omega) \tag{2.7}$$

Where D(ω) is defined by the expression:

$$D(\omega) = \epsilon_0 E(\omega) = \epsilon_0 [1 + \chi'(\omega) - i\chi''(\omega)] E(\omega) \tag{2.8}$$

The physical interpretation of the frequency-domain dielectric induction D(ω) is that its real part gives that component of the total induced charge at the plates which is in phase with the driving field E(ω). The imaginary component of D(ω) gives the charge that is in quadrature with the driving field E(ω). A complex dielectric permittivity is defined as the complex ratio of the induction and field at a given frequency:

$$\epsilon(\omega) = \epsilon'(\omega) - i\epsilon''(\omega) \tag{2.9}$$

where ϵ' is the real part of the complex permittivity. It indicates the ability of the material to store energy from applied electric field. The imaginary part of the permittivity is called *dielectric loss*, ϵ''. It describes the dielectric losses related to the dipolar relaxation mechanisms.
The ratio between ϵ'' and ϵ' is defined as the *electric loss tangent*:

$$\tan \delta = \frac{\epsilon''(\omega)}{\epsilon'(\omega)} \tag{2.10}$$

The practical significance of tan δ is the ratio of the energy dissipated *per radian* in the dielectric to the energy stored at the peak of the polarization.

2.3 Type of dielectric polarizations

There are several microscopic mechanisms of polarization in a dielectric material. Electric dipole moments can be induced by the electric field or can be permanent. The induced electric dipole moment can be a result of two polarization phenomena, *i.e.*, electronic polarization and distortion polarization.

Electronic polarization, describes the displacement of the cloud of bound electrons with reference to the nucleus under an applied electric field. The atom distorts and the center of the atom's negative charge no longer coincides with the position of the nucleus, resulting in an electric dipole moment.

Distortion polarization also often referred to as *ionic polarization* relates to the distortion of the position of the nuclei by the applied field, thereby stretching or compressing the bond length, depending on the relative orientation between the ionic bond and the electric field. The molecule is bent and stretched by the applied field and its dipole moment changes accordingly. Nonpolar molecules may acquire an induced dipole moment in an electric field on account of the distortion the field causes in their electronic distributions and nuclear positions.

Orientational or *rotational* polarization usually occurs in polar molecule with a permanent electric dipole moment. The permanent dipole moment is a result of the partial charges on the atoms in the molecule that arise from the different electronegativity or other features of bonding. Polar molecules may have their existing dipole moments modified by the applied field. Orientation polarization relates to the phenomenon of a permanent dipole moment as a result of polar molecules. [42]

2.4 Dielectric relaxation

When the applied electric field is an ac field, the frequency of the signal comes into play. Considering the consequences for the polarization phenomena. Electronic polarization follows the electric field almost instantaneously as only the displacement of bound electrons is involved. Both electronic and distortion polarization are subject to a counteractive restoring force, which gives rise to a resonant frequency. The distortion polarization cannot respond as rapidly to fast changing fields since it involves the displacement of entire ions. In contrast, orientation polarization requires the motion of complete molecules. For orientation polarization, there is no counteractive restoring force. At low frequencies the three polarization phenomena contribute to the real part of the dielectric constant. The maximum frequency for orientation polarization is on the order of 10^9

Hz. Above, this frequency distortion and the electronic polarization contribute to the dielectric constant up to the resonance frequency for distortion polarization, which is typically in the order of 10^{13} Hz, and beyond that only electronic polarization is defining the dielectric constant. The resonant frequency of the electronic polarization is typically beyond the frequency of visible light at 10^{15} Hz (Figure 2.1). [42]
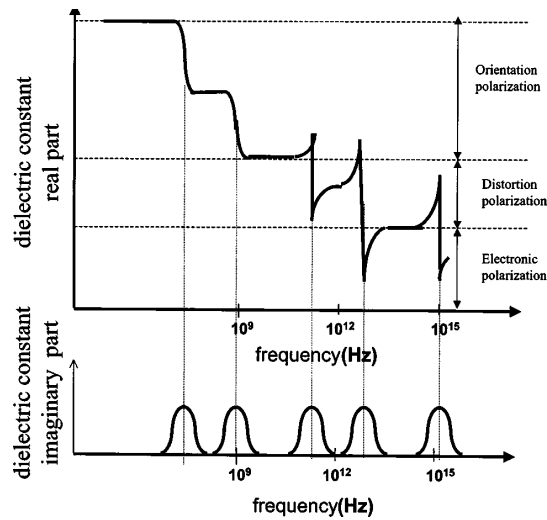
FIGURE 2.1: Schematic curve of the real and imaginary parts of the dielectric constant of a fictive material. This material exhibits two different orientation polarization modes and two different distortion polarization modes. [42]

2.5   Interfacial polarization

Interfacial polarization, termed the Maxwell-Wagner-Sillars (MWS) effect, is observed in heterogeneous systems composed of two or more phases. Under an applied electric field, an accumulation of the migrating charges occurs at the interface of the phases. Thus, the interface represents a physical barrier due to the difference in the conductivities and permittivities between phases. The accumulation of charges distorts the local electric field, increasing of the permittivity of the system. One phase could be the filler in the case of a composite material, or defects, generally located into a matrix, such as voids, grain boundaries and impurities. [11]

Composites based on organic and inorganic phases present a direct relationship between the microstructure characteristics and the electrical properties, more specifically in the percolation threshold (f_c). The percolation threshold f_c can be estimated using a power law 2.11, which correlates the volume fraction of the filler and the matrix conductivity. This law predicts an increasing of the composite conductivity when the filler content is increased:

$$\begin{cases} \sigma_{eff} \propto (f_f - f_c)^t & f_f > f_c \\ \sigma_{eff} \propto (f_f - f_c)^{-s'} & f_f < f_c \end{cases} \tag{2.11}$$

Where σ_{eff} is the effective composite film conductivity, t is the critical exponent in the conducting region, and s' is the critical exponent in the insulating region. [13]

The best fits of the conductivity data to the log-log plots of the power law give the values of f_c, t, and s'. A similar power law can be used to describe the dielectric constant in a composite: the measured dielectric constant shows a divergence at both sides of percolation threshold. This variation of the dielectric constant near to the percolation threshold is given by:

$$\epsilon_{eff} \propto (f_c - f_f)^{-s} \tag{2.12}$$

Where s is the dielectric critical exponent. [43]

The introduction of inorganic nanoparticles into polymer matrices to form dielectric polymer nanocomposites represents one of the most promising and exciting method for the development of dielectric materials. In the case of PVDF, the inorganic part could be conductive, semiconductive or dielectric. PVDF matrix with embedded NiO nanosheets were investigated by Amoresi *et al.* They found a

percolation threshold at 4.0 vol% of NiO nanosheets. The obtained dielectric constant was up to six-fold larger than the PVDF film without filler. [13]

Microcapacitor networks with exfoliated graphite nanoplates have been developed by He *et al.* The conductive graphite nanoplates were isolated by very thin dielectric insulating-polymer layers forming microcapacitors, which leads to a very high dielectric constant near to the percolation threshold. The value of dielectric constant measured at 1000Hz and room temperature was found 270 times higher than that of a PVDF matrix. [44]

In the case of metallic filler, Dang *et al.*, [43] investigated the role of Ni particles in PVDF matrix. The attained value of the effective dielectric constant of the percolation composite at room temperature as high as ca. 400, which is about 40 times higher than the effective dielectric constant of PVDF (Figure 2.2).
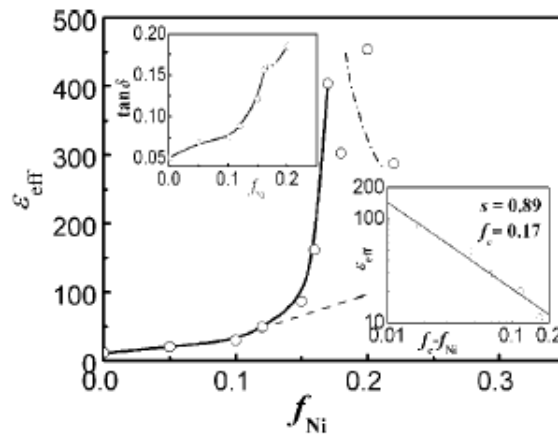
FIGURE 2.2: Variation of the effective dielectric constant, ϵ_{eff} of the Ni-PVDF composite with Ni volume fraction f_{Ni} measured at room temperature and 100Hz. [43]

2.6   Piezoelectric effect and crystallinity

Piezoelectric, pyroelectric and ferroelectric behaviours are related to the crystalline structure of the materials. A crystal can be categorized by its lattice and the atoms that lie in a primitive cell. There are seven possible primitive cells to fill all the lattice space without leaving gaps:

- cubic (a=b=c, $\alpha=\beta=\gamma$ =90°);

- hexagonal (a=b≠c, $\alpha=\beta$=90°, γ =120°);

- tetragonal (a=b≠c, $\alpha=\beta=\gamma$ =90°);

- rhombohedral (a=b=c, $\alpha=\beta=\gamma\neq$90°);

- orthorhombic (a≠b≠c, $\alpha=\beta=\gamma$ =90°);

- monoclinic (a≠b≠c, $\alpha=\gamma$=90°≠β);

- triclinic (a≠b≠c, $\alpha\neq\beta\neq\gamma$);

Here, a, b, c, α, β and γ are the parameters of each lattice (Latin letters = lattice constants and Greek letters = angles). Furthermore, other seven crystal systems are derived from primitive lattices call *Bravais lattices*: centered cubic, face-centered cubics, centered tetragonal, base-centered orthorombic, centered orthorombic, face-centered orthorombic, and base-centered monoclinic lattices.

It is possible to take microscopic symmetries into account if we consider the pattern attached to the lattice. The so-called *space groups* are combination of the translational symmetry of a unit cell including lattice centering, the point group symmetry operations of reflection, rotation and improper rotation (also called rotoinversion), the screw axis, and glide plane symmetry operations. The combination of all these symmetry operations results in a total of 230 different space groups. From the structural point of view, all symmetry elements describing macroscopic properties should refer to one single point. Considering the entire crystal, 32 *crystal classes* or *point groups* are defined.

The crystals are composed of electrically charged particles. In particular, the lack of a center of symmetry in the crystal determine the arrangement susceptible to give a piezoelectric effect. Thus, starting from the 32 existing crystal classes only 21 do not posses a center of symmetry (Table 2.1). Out of these 21 classes, one displays no piezoelectric effect (cubic system with crystal class 432) due to the movement of the charges, during mechanical sollicitation, which does not induce the appearance of a dipole.

In 20 of these groups, an electric dipole is generated when a mechanical stress is applied to them. Among these 20 piezoelectric systems only 10 of them have polar axis and thus permanent polarization can be observed in the absence of an electric field or mechanical stress, making them pyroelectric. Additionally, polar materials can have ferroelectric properties. It's important at this point to define properly these physical properties.

TABLE 2.1: Crystal classes with their crystal system, those that display a center of symmetry, and piezoelectric effect

Crystal system	Crystal class	center of symmetry	Piezo/Pyro
Triclinic	$\bar{1}$	X	-
	1	-	Pyro
Monoclinic	2/m	X	-
	2	-	Pyro
	m	-	Pyro
Orthorombic	mmm	X	-
	222	-	Piezo
	mm2	-	Pyro
Tetragonal	4/mmm	X	-
	422	-	Piezo
	4mm	-	Pyro
	$\bar{4}$2m	-	Piezo
	4/m	X	-
	4	-	Pyro
	$\bar{4}$	-	Piezo
Trigonal	$\bar{3}$m	X	-
	32	-	Piezo
	3m	-	Pyro
	$\bar{3}$	X	-
	3	-	Pyro
Hexagonal	6/mmm	X	-
	622	-	Piezo
	6mm	-	Pyro
	$\bar{6}$2m	-	Piezo
	6/m	X	-
	6	-	Pyro
	$\bar{6}$	-	Piezo
Cubic	m$\bar{3}$m	X	-
	432	-	-
	$\bar{4}$3m	-	Piezo
	m$\bar{3}$	X	-
	23	-	Piezo

2.7 Piezoelectricity, pyroelectricity and ferroelectricity

The piezoelectric effect linearly links a mechanical variable to an electric variable. The direct effect was discovered by the Curie brothers in 1880: they described the creation of an electrical charge during the application of a mechanical stress on the piezoelectric material. Lippmann, later, suggested the existence of the reverse effect: inverse piezoelectric effect. [45]

In a piezoelectric material the arrangement of positive and negative ions does not result in any permanent dipole moment in the absence of an external force. In other words, even if the dipole existed (non-centrosymmetric system), the net dipole is zero. When the force is applied, the amplitude of the dipole moments varies with the appearance of a net dipole moment. Considering the inverse piezoelectric effect, the mechanical strain is induced by an external applied electric field.

Pyroelectric material (which is still piezoelectric), is characterized by the presence of the permanent dipoles, in fact they are naturally electrically polarized. Applying a force or a temperature change leads to deform the lattice and therefore the dipole moment, hence the appearance of the charges on the extremities of the dielectric. The direction in which the propagation of the charge tends toward is usually constant throughout a pyroelectric material, but, in some materials, this direction can be reversed. These materials are said to exhibit ferroelectricity.

Ferroelectricity is a property of certain materials that have a spontaneous electric polarization that can be reversed by the application of an external electric field. In addition, ferroelectric materials retain a residual polarization after an applied electric field has been switched off. In contrast with normal dielectric materials, ferroelectric materials show a nonlinear relationship between polarization and the electric field applied, as shown in Figure 2.3.

When the intensity of the electric field is increased, ferroelectric materials exhibit a saturation polarization, P_s, at high field strength. They also retain a remanent polarization, P_r, when the electric field is reduced to zero after saturation, and when an electric field is applied in the opposite direction, the polarization vector is reversed, which is usually known as switching. The coercive field, E_c, is the electric field required to reduce the polarization to zero. Typically, materials demonstrate ferroelectricity only below a certain phase transition temperature, called the Curie temperature, T_c, and are paraelectric above this temperature: the spontaneous polarization vanishes, and the ferroelectric crystal transforms into the paraelectric state. Many ferroelectrics lose their piezoelectric properties
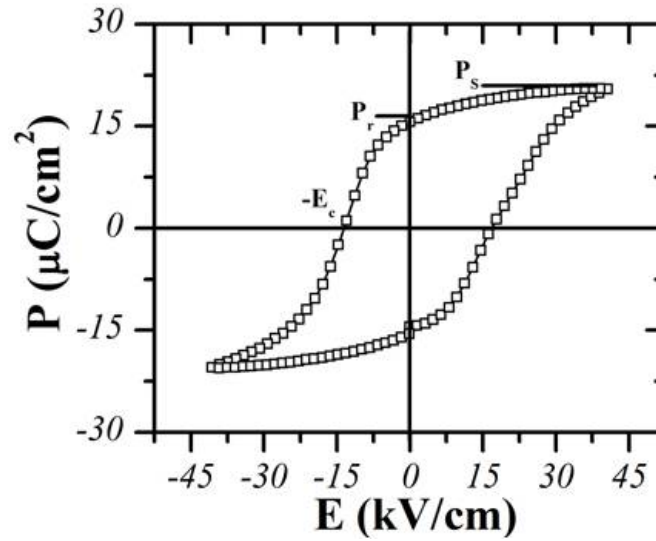
FIGURE 2.3: Hysteresis loop for a general ferroelectric material.

above T_c completely, because their paraelectric phase has centrosymmetric crystallographic structure.

2.8   Linear theory of piezoelectricity

Linear piezoelectricity is the combined effect of:

- The linear electrical behavior of the material:

$$D = \epsilon.E \tag{2.13}$$

  In form of tensors become:

$$D_i = \epsilon_{ij}.E_j \tag{2.14}$$

  Where D is the electric displacement, ϵ is permittivity (rank tensor 2) and E is the electric field, and $\nabla \cdot D = 0$, $\nabla \times E = 0$.

- Hooke's Law for linear elastic materials:

$$S = s.T \tag{2.15}$$

  In form of tensors become:

$$S_{ij} = s_{ijkl}.T_{kl} \tag{2.16}$$

Where S is the strain (rank tensor 2), s is the compliance (rank tensor 4) and T is the stress. $\nabla \cdot$ T = 0, S=$\frac{\nabla u + u \nabla}{2}$

These may be combined into so-called coupled equations, of which the strain-charge form is:

$$S_{ij} = s^E_{ijkl}T_{kl} + d_{kij}E_k$$
$$D_i = d_{ijk}T_{jk} + \epsilon^T_{ij}E_j$$

(2.17)

In matrix form:

$$S = [s^E]T + [d^t]E$$
$$D = [d]T + [\epsilon^T]E$$

(2.18)

where [d] is the matrix for the direct piezoelectric effect and [d^t] is the matrix for the converse piezoelectric effect. The superscript E indicates a zero, or constant, electric field; the superscript T indicates a zero, or constant, stress field; and the superscript t stands for transposition of a matrix.

2.9 Polymorphism in PVDF film

PVDF polymorphism is well-known and consists in four crystalline phases, named phases α, β, γ and δ. The macromolecules can rotate about each single bond. Depending on the orientation of the substituents, two main torsional bond arrangements can be distinguished: *trans(t)*, with a 180° and *gauche (g$^\pm$)*, with a $\pm$120° orientation.

Thermodynamically, the most stable phase at room temperature and pressure is the α phase. The α phase is characterized by an alternating trans and gauche tg^+tg^- sequences resulting in a zero net dipole moment. The reported space group for alpha phase is *P2$_1$/c* (14). According with the Table 2.1 it is included in the crystal class *2/m* monoclinic with no piezo/pyro properties.

The polarized phase of α is δ phase. According with Li *et al.* [46] to transform α in δ the first and the third chains have to be rotated by 180° around the chain axis. Moreover, these chains also need to be shifted by half the c-axis length. The resulting lattice for δ is truly orthorhombic belonging to crystal class mm2 with space group *Pna2$_1$* (33).

Biaxial stretching is the most common technique used to transform the paraelectric α phase to β phase. [47, 48] In the β phase, two chains are in an all-trans (*ttt*) planar zigzag conformation resulting in a net dipole moment with a strong pyro/piezo effect. The space group associated to β phase is the *Amm2* (38) relative to the orthorhombic crystal system *mm2*. [49, 50]

The polymer chains in γ PVDF has a conformation (*tttg$^+$tttg$^-$*). The crystal class

for γ is monoclinic *2* with a space group *C121* (5) with moderate piezo/pyro properties. [49]

Except for β phase, δ and γ are hardly accessible. In the case of γ phase, temperature control and high pressure are required. A remanent polarization is obtained in ferroelectric δ phase applying high electric field around 250MVm^{-1}. [46]

2.10 Piezoelectricity formalism applied to bi-stretched PVDF film

Considering the formalism 2.18 in form of tensors, we obtain for the strain and electric displacement respectively:

$$
\begin{pmatrix} S_1 \\ S_2 \\ S_3 \\ S_4 \\ S_5 \\ S_6 \end{pmatrix} = \begin{pmatrix} s_{11} & s_{12} & s_{13} & s_{14} & s_{15} & s_{16} \\ s_{21} & s_{22} & s_{23} & s_{24} & s_{25} & s_{26} \\ s_{31} & s_{32} & s_{33} & s_{34} & s_{35} & s_{36} \\ s_{41} & s_{42} & s_{43} & s_{44} & s_{45} & s_{46} \\ s_{51} & s_{52} & s_{53} & s_{54} & s_{55} & s_{56} \\ s_{61} & s_{62} & s_{63} & s_{64} & s_{65} & s_{66} \end{pmatrix} \begin{pmatrix} T_1 \\ T_2 \\ T_3 \\ T_4 \\ T_5 \\ T_6 \end{pmatrix} + \begin{pmatrix} d_{11} & d_{21} & d_{31} \\ d_{12} & d_{22} & d_{32} \\ d_{13} & d_{23} & d_{33} \\ d_{14} & d_{24} & d_{34} \\ d_{15} & d_{25} & d_{35} \\ d_{16} & d_{26} & d_{36} \end{pmatrix} \begin{pmatrix} E_1 \\ E_2 \\ E_3 \end{pmatrix} \quad (2.19)
$$

$$
\begin{pmatrix} D_1 \\ D_2 \\ D_3 \end{pmatrix} = \begin{pmatrix} d_{11} & d_{12} & d_{13} & d_{14} & d_{15} & d_{16} \\ d_{21} & d_{22} & d_{23} & d_{24} & d_{25} & d_{26} \\ d_{31} & d_{32} & d_{33} & d_{34} & d_{35} & d_{36} \end{pmatrix} \begin{pmatrix} T_1 \\ T_2 \\ T_3 \\ T_4 \\ T_5 \\ T_6 \end{pmatrix} + \begin{pmatrix} \epsilon_{11} & \epsilon_{12} & \epsilon_{13} \\ \epsilon_{21} & \epsilon_{22} & \epsilon_{23} \\ \epsilon_{31} & \epsilon_{32} & \epsilon_{33} \end{pmatrix} \begin{pmatrix} E_1 \\ E_2 \\ E_3 \end{pmatrix} \quad (2.20)
$$

We consider a cartesian coordinate system where *x*, *y*, and *z* correspond respectively with *1,2,3* directions. Conventionally, because *S* and *T* are all symmetric tensors, the subscript of strain and stress can be relabeled in the following manner: $11 \rightarrow 1$; $22 \rightarrow 2$; $33 \rightarrow 3$; $23 \rightarrow 4$; $13 \rightarrow 5$; $12 \rightarrow 6$. That is why *S* and *T* appear to have the "vector form" of six components. Consequently, *s* appears to be a 6-by-6 matrix instead of a rank-4 tensor.

The relations in 2.19 are referred to characterize anisotropic materials since there are no planes of symmetry. Considering β as the only ferroelectric phase in the

PVDF, the compliance and piezoelectric tensor are reduced by the additional degree of symmetry of the orthorhombic system (crystal system *mm2*). Thus, the compliance and piezoelectric tensors become respectively [51, 52]:

$$
\begin{pmatrix}
s_{11} & s_{12} & s_{13} & 0 & 0 & 0 \\
s_{12} & s_{22} & s_{32} & 0 & 0 & 0 \\
s_{13} & s_{32} & s_{33} & 0 & 0 & 0 \\
0 & 0 & 0 & s_{44} & 0 & 0 \\
0 & 0 & 0 & 0 & s_{55} & 0 \\
0 & 0 & 0 & 0 & 0 & s_{66}
\end{pmatrix}
\tag{2.21}
$$

$$
\begin{pmatrix}
0 & 0 & 0 & 0 & d_{15} & 0 \\
0 & 0 & 0 & d_{24} & 0 & 0 \\
d_{31} & d_{32} & d_{33} & 0 & 0 & 0
\end{pmatrix}
\tag{2.22}
$$

Considering the case of the *direct piezoelectric effect*, where the electric field is zero in all of the three directions (E_1=E_2=E_3=0), and in the hypothesis where the stress is applied in direction *3* (perpendicular to the film surface), we are able to simplify the constitutive equations 2.19 and 2.20.

Replacing the 2.21 in the 2.19, we obtain the Hook's law in the three directions:

$$
S_1 = s_{13}T_3 \tag{2.23}
$$

$$
S_2 = s_{23}T_3 \tag{2.24}
$$

$$
S_3 = s_{33}T_3 \tag{2.25}
$$

If we consider a bi-stretched piezoelectric film (stretching in directions *1* and *2*), the additional hypothesis is that the strain in the directions *1* and *2* are identical. Moreover, in the case where the film is fixed on a circular support and the stress is applied in direction *3*, we can suppose that the strain in the directions *1* and *2* are neglegible in comparison with the strain in direction *3*.

Replacing the 2.22 in 2.20, we obtain:

$$
D_3 = d_{33}T_3 \tag{2.26}
$$

In this special case the only contribute to the electric displacement is proportional to the piezoelectric coefficient d_{33}.

Chapter 3

Swift Heavy Ions (SHI) and electron beam (e-beam) irradiations

In this chapter I will illustrate the effect of radiations in matter. Two radiation sources have been chosen: electron beam (e-beam) and swift heavy ions (SHI) radiation. The SHI and e-beam characteristics are described in section 3.1, with particular attention to the latent-track formation in the case of SHI. Section 3.2 highlights the typical defects generated in polymers after irradiation process.

3.1 Radiation and Matter

Radiation chemistry is the study of the chemical changes produced by the absorption of radiation of sufficiently high energy to produce ionization. The so-called *ionizing radiations* are composed of photons (gamma or X-rays, bremsstrahlung), accelerated particles (electrons, lightions, swift heavy ions(SHI)), and particles ejected from radioactive emitters (α or β^-). The ionization radiation interact with the atoms of the target material by transferring energy. The electrons may be ejected from the atoms, giving positively charged ions and free electrons, or may be moved to a higher-energy atomic orbital, giving an excited atom or molecule. The deposited energy depends on the radiation type and its energy.

 (i) Photoelectric effects at low energies ($\sim$ 1- 10^2 keV).

 (ii) Compton scattering (10^2-10^4 keV).

 (iii) Electron-positron pair production for energy higher than 1.02 MeV(twice the rest-mass energy of an electron) and for materials containing heavy atoms.

Regarding at the processes by which ionizing radiation interact with the matter we can distinguish elastic and inelastic scattering.

An elastic scattering occurs when electrons are deflected by the electrostatic field of an atomic nucleus. The elastic scattering is greatest with incident low-energy electrons and high stopping power. These two conditions contribute to the irregular path followed by the electrons. On the other hand, in an inelastic scattering, the electrons interact with the electrostatic field of atomic electrons so that they are either raised to a higher energy level (*i.e* the atoms are excited) or they are ejected from the atom (the atoms are ionized).

3.1.1   Physical quantity of ionizing radiations

- The **stopping power** also called *Linear Energy Transfer* (LET) is quantifies as the energy loss *per* unit path lenght:

$$L_\Delta = \frac{\mathrm{d}E_\Delta}{\mathrm{d}x} \tag{3.1}$$

  Where $\mathrm{d}E_\Delta$ is the energy loss of the charged particle due to electronic collisions while traversing a distance $\mathrm{d}x$. LET is frequently expressed in keV.μm^{-1}, MeV.mm^{-1}, or MeV.cm^2.mg^{-1}.

- The **fluence**, n, represent the number of ionizing particles *per* unit area. It is linked with the flux Φ, and the exposition time as indicated in the following expression:

$$n = \int_0^{t_e} \Phi dt \tag{3.2}$$

- The **absorbed dose**, D, represent the quantity of energy absorbed by the sample target *per* unit mass. It is measured in **Gray** (Gy): 1 Gy = 1 J.kg^{-1} = 100 rad. The absorbed dose is linked with stopping power expressed in MeV.cm^2.mg^{-1} as shown in the following expression:

$$D = C \times n\frac{dE}{dx} \tag{3.3}$$

  C is conversion constant (J.mg.MeV^{-1}kg^{-1}) and it is equal to $1.6.10^{-7}$.

- The **dose rate** is the absorbed dose variation *per* unit time (Gy.s^{-1}):

$$\dot{D} = \frac{dD}{dt} \tag{3.4}$$

- The **path length**, *R*, of the charged particles is calculated using the following expression:

$$R = \int_0^E \left(\frac{dE}{dx} \right)^{-1} dE \qquad (3.5)$$

3.1.2 Electron irradiation

The electrons may be interact with the target atoms through either elastic or inelastic collisions. Energy around few MeV lead to inelastic collisions. As opposed to the ion, the electron transports a constant charge and it has a lower mass. The kinetic energy of the incident electron, in this case, is weak but enough to transfer part of its energy on the target atoms. As a result the trajectory of the incident electron is deflected. The target electrons (called *secondary electrons*) are ejected from the target atoms leading to the ionization of other neighbor atoms and producing a cascade effect. The absorbed energy is homogeneous along the thickness of the polymer film.

3.1.3 Ion irradiation

Ion irradiation requires an ion accelerator with a large range of energy, flux and incident angles. The characteristics of this technique are:

1. *Randomly distribution* of the ions on the target.

2. *Radial distribution* of the energy around the ion path.

The interaction ion-matter is a combination of elastic and inelastic collision. The resulting stopping power is the sum of the electronic and nuclear loss.

$$S(E) = -\frac{dE}{dx} = S_n + S_e \qquad (3.6)$$

Where S_n and S_e are the nuclear and electronic stopping power respectively. The stopping power can be calculted with the following expression:

$$-\frac{dE}{dx} = \frac{4\pi Z_1^2 e^4 Z_2}{m_0 v^2} \times ln\left(\frac{2m_0 v^2}{I} \right) \qquad (3.7)$$

Where, Z_1 and Z_2 are the atomic number of incident particle and target atoms, v is the particle velocity of the incident ion, e and m_0 are the charge and the mass of the electron, and *I* is the ionizing potential.
Figure 3.1 shows the stopping power as a function of the incident ion energy. The first part of the curve is dominated by nuclear stopping power with maximum energy around 0.1MeV.u^{-1}. At higher energy (1MeV.u^{-1}) S_e is predominant.
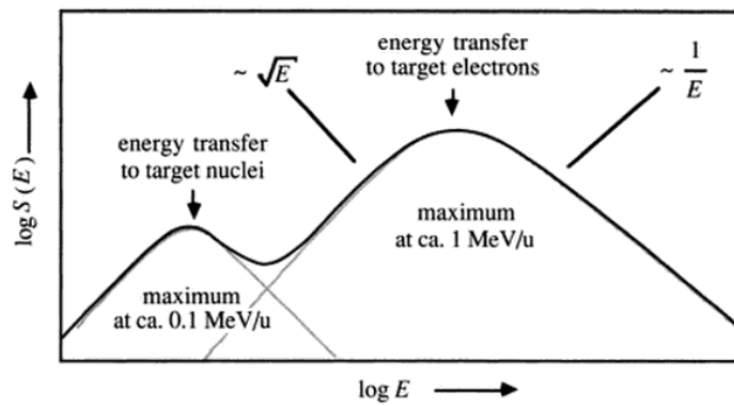
FIGURE 3.1: Qualitative shape of stopping function S(E) versus kinetic energy E of the projectile-ion. [29]

Latent track formation

The passage of the ions across the sample generate a cylindrical damage zone called '*latent-track*'. [29] the latent track formation may be described in two steps:

1. The incident ion interacts with the atoms of the target (10^{-17}s). The electronic loss induces ionization and exitation of the atoms. The defects propagate in radial direction in a cylindrical zone with radius around 10 nm.

2. After the first interaction an electronic cascade collision (10^{-15} - 10^{-14}s) takes place. The defects expand radially with a final diameter between 100 and 1000 nm.

The density of the polymer inside the latent-track is lower than the bulk, due to the large amount of defects such as chain scissions and radicals.
Chemical etching may be use to reveal the tracks obtaining nanopores. Polymers are characterized by etching threshold. It is defined as the minimum energy loss that is required for forming an etchable track. In the case of polyimide Kapton the threshold for an homogeneous etching has been found around 450 eV.Å^{-1} (Figure 3.2). [53]
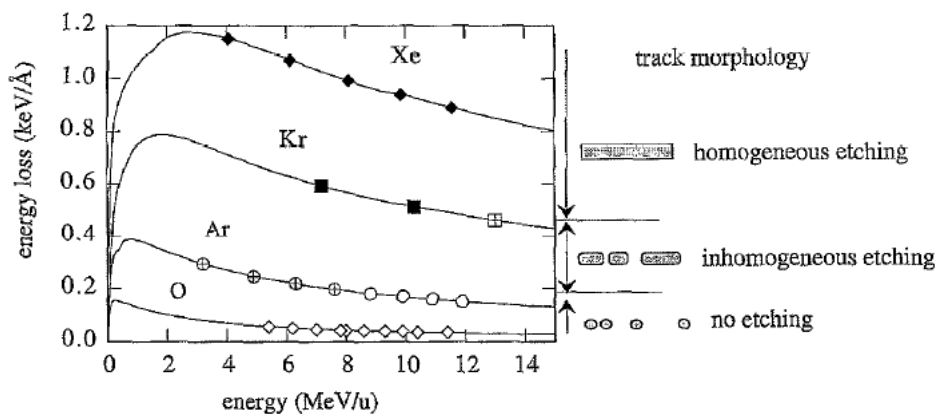
FIGURE 3.2: Calculated curves of the energy loss of Xe-, Kr-, Ar-, and O-ions in kapton as function of their specific energy. Full symbols (◆,■): etched tracks with small pore size distribution, crossed symbols (⊕,⊞): etched tracks with wide pore size distribution, open symbols (◇,○): no pores. [53]

3.2 Radiation effect in polymer

The molecular changes induced by ionizing radiations in a polymer can be of several types:

(i) Emission of volatile compounds (hydrogen H_2, carbon oxides CO and CO_2, hydrocarbon molecules like methane CH_4...),

(ii) Creation of unsaturated bonds and other molecular bonds, and formation of low molecular weight molecules (alcohols, carboxylic acids,...),

(iii) Crosslinking and chain scissions.

New bonds created depend on the polymer chemical structure through the nature of the excited states created, on its composition (impurities, fillers, and/or additives), and on their radiation parameters (oxygen, LET, temperature,...). The presence of oxygen during irradiation introduces a degradation mechanism due to the reaction between oxygen and radicals. The oxidation process is enhanced by high temperature and doses. Temperature has also effects in gas production. The concentrations of scissions, crosslinking and new bonds in the polymer is influenced by the radiation doses.

3.2.1 Initial species in polymer

Inelastic collision between ionizing radiation and target electrons, leads to either ionization (i) or electronic excitation (ii), depending of the deposited energy

(Dose).

(i) At the ionization energy, E_i (around 15eV), the ionization radiation leads to ion species. The general reaction is:

$$\text{AB} \xrightarrow{\text{ionizing radiation}} \text{AB}^+ + e^-$$
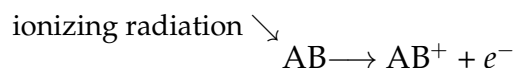
(ii) at high energy (>15eV), the ionizing radiation leads to excite molecules that generally relax to give radicals through homolytic bond ruptures, as shown in the following reaction:

$$\text{AB} \xrightarrow{\text{ionizing radiation}} \text{AB}^*, \text{AB}^{**} \longrightarrow \text{A}\bullet + \text{B}\bullet$$
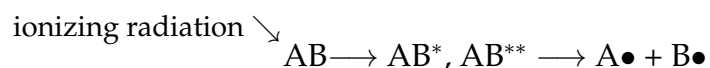
Starting from the molecule AB, we indicate here with AB^* and AB^{**} respectively its excited and its highly excited form. The resulting radicals ($\text{A}\bullet$ and $\text{B}\bullet$) are considered as high reactive species. These species can stay trapped in crystalline domais, in case of semi-crystalline polymers or can be involved in other reactions and transformations inside the polymer (*i.e.* crosslinking).

3.2.2   Gas emission

Main gases generally evolved from organic polymers submitted to low-ionizing radiations are:

(i) Hydrogen H_2,

(ii) Carbon oxides, CO and CO_2, in polymers containing oxygen atoms (like polycarbonate PC or polyacrylates),

(iii) Hydrocarbon molecules of low masses (like CH_4, C_2H_4 or C_2H_6),

(iv) Halogenated gases (like HCl or HF), in halogenated polymers.

The different gases formed are fingerprints of the polymer structure. For instance, methane and ethane are main hydrocarbons evolving from irradiated polypropylene and polybutylene, respectively.

3.2.3 Radicals and double bonds formation in PVDF

Considering ionizing radiations in PVDF, different defects can be detected:

(i) Generally high doses radiation (MGy) goes with high level of heat leading to progressive *amorphisation* of the semi-crystalline PVDF. [15] Infra-red spectra show as the group CH_2 of the crystalline phase, located at 3025cm^{-1} and 2985cm^{-1}, decrease when the absorbed dose increases. The same behaviour is observed for the bands, located between 1500-500 cm^{-1}, relative to the α and β phase. For doses in a range of 5 to 200 kGy, no amorphization was observed. [26]

(ii) *Double-bonds* formation were observed along the chains for example: $-CF_2$-$CH=CF_2$ and $-CH=CF$-.

(iii) The EPR spectra, in Figure 3.3(a), shows the nature of the radicals in PVDF after irradiation under vacuum. In the PVDF, there is the appearance of alkyl radials (R$^\bullet$), radicals at the extremity of the chains ($-CF_2$-C$^\bullet$H$_2$) or ($-CH_2$-C$^\bullet$F$_2$) and radicals in the middle of the chains ($-CF_2$-C$^\bullet$H-CF$_2$) or ($-CH_2$-C$^\bullet$F-CH$_2$). When the radicals are in contact with the oxygene (*i.e.* at the end of the irradiation process), they recombine themselves producing peroxyl radicals (ROO$^\bullet$) (Figure 3.3(b)). [54]
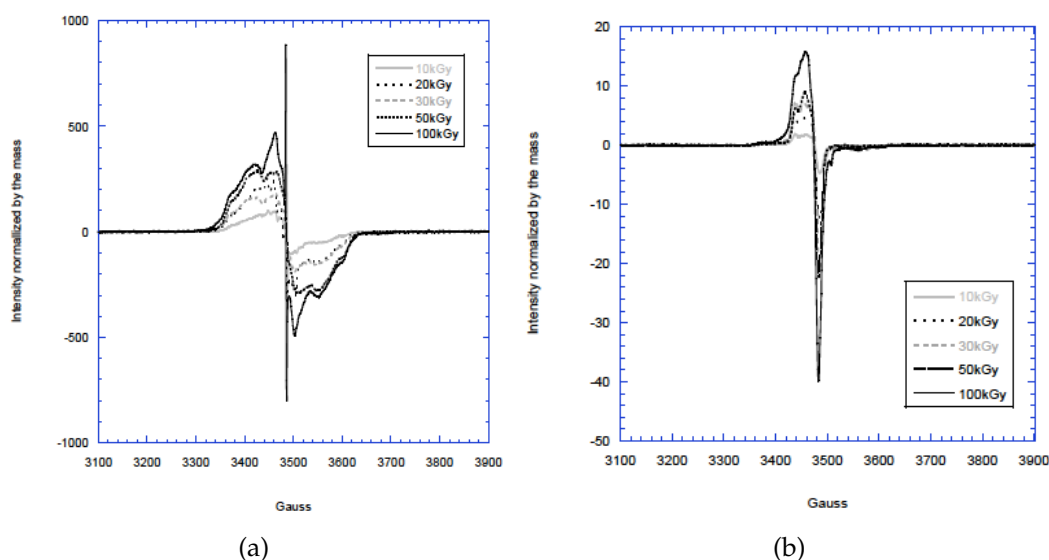
FIGURE 3.3: (a).Alkyl radicals in PVDF NPs irradiated under vaccum (2.5 MeV electron Van de Graaf accelerator); (b). Peroxy and alkyl radicals in PVDF NPs in presence of air.

3.2.4   Trapped radicals

Even if radicals are reactive, part of them may be trapped in the polymer for long periods, weeks or months after irradiation under certain conditions. The trapping time depends first on the radical stability and second on the material composition, its crystalline structure and its physical state when these radicals are created. Temperature is one of the most important parameter for the chains mobility and the trapping time.

The segments mobility may be facilitated depending of the range of the temperature considered respect to the glass transition temperature (T_g) of the polymer. Below the T_g, the amorphous phase is in the glassy state and the segment mobility is almost hindered. As a consequence, since radicals formed by irradiation mostly react through binary collisions, they may remain trapped and react slowly. Usually the polymer samples are conserved in liquid nitrogen for amorphous polymers and at -20°C for semi-crystalline polymers such as PVDF. The conservation at low temperature is necessary to preserve the concentration of the radicals, which are fundamental for chemical etching and grafting reactions.

Above T_g and below the melting temperature T_m, the amorphous phase is in its viscoelastic state and macromolecules mobility is enhanced. Then radicals react with the surrounding macromolecules and/or recombine. Primary radicals disappear or are replaced by more stable radicals.

3.2.5   Crosslinking

Macromolecular radicals created in polymers by irradiation evolve through recombination or rearrangements to give stable products. Among new bonds, resulting from these evolutions, there are: crosslinking, chain scissions and unsaturated bonds.

Crosslinking is defined as the formation of a new covalent bond, which can occur in one single chain (intrachain crosslinking, i.e., cyclization of the polymer, without molar mass change) or between two adjacent chains (interchain crosslinking, with molar mass increase). It requires doses generally comprised between 5 and 200kGy, and involves single steps or short kinetic chain length reactions. A typical mechanism of the interchain crosslinking in PVDF is described in the following reaction:

Ioniziong radiation

$$\Downarrow$$

$$\sim\!\!\sim\!\!\sim CH_2 \textemdash CF_2 \sim\!\!\sim\!\!\sim$$

$$\sim\!\!\sim\!\!\sim \dot{C}H \textemdash CF_2 \sim\!\!\sim\!\!\sim \qquad\qquad \sim\!\!\sim\!\!\sim CH_2 \textemdash \dot{C}F \sim\!\!\sim\!\!\sim$$

$$\sim\!\!\sim\!\!\sim CH \textemdash CF_2 \sim\!\!\sim\!\!\sim$$

$$\sim\!\!\sim\!\!\sim CH_2 \textemdash CF \sim\!\!\sim\!\!\sim$$
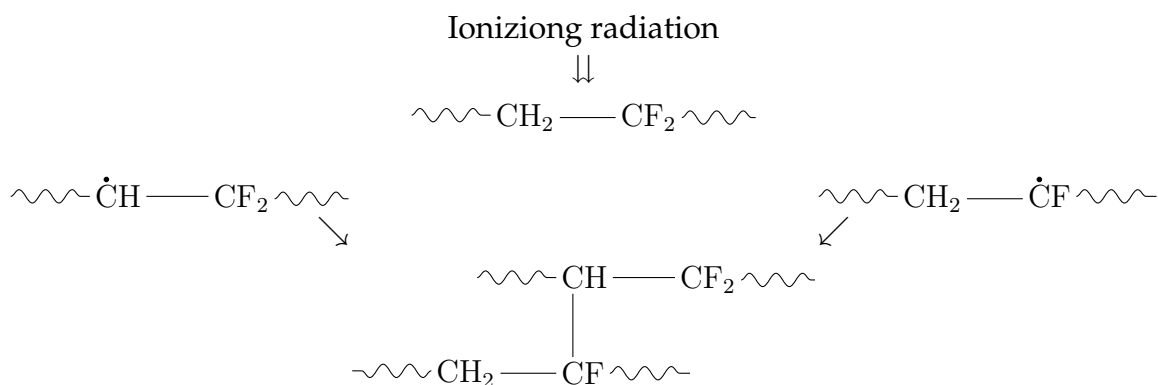
In this case, the homolytic rupture generates radicals along the chains and gas release (HF).

The starting dose for crosslinks is defined as *gel-dose*. For doses below the gel-dose, no crosslinks were observed. The gel-dose of PVDF is known to be in the range of 9.9-35.1 kGy. The corresponding interval of fluence is 1.9×10^9-4.9×10^9 cm^{-2}. [24] The concentration of crosslinks increases with dose, and the increase is not linear for the PVDF, as shown in Figure 3.4.
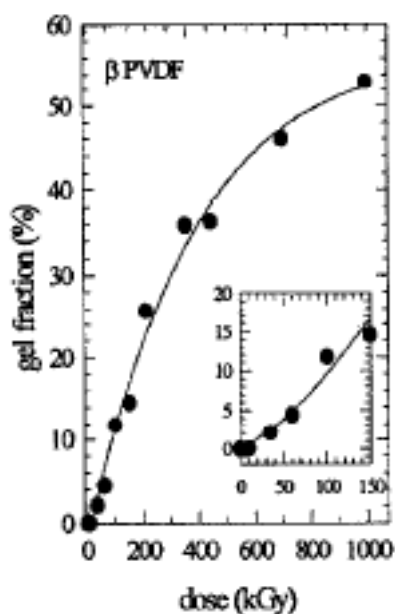
FIGURE 3.4: Evolution of the gel fraction as a function of the absorbed dose for the β PVDF [24]

As a consequence of the formation of covalent bridges between polymer chains at a specific temperature (network formation), elastomers or thermoplastics with a typical morphology and shape can be exposed to higher temperatures without melting. Generally, the crosslinked materials exhibit not only better mechanical and chemical properties, but also thermal and flame resistances. Radiation

crosslinking confers to polymers properties for instance of insolubility, infusibility, and a significant improvement of their dimensional stability in chemically aggressive and high temperature conditions.

Chapter 4

Ferromagnetism in nickel nanowire

In this chapter, I introduce the theoretical background to study the magnetization state of a ferromagnetic nickel nanowire considered as *mono-domain*. The nanowire is embedded in PVDF matrix. Thanks to the *magnetoresistance* properties, it is possible to access to the magnetization states of a nano-magnet *via* resistance measurements: *anisotropic magneto-resistance*(AMR) (section 4.2). By a theoretical point of view the magnetization states are obtained minimizing the total energy composed of three different terms: Zeeman, shape anisotropy and magnetoelastic energy. The total ferromagnetic energy will be define in section 4.4. A thermal source is used to deform the nanostructured system (Ni NW/PVDF). The PVDF deformation plays an important role in the amplitude and direction of the stress detected by the Ni NW. A mechanical description of the PVDF film will be presented in section 4.5.

4.1 Ferromagnetism

Ferromagnetism is define as the aptitude of certain materials to form a permanent magnet, or being attracted by magnets. The main source of ferromagnetism comes from a fundamental property of the electron, the magnetic dipole moment. Atoms with partially filled shells (*i.e.,* unpaired spins) may have a net dipole moment. In ferromagnetic material, in particular in transition metal (3d) such as (Ni) or cobalt (Co), the exchange interaction favors electrons with parallel spins resulting in a *spontaneous magnetization*, M_s. When the temperature rises beyond a certain point, called the *Curie temperature* (T_c) there is phase-transition from ferromagnetic to paramagnetic phase, with consequent loss of the spontaneous magnetization. Below T_c, the magnetic moments are oriented in an uniform direction within a region, called *Weiss domain*. The different orientation of the spontaneous magnetization in the Weiss domains lead to a macroscopically null magnetic moment in the material.

Magnetic materials are particularly interesting not only for their response to a

magnetic field, but also for their sensitivity to mechanical forces. In particular, the goal of this study is to measure the physical properties of single-contacted magnetic nanowires (NWs) embedded in an active thermoelastic polymer matrix. It is shown that a NW embedded in a matrix plays the role of a nanoscopic probe, which is sensitive to the amplitude and the direction of the mechanical stress.

4.2   Anisotropic Magneto-Resistance (AMR)

One of the physical effect explored in this work is the *Anisotropic Mangeto-Resistance* (AMR). Magnetoresistance is defined as the variation of the resistance in a ferromagnetic material due to the change of the magnetization states.

The anisotropic magnetoresistance is proportional to $\cos\theta$, where θ is the angle between the direction of the current and the magnetization $\vec{M}$, function of the applied magnetic field $\vec{H}$, as shown in Figure 4.1.
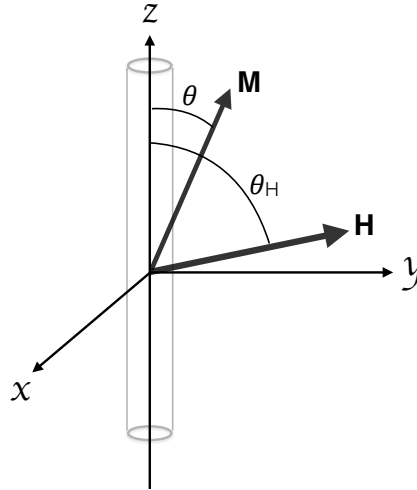
FIGURE 4.1: Orientation of the magnetization and external magnetic field respect to NW-axis.

The electric current density, J, inside the metal is constant and homogeneous along the wire in the direction $J = J_0 e_z$, where J_0 is constant. Consequently the direction of the current corresponds to the z-axis.

The expression that links the resistance of the Ni NW, R, with the applied magnetic field, H, is the following:

$$R(H) = R_0 + \Delta R_{max} \left(\frac{M_z(H)}{M_s} \right)^2 \tag{4.1}$$

Where: $M_z = M_s \cos\theta$, M_z represents the projection of the magnetization of the z-axis. ΔR_{max} is the maximum resistance variation due to AMR. R_0 is the

minimum resistance and corresponds to the magnetization perpendicular to the wire axis.

The AMR is defined as $\Delta R_{max}/R_0$ and it is expressed in percentage. In order to simply the notation the expression $\Delta R_{max}/R_0$ is re-write as $\Delta R/R$, as shown in Figure 4.2.
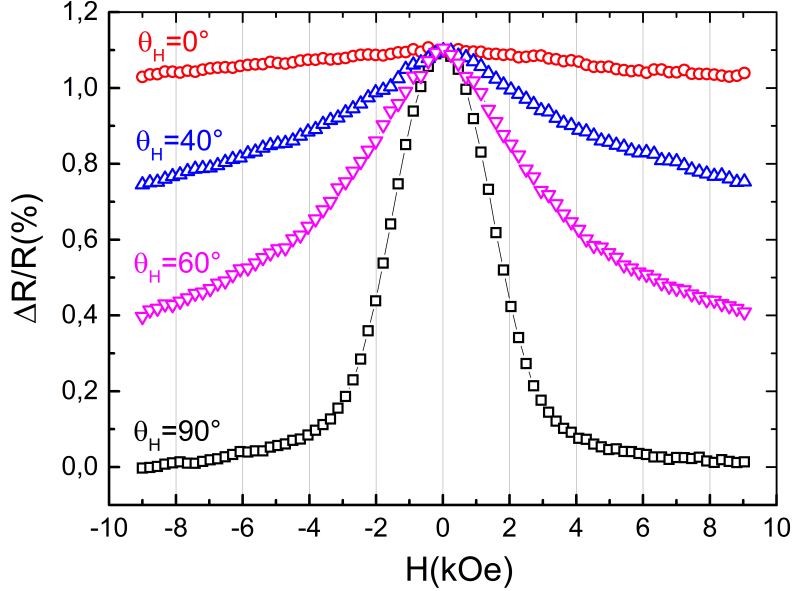
FIGURE 4.2: AMR at different θ_H.

A typical value for the AMR in the Ni NW is around 1%. We should note that the configuration with the applied magnetic field along the Ni NW axis, $\theta_H = 0$ stabilizes the magnetization along the same axis. The applied magnetic field at $\theta_H = 90°$ has the effect to rotate the magnetization from its original configuration toward the magnetic field direction. At saturation (magnetic field around 10kOe), the alignment between applied magnetic field and magnetization is complete. The component of the magnetization along z-axis, M_z is zero. Regarding the equation 4.1, the resistance of the Ni NW is minimum.

The anisotropic magnetoresistance (AMR) of single-contacted NWs are exploited in order to measure the magnetization states as a function of (i) the amplitude and angle of the applied magnetic field (θ_H), and (ii) the mechanical stress actuated by the matrix.

In the next section, we will define the energy terms involved in the determination of the magnetization states.

4.3   Components of the energy in a cylinder of infinite length

A cylindrical nanowire (NW) is described in this section. NW is a special nano-object where the length in the *z*-direction is predominant with the respect to the *x* and *y* directions. Due to the high aspect ratio and the nanoscopic size, the NW possess an uniform magnetization $\vec{M}$ along the *z*-axis: $\vec{M} = M_s \vec{e}_r$, where M_s is the saturation magnetization and $\vec{e}_r$ is the radial unit vector.

As we will discuss in section 4.3.1, the application of an external magnetic field (H), in a different spatial direction respect to the *z*-axis ($\theta_H \neq 0$), has the effect of change the orientation of the magnetization. The rotation of the magnetization is represented by the angle θ in Figure 4.3. A demagnetization field opposes to the rotation of the magnetization (section 4.3.3).

In presence of an external stress, on the Ni NW, another term should be considered in the analysis: the magnetoelastic field (H_{me}), defined by the angle θ_{me}. As already described for the external magnetic field, H_{me} acts to change the orientation of the magnetization from the axial position.
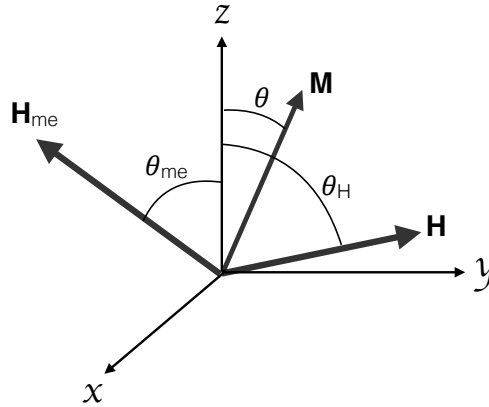
FIGURE 4.3: Orientation of the magnetization, magnetic and magnetoelastic field respect to NW-axis.

The orientation of the magnetization is described by the interaction between the magnetization and the effective H_{eff} magnetic field. H_{eff} represents either a magnetoelastic, demagnetization ,or the external magnetic field. The associate term of energy is given by the scalar product between the H_{eff} field and the magnetization: $E_i = -\vec{H}_{eff} \cdot \vec{M}$, where E_i represents either magnetoelastic, demagnetization, or Zeeman energy. In a physical point of view, all of these energy terms are defined for an infinite length cylinder that represents our NW. The total energy is given by the contribution of the single energy term involved in the system.

4.3.1 Zeeman energy density

The interaction between the external magnetic field, $\vec{H}$, and the magnetization is called Zeeman coupling:

$$E_z = -\mu_0 \vec{H} \cdot \vec{M} \tag{4.2}$$

referring to Figure 4.3 the Zeeman coupling becomes:

$$E_z = -\mu_0 H M_s \cos(\theta_H - \theta) \tag{4.3}$$

The term of the Zeeman energy is minimum when external magnetic field and magnetization are aligned.

4.3.2 Anisotropy energy

The anisotropy is related to the grain orientation in a ferromagnetic crystal. In particular, the energy involved to magnetize the crystal may be lower in certain direction rather than in others. The easy axis, corresponding with the minimum energy, in the case of Nickel, corresponds to the direction [111]. Furthermore, in the following study, the electrodeposited Ni NW is composed of randomly oriented nanocrystallites of about 10 nm, such that the magnetocrystalline anisotropy averages out to zero. The anisotropy is only due to the shape anisotropy (*i.e.,* it is due to the so-called 'demagnetizing field' or dipolar field). [55]

4.3.3 Shape anisotropy

Another term involved on the total energy is the *shape anisotropy*, also called *magnetostatic energy*. The presence of magnetic poles on the surface of the ferromagnetic material generates a so-called *demagnetization field*, $\vec{H}_d$. The demagnetization field, is generated by the magnetization $\vec{M}$ in a ferromagnetic material and it is opposite to the direction of the magnetization. The geometry of the system is also important. In the case of anisotropic system, we define $\bar{\bar{N}}$ as an anisotropic shape tensor. Consequently $\vec{H}_d = -\bar{\bar{N}}\vec{M}$. The resulting energy E_d is:

$$E_d = -\frac{\mu_0}{2} \vec{M} \cdot \vec{H}_d \tag{4.4}$$

As the energy E_d depends on the sample geometry, if we consider an ellipsoid system, $\bar{\bar{N}}$ is reduced to diagonal tensor with N_x, N_y, and N_z different from zero and the trace of the tensor is equal to 1:

$$N_x + N_y + N_z = 1 \tag{4.5}$$

Nanowires generally have a high aspect ratio and, in a physical point of view, we can consider them as cylinder with infinite length along z axis. The anisotropic component N_z is equal to zero. Thus, according with the expression (4.5) we obtain $N_x + N_y = 1$, and it implies that $N_x = N_y = 1/2$. The equation (4.4) becomes:

$$E_d = \frac{\mu_0}{4}(M_x^2 + M_y^2) \tag{4.6}$$

For a given ferromagnetic material the magnetization, M_s, is fixed. The components of M_s in the three-dimensional space are: M_x, M_y, and M_z. consequently:

$$M_s^2 = M_x^2 + M_y^2 + M_z^2 \tag{4.7}$$

So, we can rewrite the equation (4.6) as:

$$E_d = \frac{\mu_0}{4}(M_s^2 - M_z^2) \tag{4.8}$$

Considering the constant factor $M_s^2(\mu_0/4)$, the energy E_d becomes:

$$E_d = -\frac{\mu_0}{4}M_z^2 \tag{4.9}$$

In order to minimize E_d, the magnetostatic energy promotes the formation of domains in a ferromagnetic material with uniform magnetization inside. In the case of a cylinder of infinite length, the only domain possible is along the wire axis (*mono-domain*). The minimum of E_d is given by $M_s = M_z$ (magnetization along the wire axis).

If we express $M_z = M_s \cos\theta$, the equation (4.9) becomes:

$$E_d = -\frac{\mu_0}{4}M_s^2 \cos^2\theta \tag{4.10}$$

In the case of infinite cylinders (high aspect ratio), the shape anisotropy field for a NW is oriented along the wire axis $\vec{H}_d = H_d \vec{e}_z$

$$\vec{H}_d = \frac{M_s}{2}\vec{e}_z \tag{4.11}$$

Consequently we can write E_d as:

$$E_d = -\frac{\mu_0}{2} H_d M_s \cos^2 \theta \tag{4.12}$$

4.3.4 Magnetoelastic energy

When a ferromagnetic material is subjected to magnetic field, its dimensions change. This effect is called *magnetostriction*, and it is related to the reorientation of the magnetization. A magnetostriction strain λ is defined as:

$$\lambda = \frac{\Delta l}{l} \tag{4.13}$$

The maximum strain is called *saturation magnetostriction*, λ_s, and it occurs at saturation magnetic field.

A similar effect to magnetostriction, is called *inverse magnetostriction effect* or *magnetoelestic effect*. As the name 'inverse' suggests, the magnetization changes as a function of an applied stress, σ. We can express the magnetoelastic energy, E_{me}, as the interaction between a magnetoelastic field, H_{me} and the magnetization M:

$$E_{me} = -\mu_0 \vec{H}_{me} \cdot \vec{M} \tag{4.14}$$

In polycrystalline samples (*i.e.* electrodeposited nanowires), if the grain orientation are completely random, we can suppose an isotropic condition where the strain is equal in all the different directions: $\lambda_{100} = \lambda_{001} = \lambda_{si}$. We define λ_{si}, as the average of all the different directions. λ_{si} in polycrystalline nickel is equal to -3.10^{-5}.

If we suppose an isotropic magnetostriction the expression of the energy becomes:

$$E_{me} = -\frac{3\mu_0 \lambda_{si} \sigma}{2} M_u^2 \tag{4.15}$$

Where M_u is the projection of magnetization along an u-axis. We observe the minimum of the energy when $\vec{M}$ is aligned with u-axis. Considering the $H_{me} = E_{me}/M_s$ the expression of the magnetoelastic field becomes:

$$H_{me} = \frac{3\mu_0 \lambda_{si} \sigma}{2M_s} M_u^2 \tag{4.16}$$

The magnetoelastic field is proportional to the applied stress and the projection of the magnetization along the u-axis defined by θ_{me}.

4.4 Total ferromagnetic energy in Ni NW

Let us first ignore the magnetoelastic effect in a first approach. The magnetization states are defined by the external field and by the shape anisotropy only. In that case, the energy is defined by the two corresponding terms, the Zeeman coupling (equation E_z 4.3) and the shape anisotropy energy E_d (equation 4.12). Considering only these two terms of energy we obtain:

$$E(\theta) = E_z + E_d = -\mu_0 H M_s \cos(\theta_H - \theta) - \frac{1}{2}\mu_0 H_d M_s \cos^2\theta \qquad (4.17)$$

The quasi-static states of the magnetization are defined by the minimum of $E(\theta)$. Due to the cylindrical symmetry, all planes Π defined by the NW axis and the external fields H ($\theta_H = 90°$) are equivalent (the configuration space is reduced to the single variable θ). The quasi-static states of the magnetization are given by dE/dθ=0 and d^{2}E/d$^2\theta \geq$0.

If the $\vec{H}_{me}$ comes into play, the cylindrical symmetry becomes broken. The new configuration 3D is presented in Figure 4.4
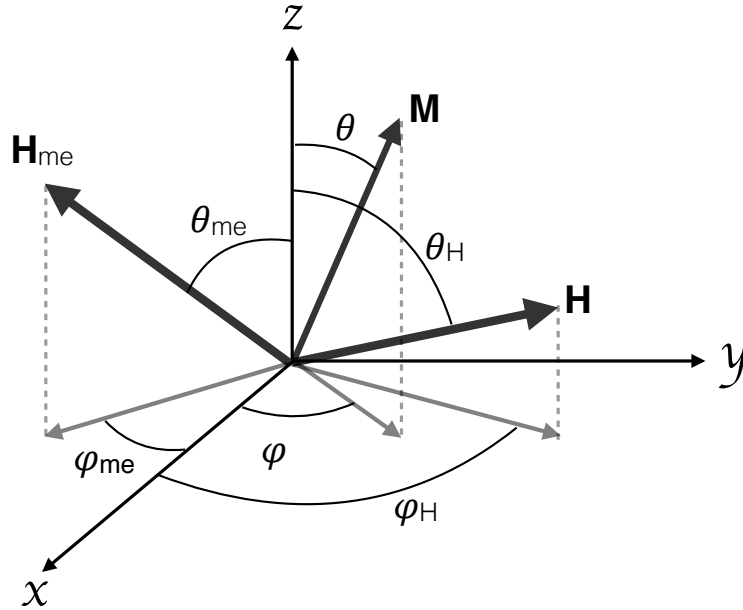
FIGURE 4.4: 3D orientation of the magnetization, magnetic and magnetoelastic field respect to NW-axis (z-axis).

The magnetization M must then be described by the coordinates (θ,φ) and and the external field by the coordinates (θ_H,φ_H). The Zeeman coupling reads now:

$$E_z = -\mu_0 H M_s(\sin\theta_H \sin\theta \cos(\varphi_H - \varphi) + \cos\theta_H \cos\theta) \qquad (4.18)$$

The direction of $\vec{H}_{me}$ is given by the coordinates (θ_{me}, φ_{me}). The contribution of the E_{me} becomes:

$$E_{me} = \frac{3\mu_0 \lambda_{si} \sigma}{2} \sin^2 \alpha \qquad (4.19)$$

The angle α (M) varies with the position of the magnetization. The magnetoelastic field can be defined by its amplitude $H_{me} = E_{me}/M_s$, consequently $\vec{M} \cdot \mu_0 \vec{H}_{me} = \mu_0 \cos \alpha$. The angle α is expressed by the relation:

$$\alpha = \arccos[\sin \theta_{me} \sin \theta \cos(\varphi_{me} - \varphi) + \cos \theta_{me} \cos \theta] \qquad (4.20)$$

Note that if we assume $\varphi = \varphi_{me} = 0$, then $\alpha = \theta_{me} - \theta$. The total energy is now the sum $E_t(\theta, \varphi) = E_z(\theta, \varphi) + E_d(\theta) + E_{me}(\theta, \varphi)$. The quasistatic states of the magnetization are calculated numerically by finding the minimum of the function $E_t(\theta, \varphi)$ for different values of the parameters {H,θ_H,φ_H}. [55] As shown in equation 4.19, the magneto-elastic energy is related to the total σ that acts on the Ni NW. In the next section, we discuss the origin of σ.

4.5 Thermo-elastic strain

The stress applied on the Ni NW is related to the strain in the PVDF film during heating. Indeed, the thermo-elastic strain generates a stress field around the Ni NW. The resulting stress is responsible to change the magnetization state in the Ni NW. In this section, we formulate a model to represent the stress in a transversely isotropic solid (bi-oriented PVDF film). In the transversely isotropic condition, the solid has a plane with identical elastic properties. The plane corresponds with the bi-stretched plane *xy* of the PVDF film. The stress field is represented by a spheroid.

On the other hand, an example of completely isotropic material will be provided. Polycarbonate (PC) is an amorphous polymer with characteristic properties of isotropic solid. Unlike bi-oriented PVDF, the stress developed in PC during thermo-elastic deformation is homogeneous in all the three directions of the space. The stress field is represented by a sphere.

The heating in the polymer film, obviously generates a strain (stress) in the Ni NW itself proportional to its linear coefficient of thermal expansion.

4.5.1 Transversely isotropic PVDF film

To confer a piezoelectric property to the samples, α-PVDF thin films have been stretched in the x and y directions (as described in material and method section). The elastic modulus in x and y directions result $E_x = E_y = 2,5 GPa$.
Transversely isotropic materials have a plane of isotropy in which the elastic properties are isotropic. If we assume that this plane of isotropy is the plane x-y, we can generalize the Hooke's Law $[\epsilon] = [C^{-1}][\sigma]$ as:

$$
\begin{pmatrix} \epsilon_{xx} \\ \epsilon_{yy} \\ \epsilon_{zz} \\ 2\epsilon_{yx} \\ 2\epsilon_{zx} \\ 2\epsilon_{xy} \end{pmatrix} = \begin{pmatrix} \frac{1}{E_x} & -\frac{\nu_{yx}}{E_x} & -\frac{\nu_{zx}}{E_z} & 0 & 0 & 0 \\ -\frac{\nu_{xy}}{E_x} & \frac{1}{E_x} & -\frac{\nu_{zx}}{E_z} & 0 & 0 & 0 \\ -\frac{\nu_{xz}}{E_x} & -\frac{\nu_{xz}}{E_x} & \frac{1}{E_z} & 0 & 0 & 0 \\ 0 & 0 & 0 & \frac{1}{G_{yz}} & 0 & 0 \\ 0 & 0 & 0 & 0 & \frac{1}{G_{yz}} & 0 \\ 0 & 0 & 0 & 0 & 0 & \frac{2(1+\nu_{xy})}{E_x} \end{pmatrix} \begin{pmatrix} \sigma_{xx} \\ \sigma_{yy} \\ \sigma_{zz} \\ \tau_{yx} \\ \tau_{zx} \\ \tau_{xy} \end{pmatrix} \tag{4.21}
$$

Where C^{-1} represents the compliance matrix in the transverse isotropic condition. In the hypothesis where $\sigma_{xx} = \sigma_{yy}$, and no shear stress ($\tau_{yx} = \tau_{zx} = \tau_{xy} = 0$) acts on the PVDF film, we can write the 4.21 as following:

$$
\epsilon_{xx} = \epsilon_{yy} = \frac{\sigma_{xx}}{E_x} - \frac{\sigma_{yy}\nu_{yx}}{E_x} - \frac{\sigma_{zz}\nu_{zx}}{E_z} \tag{4.22}
$$

$$
\epsilon_{zz} = -\frac{\sigma_{xx}\nu_{xz}}{E_x} - \frac{\sigma_{xx}\nu_{xz}}{E_x} + \frac{\sigma_{zz}}{E_z} \tag{4.23}
$$

By the equality between $\epsilon_{xx} = \epsilon_{yy}$, it results $\nu_{xy} = \nu_{yx}$. Thermal deformation involves the deformation of the membrane in three directions xyz. If we impose the condition of equal strain $\epsilon_{xx} = \epsilon_{yy} = \epsilon_{zz}$, under thermal deformation, consequently:

$$
\sigma_{zz} = \sigma_{xx}\frac{E_z}{E_x}\left(\frac{1 - \nu_{yx} + 2\nu_{xz}}{1 + \nu_{zx}}\right) \tag{4.24}
$$

We can group the constant term of the equation 4.24:

$$
A = \frac{E_z}{E_x}\left(\frac{1 - \nu_{yx} + 2\nu_{xz}}{1 + \nu_{zx}}\right) \tag{4.25}
$$

Consequently, the stress in z-direction becomes proportional to the stress in x or y direction:

$$
\sigma_{zz} = A\sigma_{xx} \tag{4.26}
$$

We are able to calculate the A coefficient. Bi-oriented PVDF film shows a large Poisson ratio due to orientation of the β crystallites in the *xy* plane: $\nu_{zx} \simeq \nu_{xz} \simeq 0.6$. As effect of the orientation, $\nu_{yx} = 0.35$. [56, 57]

The transversal modulus E_z is measured by ultrasound technique and it is equal to 5.8 GPa. Introducing these values in equation 4.25 we obtain A=2.76.

In summary, we can represent the stress field around the Ni NW as a spheroid. In particular, The coefficient A>1 allows to define a *prolate* spheroid: $\sigma_{xx} = \sigma_{yy} < \sigma_{zz}$ (Figure 4.5).
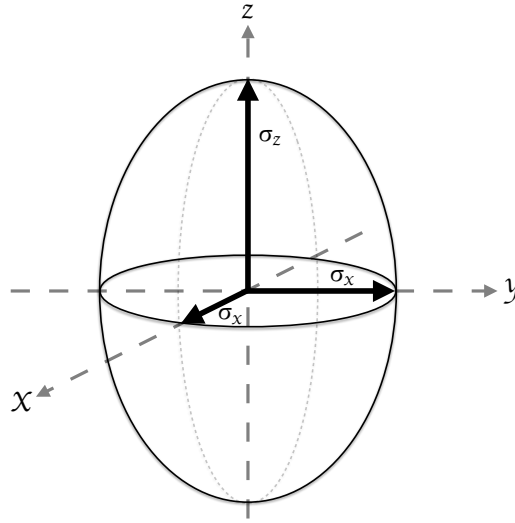
FIGURE 4.5: Prolate-spheroid shape of β-PVDF stress σ occurring in the polymer film during thermal expansion.

The thermo-elastic strain in the bi-oriented PVDF film is expressed by the relation:

$$\epsilon = \alpha \Delta T \tag{4.27}$$

Where ΔT, ϵ, and α_i are respectively the temperature difference, the strain and the linear thermal coefficient $\alpha = 9.99.10^{-5} K^{-1}$.

4.5.2 Isotropic PC film

Isotropic solids have equal elastic properties in the three directions. In PC $E_x = E_y = E_z = E$. If we consider an homogeneous thermal heating around the polymer film, we can suppose an equal thermo-elastic strain in all the three spatial directions $\epsilon_x = \epsilon_y = \epsilon_z = \epsilon$. Consequently to the Hooke's Law, the stress $\sigma_x = \sigma_y = \sigma_z = \sigma$. We can write the resulting σ as follows:

$$\sigma = \frac{\epsilon E}{(1 - 2\nu)} \tag{4.28}$$

substituting ϵ with the expression $\epsilon = \alpha_{PC}\Delta T$:

$$\sigma = \frac{\alpha_{PC}\Delta T E}{(1 - 2\nu)} \tag{4.29}$$

Where ν is Poisson's ratio, $\alpha_{PC} = 9.45.10^{-6}$ is coefficient of thermal expansion of the PC, and ΔT is the temperature difference. The stress field is isotropic around the Ni NW and it is represented by a sphere.

4.5.3   Thermal dilatation of the Ni NWs

During the heating process, not only the polymer film is affected by thermal dilatation. In particular, the strain along the Ni NW (z axis) is not negligible. Following the Hook's law, The strain in the PVDF is proportional to the thermal stress. Although the elastic modulus is independent of heating, for nano-object, it becomes much larger than in the bulk. The increase of the elastic modulus is related to the *surface tension γ_s*. The elastic modulus of the Ni NW is evaluated using the relation:

$$E_{ap} = E + \frac{\gamma_s(1 - \nu)8L^2}{5D^3} \tag{4.30}$$

where ν is Poisson coefficient, E Young's modulus of the bulk, L the length of the NW and D the diameter of the NW. The surface tension γ_s varies as function of the temperature as follows:

$$\gamma_s(T) = \gamma_L + \gamma_T(T - T_L) \tag{4.31}$$

where γ_L is the surface of the material at the melting temperature T_L, and γ_T the thermal coefficient of the surface tension. Using the values $T_L = 1454K$, $\sigma_L = 1.77$ and $\sigma_L = -3.310^{-4}N.m^{-1}.K^{-1}$ in equation 4.31, we obtain $2.15N.m^{-1}$ at 293K for the surface tension of the Ni NW. The young modulus for Ni bulk is 283 GPa. For a Ni NW of $9\mu m$ length and 75 nm in diameter, the apparent elastic modulus calculated from equation 4.30 is 745 GPa. [55] The thermo-elastic strain has also to be considered. The strain $\Delta L/L$ is equal to:

$$\frac{\Delta L}{L} = \alpha_{Ni}\Delta T \tag{4.32}$$

where α_{Ni} is the linear coefficient of thermal expansion for Ni ($13.10^{-6}K^{-1}$ at room temperature) and ΔT is the difference of the temperature. Considering the high aspect ratio of the Ni NW, we can neglect the deformation in x and y directions. Ni NW is electrodeposited in the cylindrical pores of the track-etched

polymer film, and it is bounded inside the film. The resulting stress σ_z^w is a compression along the axis. The corresponding stress will be:

$$\sigma_z^w = \alpha_{Ni} \Delta T E_{ap} \qquad (4.33)$$

In conclusion, if we take into account each term of stress generates by the polymer film and the Ni NW under thermal dilatation, the intensity and direction of the resulting stress is theoretically tough to solve. In our case, we propose a relative simple method based on the interaction between the thermo-elastic stress (matrix plus Ni NW) and magnetization states of the Ni NW. The effect of the thermo-elastic strain on the Ni NW will be discussed in 'results and discussion' chapter.

Part II

Chapter 5

Materials and Methods

The objective of this chapter is to give an overview of all the necessary steps to realized a single contact nanowire embedded in the PVDF film, and the main magnetic measurement used to characterized it.

Section 5.1 gives a description of PVDF film used in this study. Therefore, in the first part of the chapter, we report the three main steps used to realize a single-contact nanowire: SHI irradiation and chemical etching of the PVDF film, and electrodeposition of the single-contacted Ni NW, respectively. In the second part of the chapter, the magnetic measurements are listed. In particular, the experimental set-up to measure the AMR will be presented in section 5.5.1. The AMR is measured as function of: the external magnetic field (5.5.2), the angle θ_H (5.5.3), and thermo-elastic stress generated by heating (5.5.4).

5.1 Bi-oriented polarized PVDF film

Bi-oriented and polarized PVDF films were purchased from PIEZOTECH SA (thickness: h = 9 μm). PVDF is obtained by radical polymerization of vinylidene fluoride ($CH_2 \!=\! CF_2$). The polymerization is performed in emulsion in the presence of catalysts. Then, the film is obtained by extrusion. PVDF polymorphism is well-known and consists in four crystalline phases, named α, β, γ, and δ, as already described in section 2.9.

The orientation of the chains, inside the crystalline parts, is in form of *lamella*. The thickness of the lamella is around 10 nm. [58] Cooling down melted PVDF, part of the polymer tends to crystallize in form of α spherulites. The aggregation of the lamellae is radial respect to the center of nucleation. Between the lamellae, part of the polymer is in the amorphous state. The size of the spherulites is between 10^{-6} and 10^{-3} m.

α-PVDF is transformed in β-PVDF by stretching. The stretching is performed a at temperature below 100°C, with stretch ratio between 3 and 5. [59] In these conditions the spherulites are deformed in direction of the stress. In the first step,

the spherulite deforms in an ellipsoid. Successively, the blocks of lamellae continue to deform until forming a fibrillar structure of crystallites (Figure 5.1). This mechanism change the structure of the crystalline part in all-trans planar zigzag conformation (β-phase). The fibrillar-structure is aligned in direction of stress with a thickness around 10nm and 1-5 μm in length.
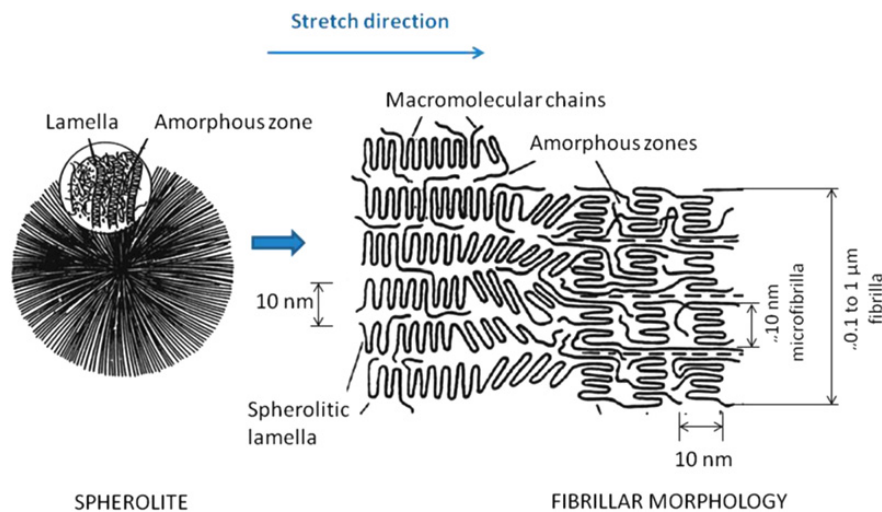
FIGURE 5.1: impact of the deformation on the spheruite

X-ray diffraction (XRD) spectra of α and β-PVDF are shown in Figure 5.2. You should note the disappearance of the two alpha peaks at $2\theta = 17.869$ and $2\theta = 18.392$, respect to the bi-oriented configuration. Consequently, there is the formation of a beta phase with a double peaks at $2\theta = 20.688$ and $2\theta = 20.828$. In bi-oriented PVDF film, the only trace of alpha phase is the peak at $2\theta = 20.119$.
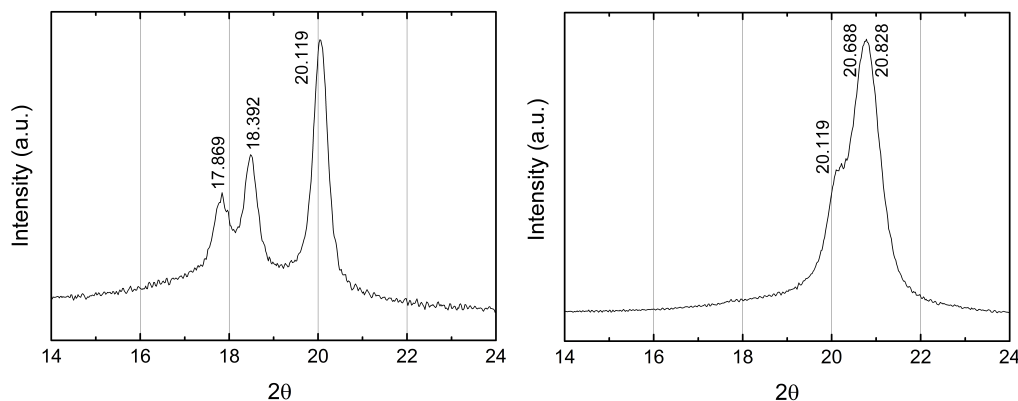
FIGURE 5.2: Left: XRD spectrum of α-PVDF. Right: XRD spectrum of bi-oriented β-PVDF

The film results in transversally isotropic solid as described in section 4.5.1.

5.2   SHI Irradiation

SHI irradiation is used as the first step to nanostructure our PVDF film. SHI irradiations were performed at GANIL, France. Films were irradiated at room temperature with $_{136}Xe^{48+}$ or Kr^{36+} at energy between 7.46 and 10.37 MeV.amu^{-1} (according with the conditions described in section 3.1.3), under He atmosphere. The use of $_{136}Xe^{48+}$ or Kr^{36+} is equivalent in terms of homogeneity of the latent-track. PVDF films (4 cm width × 30 cm length) were fixed on movable sample holders (speed rate 0.06 m.min^{-1}). Fluencies were adjusted taking into account the number of passages and the ion-beam flux. Studied fluence: $10^9.cm^{-2}$. The film was oriented perpendicular to the ions trajectory. For fluence of 10^9, four more irradiation angles have been performed: $15°$, $30°$, $45°$, and $60°$ (respect to the film surface).

5.3   Chemical etching

The latent-tracks, obtained by SHI irradiation, are revealed by chemical etching. Many parameters are involved in this step: nature of the sample, its thickness, irradiation condition, concentration of the attack solution, etching temperature, etching time etc. All of these parameters make, the track reveling, a complex process. An empirical way was used to evaluate the optimal attack condition: one should fix the concentration of the chemical etching solution, the temperature, and the size of the sample. A calibration of etching time *versus* porous diameter by FE-SEM imaging is presented in section 8.4.

Chemical attack is performed at 65°Cin a solution of KOH 10N and KMnO$_4$ 0.25N. The final diameter depends of the etching time. Afterwards, etched PVDF film were first washed in potassium disulfite solution (15%) and then 3 times rinsed with deionized water.

The mechanism of the etching reaction leads to depolymerization by hydrolysis with homolytic rupture. Following to the SHI irradiation, part of the radicals recombine to give double bonds. The KMnO$_4$ interacts with the double bond leading to intermediate species (precursors of glycol related compound, in mild condition) with two oxygen bridges between Mn and C (Figure 5.3).

Then, KOH intervenes to hydrolyze the intermediate, breaking the covalent bond between the two carbons (depolymerization by oxidative cleavage of glycols) and producing a green residual (K$_2$MnO$_4$). Consequently, another double bond in main chain is generated and the reaction continues (concerted reaction).
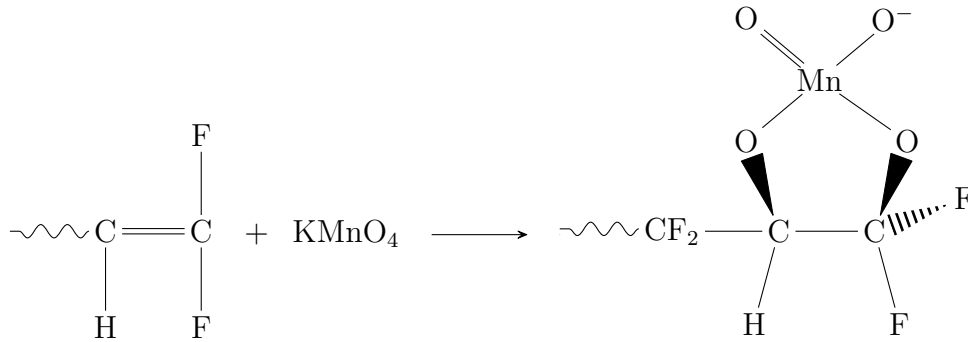
FIGURE 5.3: Typical reaction mechanism between double bond in
PVDF chain termination and Potassium permanganate

The size of the pores in PVDF is proportional to etching time. The shape of the
pore is cylindrical. The etching time used, in our study, was set to 30 minutes and
it corresponds to 50 ± 10nm in diameter.

5.4   Electrodeposition: potentiostat mode

Electrochemistry studies the chemical reaction at the interface of electrolyte and
electrode. The electrolyte is an aqueous solution contain metal ions. The electrode
is a conductor surface in contact with the electrolyte. The typical electrochemical
reaction is:

$$M^{n+} + ne^- \rightarrow M\bullet \tag{5.1}$$

The deposition of the metal is a reduction, where the ions, M^{n+}, are able to
transform themselves in metal ($M\bullet$), when they come in contact with the elec-
trode surface.

A typical experimental set-up for electrodeposition involved three electrodes con-
nected with a potentiostat. The working electrode (WE) is our cathode (where the
reduction takes place); the potential of the working electrode is measured respect
to reference electrode (RE); in order to maintain a constant potential between WE
and RE , it needs a further electrode: counter-electrode (CE) .

The CE and WE are in gold, and the RE electrode is Ag/AgCl (reference: *Calomel*
electrode).

In potentiostatic mode, the potentiostat applies a potential between WE and CE
in order to maintain the desired potential between WE and RE electrodes. At
the same time, the potentiostat registers the current circulation between WE and
CE. The potentiostat is connected to the computer, and the deposition current is
continuously registered .

5.4.1 Sample preparation

The nanoporous PVDF is covered with gold layer on both sides. On one side the gold layer has a thickness of 200 nm, and it represents the cathode during the electrodeposition. We chose a gold layer of 200 nm to ensure the complete blocking of the pores. The thickness of the gold layer, on the opposite side, is around 32 nm. In this case, the pores are not blocked and the electrolyte ions pass all along the nanopores to reach the cathode. The presence of this gold layer alerts us when the first Ni NW reaches the surface. Indeed, when the two gold layer are in contact, we register a current peak that indicates the single contact.
The gold layers are sputtered using the cathode sputtering coater QUORUM-Q150T S. The system is coupled with a vacuum pump, and the air inside the chamber is replaced with argon. Gold particles are ejected from a solid target due to bombardment by energetic ions of Ar^+ plasma. The sputtered gold layer thickness is function of the exposition time. Using a current deposition of 20 mA, the time required to sputter 32nm is 134 seconds (deposition rate of 0.26 $nm.s^{-1}$). In our device, the surface covered by the gold layer is the same for both side (around 0.81 cm^2). The shape of the layer is circular (radius 3mm).
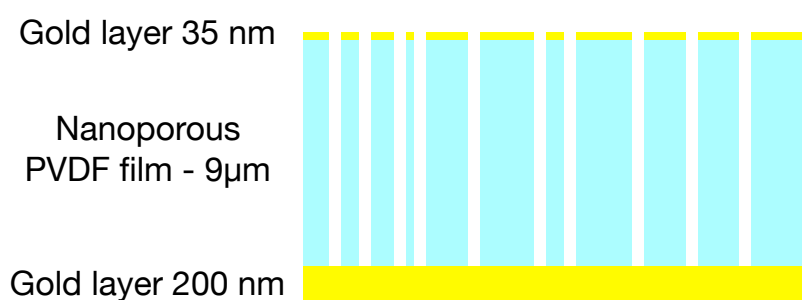
FIGURE 5.4: Nanoporous PVDF with double gold layer

After the electrodeposition, further manipulations on the PVDF film may be catastrophic; in fact, due to its high aspect ratio, the NW is very fragile. Therefore, before the electrodeposition, it is important to fix the film on a specific sample holder.
The sample holder is a printed silicate plate with four copper strips joined on four pins. Inserted in the sample holder, a peltier plate is also present (Figure 5.5(a)). This configuration allows to connect directly the four pins on the measurement device. As shown in Figure 5.5, there are different steps to prepare the sample for the electrodeposition:
(i) One side of the film, with the thicker gold layer, is in contact with the Peltier plate. Two silver wires were used to contact the gold layer with the pins 3 and 4. Instead, the thinner gold layer (on top) is connected with the pins 1 and 2. The

silver wires were fixed by silver paint (Figure 5.5(b));

(ii) Kapton tape is used to seal the sample holder and avoid the electrodeposition on the copper strip. The only part exposed to the electrolyte is that one where the electrodeposition takes place (Figure 5.5(c)). Paraffin is used on the edges of the sample holder to ensure a proper sealing.
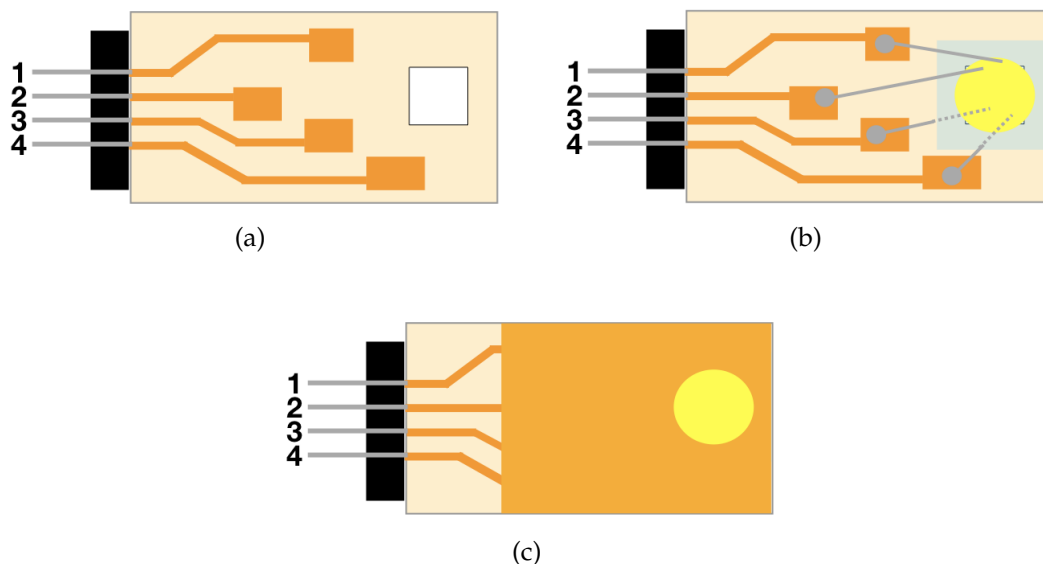
FIGURE 5.5: Preparation sample for electrodeposition: (a) printed silicate plate with peltier plate (white square in the figure); (b) PVDF film is fixed on the peltier plate and four Contacts are provided for each pin; (c) The contacts are protected by kapton tape. Only a small area is exposed to the electrolyte.

At this point, our sample is ready for the electrodeposition.

5.4.2 *In-situ* electrodeposition of a Nickel NW

Ni NW is grown by electrochemical process. The electrolyte solution consists of 65g $NiSO_4$ and 15g H_3BO_3 in 500ml of water. The electrodeposition is performed using the potentiostat/galvanostat, HEKA PG310. The sample is connected by the pin 4 to the potentiostat, and the uncovered part of the sample is immersed in the electrolyte bath (Figure 5.6). The potentiostatic mode is used. The typical potential used for the electrodeposition of the Ni is -1V.
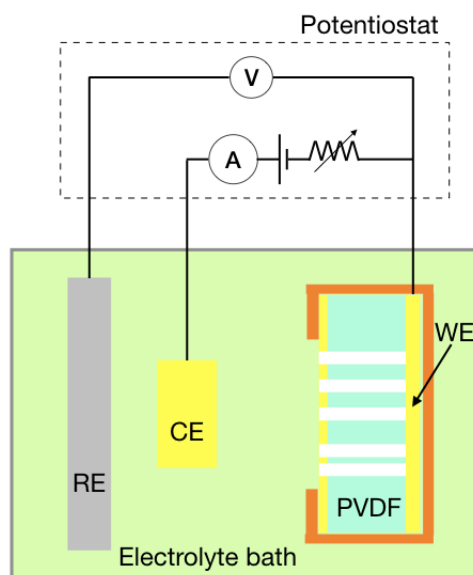
FIGURE 5.6: *In-situ* electrodeposition of a single Ni NW

The electrodeposition current is measured between CE and WE. During the electrodeposition, we register the current function of the time. Figure 5.7 shows the profile of electrodeposition current function of the time.
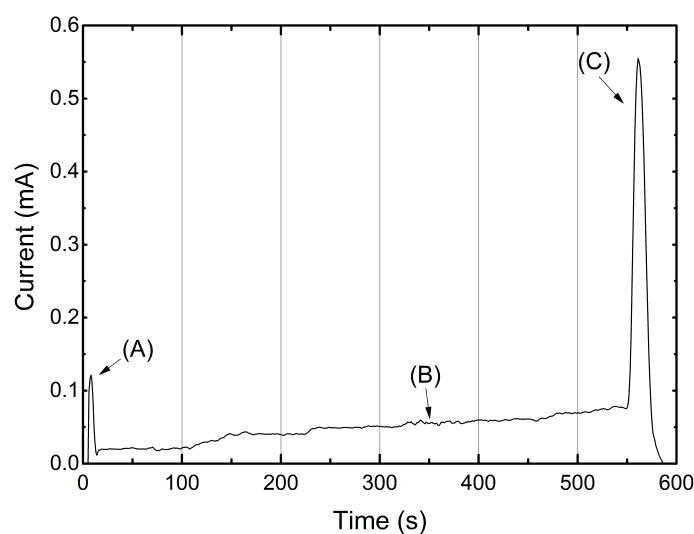
FIGURE 5.7: Electrodeposition *vs* time

We can divide the plot in three different region. The first peak indicates with (A), in Figure 5.7, is due to charge accumulation relative to the first reduction of the nickel on the cathode. Afterwards, the electrodeposition current progressively increases because the number of nanowires nucleations increase (B). When the first nanowire reaches the surface, the Ni NW generates a short-circuit between the top and bottom electrodes. Consequently, the cathode electrode surface is extended to the top gold layer. The sudden increase of the deposition surface

generates a high peak current (C). This final peak is the sign that one nanowire is contacted and we must immediately stop the electrodeposition process.

5.5   Magnetic Measurement

In this section, we describe the experimental set-up used to characterize the single-contacted Ni NW. Following, we describe the measurement protocol of the magnetization states as a function of: (i) the amplitude and angle of the applied magnetic field; (ii) the mechanical stress actuated by the thermo-elastic strain of matrix.

5.5.1   Experimental set-up

The experimental set-up, used for our experiment, is shown in Figure 5.8. The current for the electromagnets was supplied by generator. The maximum current supplied by the generator is 80 A. The intensity of the magnetic field applied to the sample depends of the intensity of current provided to the coil. The maximum value of magnetic field, at 80 A, is $\mu_0 H \simeq 2.3T$. The conversion is $\simeq 29 mT.A^{-1}$. The sample is inserted into the air gap of a 1 T (10 kOe) dipolar field. The magnetic field intensity is controlled by a voltage generator *YOKOAMA 7651*.

The sample, prepared as described in section 5.4.1, was connected with the experimental set-up through the four pins of the sample holder. The pins **1** and **4** were used to inject DC current in the single Ni NW. The intensity of the current supplied is in the range between 10 and $30\mu A$. The current source is the *Keithley 224 programmable current source*. The remaining pins, **2** and **3**, were used to measure the voltage. The tension variation in the Ni NW is measured by *Keithley 2182A nanovoltemeter* with an intrinsic noise of 25 nV in a range below 10 mV. The increasing of temperature in the sample is supplied by a Peltier plate placed below the PVDF film. The Peltier plate is connected to the *Keithley 2611A SYSTEM Source Meter*. All the instrument are managed by computer *via* GPIB. *LabVIEW* is used to control the instruments, and register the data.
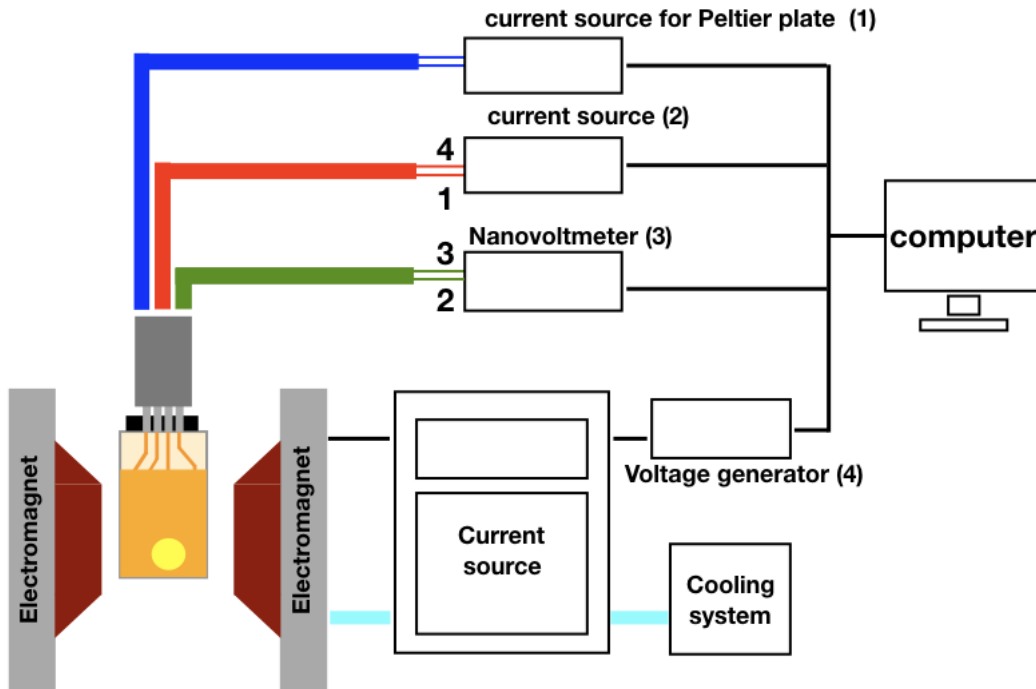
FIGURE 5.8: Experimental stet-up. (1) - Keithley 2611A SYSTEM
Source Meter; (2) - Keithley 224 programmable current source;
(3) - Keithley 2182A nanovoltemeter; (4) -YOKOGAWA 7561 pro-
grammable DC source

5.5.2 AMR function of external H

DC current is injected in the Ni NW by pins **1** and **4**. Fixing the angle θ_H, we per-
form the AMR measurement varying the intensity of the external magnetic field.
In particular, the magnetic field intensity changes between -10 kOe and 10 kOe
with 100 Oe step. We define one loop as the variation of the external magnetic
field from -10 kOe to 10 kOe and going back. Fixed the angle θ_H, five loops were
performed. The resulting AMR is the arithmetic average for each point.
The voltage is measured between the pins **2** and **3**. The configuration at four
pins, allows to disregard the contact resistance (silver paint-copper strip and sil-
ver paint-gold layer). Therefore, we measure the proper voltage on the Ni NW.
The resistance of the Ni NW is relative to the nanowire diameter. Indeed, $R = \rho L/S$, where ρ is the electrical resistivity of the nickel, L and $S = \pi r^2$ are the
length and the area of the NW, respectively. Considering $\rho = 6.99.10^{-8}\Omega.m$,
$L = 9.10^{-6}m$, and a diameter between 40 and 60 nm the corresponding resis-
tance varies between 500 and 200Ω. Sometimes the value of resistance was found
to be lower than 200Ω or higher than 500Ω. In the first case, during the electrode-
position, we can suppose that many nanowires are contacted in parallel and this
contributes to reduce the global resistance. On the other hand, resistance higher

than 500Ω could be ascribed to a bad contact between the gold layer and the Ni NW.

In order to get a good signal/noise ratio, the range of the nanovoltmeter is limited to 10 mV. If we consider a resistance of the Ni NW around 300 Ω, the maximum injected current should be lower than 30 μA. In this condition, the signal/noise ratio will be $15nV/5mV \simeq 5.10^{-6}$.

During the measurement of the AMR, very often the first value of resistance not matches with the final value obtained at the end of the loop. This phenomenon is called *drift* and it attributes to the electromigration at high current density. In the case of linear drift, a linear transformation is enough to correct the signal. To avoid large fluctuations of resistance during the measurement, it is recommended to dry the sample for 3-4 hours after electrodeposition.

5.5.3   AMR function of θ_H

In this section, we present the angular dependence of the resistance with the magnetization. As we already introduced in section 4.2, the magnetization of the Ni NW depends on the external magnetic field. Therefore, we can express the AMR of Ni NW as a function of the angle θ_H, at saturation field.

Our sample holder is inserted in a rotational support Figure 5.9. The sample may rotate of 360°, but in our case, the rotation is limited between 0° (NW aligned the magnetic field) and 90°.
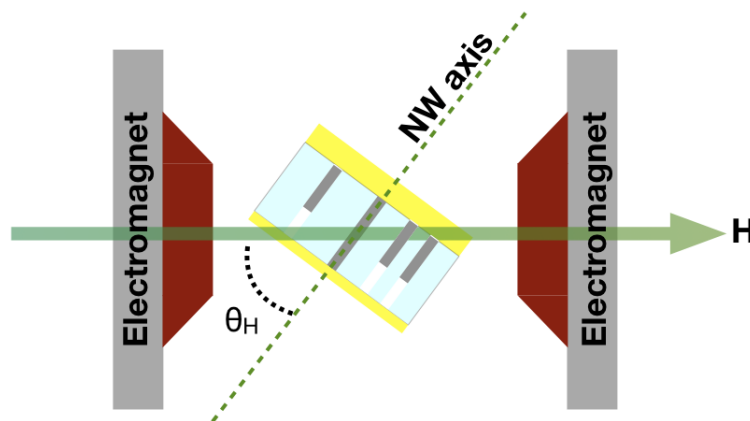
FIGURE 5.9: Rotation system for AMR characterization, function of the angle θ_H

Figure 5.10 shows the typical AMR of the Ni NW function of θ_H for a fixed value of magnetic field.
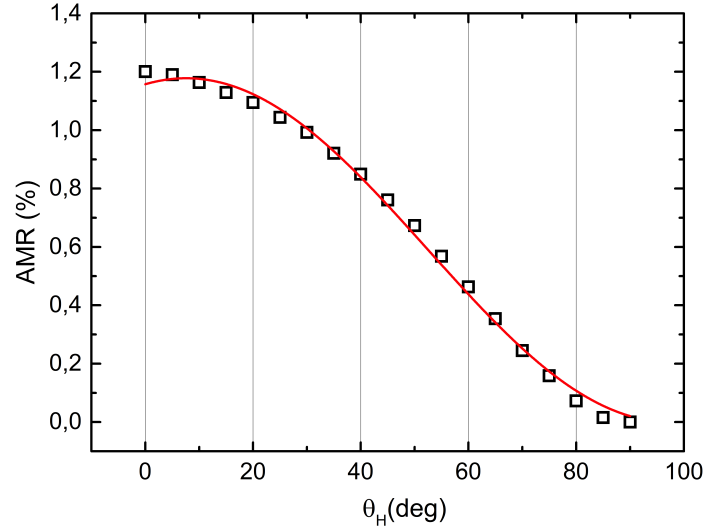
FIGURE 5.10: AMR *vs* θ_H (H=10kOe). Fit function: $1.178cos^2(\theta - 7.57)$.

The angle θ_H varies from 0° to 90° and from 90° to 0° with step of 5°. The magnetic field is fixed at 10kOe (saturation field) and the injected current in the Ni NW is 10μA. For each angle, the resistance value is the arithmetic average of 10 points. The fit function is $(\Delta R_{max}/R_0)cos^2(\theta - \theta_0)$. Where $\Delta R_{max}/R_0$ is the AMR at saturation field, θ_0 is the phase shift related to the alignment errors between the sample holder and the experimental set-up, and θ is the angle between NW axis and magnetization. At saturation field $\theta = \theta_H$, the magnetization is aligned (at each angle) to the external magnetic field.

5.5.4 AMR under applied ΔT

The membrane is heated by a Peltier plate placed in the sample holder and connected to the a generator source. The difference of temperature was calculated by the Ni NW with the following equation:

$$R(T) = R_{amb}[1 + \alpha_m(T - T_{amb})] \tag{5.2}$$

Where T is the NW temperature, T_{amb} is the room temperature, R_{amb} is NW resistance at room temperature, R(T) is the NW resistance at temperature T, and α_m is the temperature coefficient of resistance, for the nickel α_m =0.005866.
The current injected in the Peltier plate varies between 0 and 0.3A. Fixing the injected current in the Peltier plate, we measure the resistance in the Ni NW. The measurement of resistance was registered after 5 minutes since we turned on the current source on the Peltier. This delay is necessary to the stabilization of the resistance in the nanowire with the temperature variation.

Figure 5.11 shows the variation of ΔT function of the current injected in the Peltier plate. The room temperature was measured equal to 21°C. The injected current in the Ni NW was $10\mu A$. In order to prove the calculation of the ΔT based on the resistance of the Ni NW, we measure experimentally the ΔT in the Peltier plate using a thermocouple. The thermocouple was fixed by tape in intimate contact with the Peltier plate and connected with a voltmeter. The ΔT measured experimentally are compared with the ones calculated by the equation 5.2. The measured data are inside the error bar of the calculated ones. The indirect calculation of the ΔT is in agreement with the measurement.
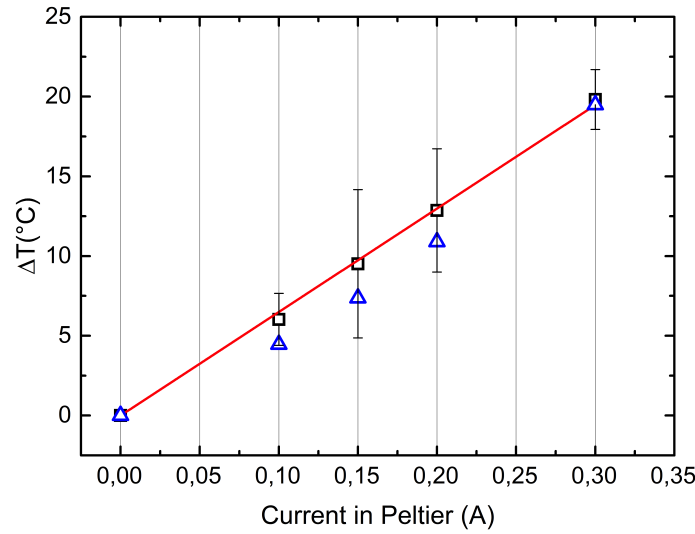
FIGURE 5.11: ΔT *vs* injected current in the Peltier plate. Calculated data ($\square$); measured data ($\triangle$)

The measurements of AMR, under heating condition, are performed at fixed angle $\theta_H = 90°$, as illustrated in section 5.5.2.
We can re-write the equation 4.1 as:

$$\frac{R(H) - R_0}{R_0} = \frac{\Delta R_{max}}{R_0}cos^2\theta \tag{5.3}$$

The term $\Delta R_{max}/R_0$ is not depending on the temperature. We can demonstrate it, reproducing the AMR curve function of θ_H (shown in Figure 5.10) with an applied ΔT around 19°C. Despite the increase of R_0, due to the ΔT, the value of the $\Delta R_{max}/R_0$ remains constant (variation less than 10% in Figure 5.12) compared with that one at room temperature.
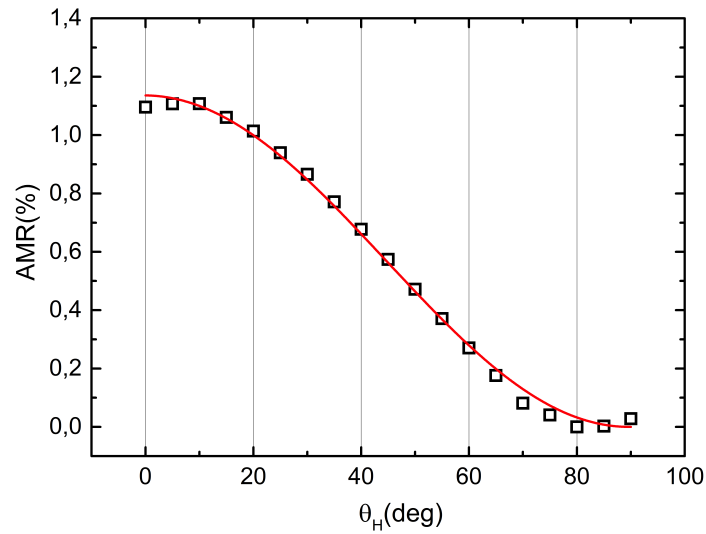
FIGURE 5.12: AMR *vs* θ_H at $\Delta T \simeq 19°C$(H=10kOe). Fit function: $1.136cos^2(\theta + 0.504)$.

On the other hand, for values of the external magnetic field different from the saturation, this hypothesis is not true. The magnetization is not aligned with the external magnetic field ($\theta \neq \theta_H$). Therefore, the AMR becomes function of the magnetization. Consequently, for external magnetic field equal to zero the magnetization may not be aligned with the demagnetization field along the NW axis ($\theta \neq 0$) due to the magnetoelastic effect.

Chapter 6

Results and discussion

Magnetic materials are particularly interesting not only for their response to a magnetic field, but also for their sensitivity to mechanical forces. We report a systematic study of the physical properties of single-contacted magnetic nanowires (NWs) embedded in an active thermoelastic (PC and PVDF) and piezoelectric polymer matrix (PVDF).

The goal of this study is to use a single Ni NW as a probe in order to measure the amplitude and direction of a mechanical stress exerted, at the nano-scale, by the polymer matrix during its deformation. In the first part of this chapter, I will present the results relative to thermo-elastic deformation in the nano-composite PC/single Ni NW. The incident of the temperature on the coercivity of AMR curves will be illustrated. A coplanarity model will be discussed to explain the relation between magnetization states of the Ni NW and stress exerted by the PC film (section 6.1).

This study shows how the properties of the polymer film plays a key role in the variation of the AMR signal. Motivated by this result, PVDF has been chosen to exploit the inverse piezoelectric effect as way to exert a stress on the Ni NW. An unexpected decrease of the amplitude of the AMR signal with the applied DC voltage was observed (section 6.2). Further investigations were made them difficult due to the high level of noise introduced by the DC voltage during the measurement. An alternative has been found using a Peltier plate as a thermal source to deform the PVDF film. The decrease of the AMR amplitude was confirmed. An energetic model will be proposed to explain the configuration out-of-plane of the magnetization (section 6.3).

In conclusion, an angle investigation will be also proposed to confirm the out-of-plane configuration in section 6.4.

6.1 Thermo-mechanical effects in PC

The effect of the temperature in the AMR curves was investigated in a nano-composite PC film/single Ni NW. The nanostructuration of the PC consists in different steps: SHI irradiation, chemical etching and electrodeposition (techniques and parameters described in the chapter 5). In this first study, the PC film was deformed by thermal source using a coil, placed under the PC film. The AMR reference was traced at room temperature ($T_0 = 290K$). The increase of T deforms the PC film. The deformation is detected by the Ni NW as a compressive stress. The most evident effect of the stress is a change of the coercivity (width) of the AMR signal as shown in Figure 6.1.
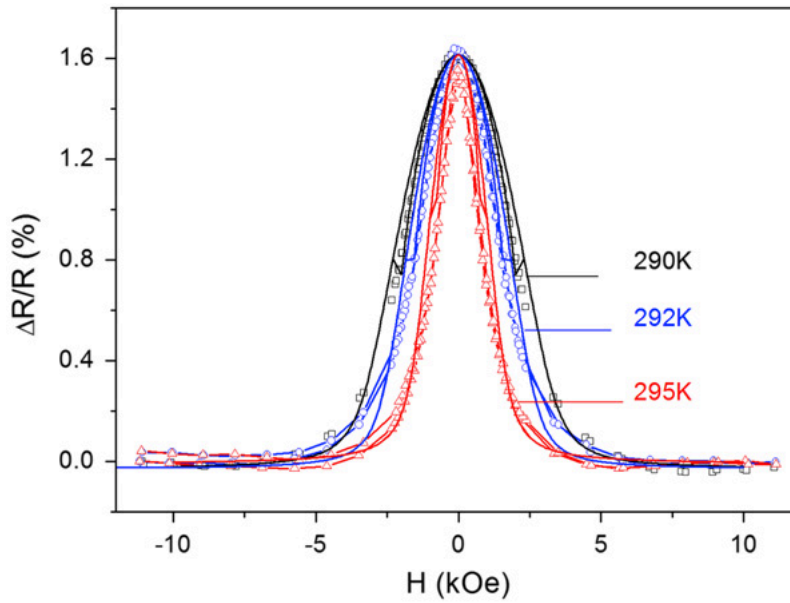
FIGURE 6.1: coercivity variation of the AMR signal in Ni NW embedded in PC matrix under thermo-elastic deformation

The magnetization states of the Ni NW were described by an energetic model proposed in section 4.4. The total ferromagnetic energy in the Ni NW is due to the contribution of the Zeeman coupling, shape anisotropy and magnetoelastic energy. The quasi-static states of the magnetization are defined by the minimum of $E_t(\theta, \varphi)$. This theoretical model is used to fit the experimental data.

The first step is to trace the fit for the AMR reference (at $T_0 = 290K$). Being at room temperature, the effect of the magnetoelastic energy is neglected, and the corresponding energy is due to the contribution of Zeeman coupling and shape anisotropy. Therefore, for $T = T_0$, the minimum $dE/d\theta = 0$ was calculated from equation 4.17. The fit was performed with the following simulation parameters: $\theta_{Happ} = 81°$, $(\Delta R_{max}/R_0) = 1.6$, and the shape anisotropy field fixed at $H_d = 3kOe$. φ_{me} is not taken into account as the set-up is not turned around the NW

axis. The resulting curve, $\Delta R/R_{min}$, is the continuous line in Figure 6.1 at $T_0 = 290K$.

The vectors $\vec{M}$, $\vec{H}$ and $\vec{H}_d$ (aligned with the NW axis) belong to the same plane Π (coplanar configuration). For $\theta_H = 90°$, all the planes Π are equivalent around the NW axis. For $T \neq T_0$, a new term has been taken into account in the energy equation: the magnetoelastic energy related to the magnetoelastic field $\vec{H}_{me}$. The magnetoelastic field is proportional to the stress applied to the Ni NW and it is function of the temperature as described in equation 4.16.

Due to the amorphous structure of the PC film, the stress field around the NW axis is isotropic (section 4.5.2). Therefore, whatever the chosen of Π plane, $\vec{H}_{me}$ will be contained inside of it. Figure 6.2.
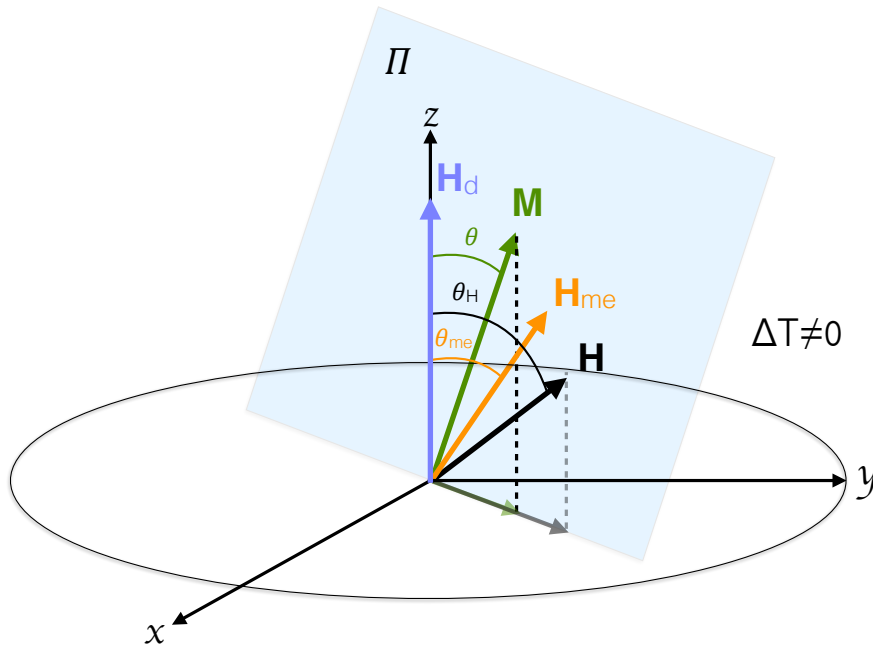
FIGURE 6.2: coplanarity configuration around the Ni NW for $T \neq T_0$: $\vec{H}$, $\vec{M}$, $\vec{H}_d$, and $\vec{H}_{me}$.

Despite the presence of the $\vec{H}_{me}$, when $H = 0$, the vector $\vec{M}$ comes back to the initial state along the NW axis. In fact, as shown in Figure 6.1, for $H = 0$ there is no amplitude variation in the AMR signal. This condition is true only if the $H_d > H_{me}$.

6.2   Response of the magnetization to piezoelectric effect in PVDF

Driven by this first result, the second step was to change the polymer film matrix. The matrix chosen to electrodeposite a single Ni NW was the bi-oriented PVDF film. As already discussed in the chapter 4, bi-oriented PVDF film is considered as a transversely isotropic material with *x-y* isotropic plane. The magnetization states of the Ni NW were investigated applying a DC voltage on the PVDF film in order to induce an elastic deformation by inverse piezoelectric effect. The deformation of the film exerts a stress on the NW inducing a modification in the magnetization states.

Before we go any further, we must verify that we do not underestimate the depolarization of a piezoelectric PVDF thin film by the SHI during bombardment. [28] The fluence chose was 10^9 cm^{-2} in order to avoid the depolarization of the PVDF film. The conservation of the piezoelectric properties under different irradiation sources will be largely illustrated in the chapter 9.

A lithography mask has been designed as shown in Figure 6.3. The mask consists of two interdigitate parts: the first part corresponds with 50 parallel equidistant lines where statistically one single Ni NW may be grown by electrodeposition; the second one (namely the capacitances) surrounded the lines, and it is not in contact with them. The capacitance were used to apply the DC voltage in order to deform the film around the Ni NW. The gap between the lines and the capacitances has to be in the range of 10 μm. Indeed, the stress detected by Ni NW decreases exponentially from the capacitance edges to the contacted NW. Larger gaps would lead to insufficient stress on the NW.
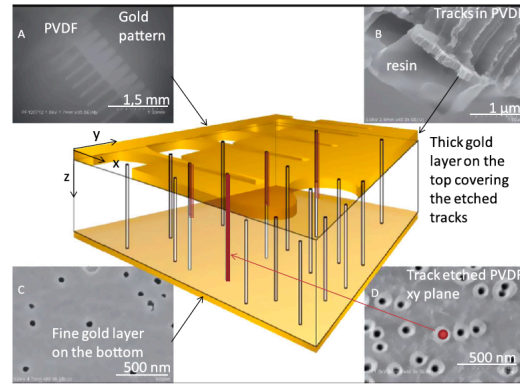
FIGURE 6.3: nanofabrication of the device with a single contacted Ni NW (red) in a track-etched piezoelectric PVDF membrane. The surrounding figures are FESEM images of (A) the gold pattern obtained from lithography with interdigitated lines; (B) a cryofracture of the device exhibiting the photoresist resin layer;(C) the track-etched PVDF surface covered by a 10 nm thick gold layer; (D) the nude track-etched PVDF membrane.

The AMR of the single-contacted NW is measured as a function of the magnetic field without applied voltage (0V) and under applied voltage (30V) Figure 6.4. The resistance measurement of the Ni NW is performed at two wires. The presence of a large contact resistance, in the parallel lines, not allowed to reach high values of AMR (maximum 0.25%). Due to the small signal-to-noise ratio, each curve has been measured by averaging over five hysteresis cycles between -10kOe to 10kOe ($\theta_H = 90°$).
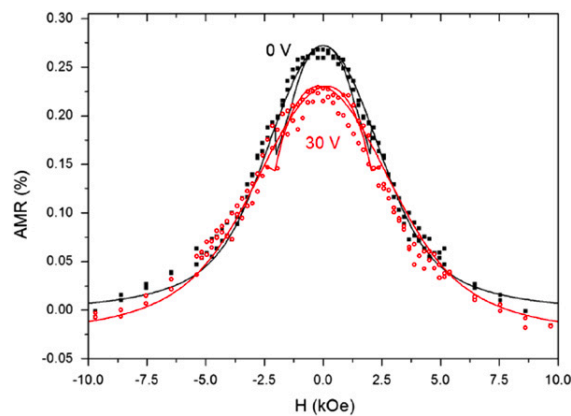
FIGURE 6.4: comparative measurements with piezoelectric voltage (open circles) and without piezoelectric voltage (full squares). The applied magnetic field: $\theta_H = 90°$. Continuous curves represent the fits deduced by the uniform-magnetization model. The amplitude of the stress field is found to be about $H_{me} = 0.1T$ and angle orientation $\theta_{me} = 70°$.

Contrary to the PC system, the effect of the deformation contributes to decrease the amplitute of the AMR signal. Further investigations were made them difficult by high level of noise in the measurement. This unexpected result, represents the starting point of my thesis.

6.3 Thermo-mechanical effects in PVDF

In order to avoid the high level of noise in the AMR measurement, the PVDF film was tested under thermo-eleastic deformation. The advantage of this technique not only reduces the noise in the measurement, but it allows to investigate deeper the role of the PVDF matrix and how it affects the magnetization states of the Ni NW. Figure 6.5 shows the effect of the temperature on the AMR curves. As already predicted in the context of inverse piezoelectric measurement, the amplitude and coercivity variation of the AMR is still confirmed by thermoelastic deformation.
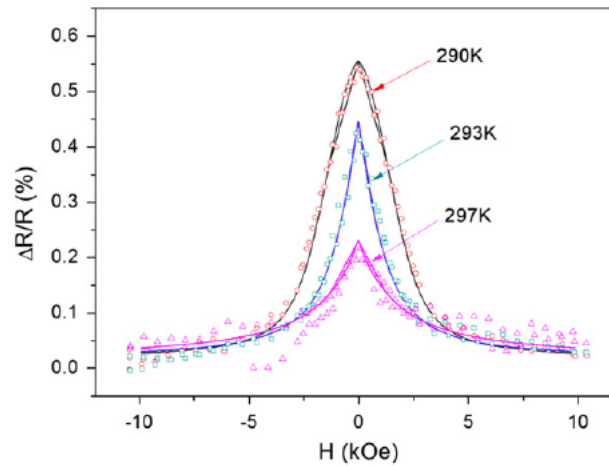
FIGURE 6.5: amplitude variation of the AMR signal in Ni NW embedded in PVDF matrix under thermo-elastic deformation

For $T \neq T_0$, the tremendous variation of the amplitude of the AMR signal indicates that the magnetization can no longer be aligned along the wire axis and keeps a non-zero angle ($\theta \neq 0$) even in the absence of an external magnetic field. It should correspond to a supplementary field contribution out-of-the plane Π defined by the wire axis and the external field. This supplementary field ($\vec{H}_{me}$) breaks the cylindrical symmetry (Figure 6.6) and it is induced by the thermoelastic stress. This effect is related with the anisotropy of the PVDF film (section 4.5.1). The structure of the film results in an anisotropic stress field around the Ni NW with a preferential orientation of the stress in the space.
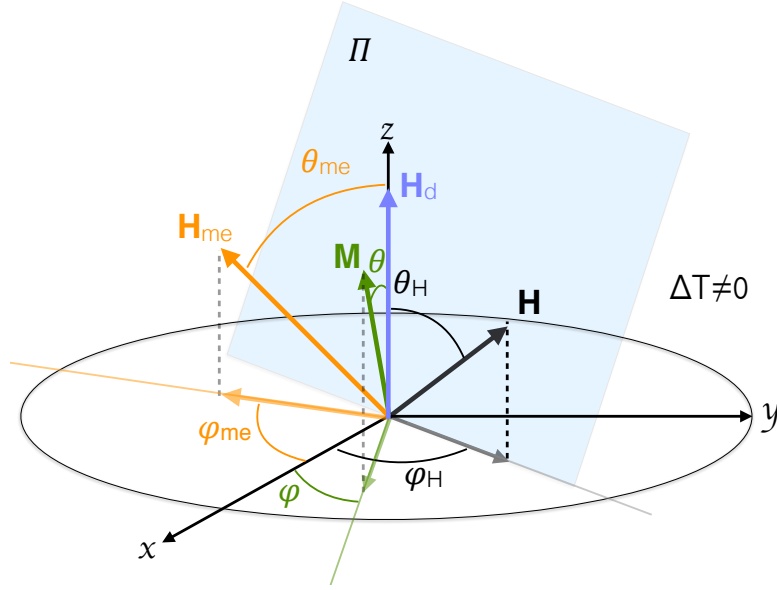
FIGURE 6.6: out-of-plane vectors due to $\vec{H}_{me}$

This hypothesis has been verified by calculation of minimum of the total energy, including the magnetoeleastic term given by equation 4.19. Parameters obtained from the curve fits are summarized in the table of Figure 6.7. A privileged orientation at angle $\theta_{me} = 72° \pm 3$ respect to the Ni NW axis was found. The amplitude of the H_{me} varies linearly with the temperature.

According to linear elastic theory, described in section 4.5.1, σ_{PVDF} can be expressed by $\sigma_{PVDF} = E_{PVDF}.\epsilon$. The young moduli of PVDF are equal to 2.5 and 5.8GPa, respectively in the isotropic plane (*x-y*) and in *z* direction. Considering the thermal expansion of the PVDF, we obtain $(\Delta\sigma_{PVDF}/\Delta T) = \alpha_{PVDF}.E_{PVDF} = 2.5 - 5.8.10^5 Pa.K^{-1}$. The magnetoelastic field given by equation 4.19, becomes:

$$\frac{\Delta H_{me}}{\Delta T} = \frac{3\lambda_{si}}{2M_s}\frac{\Delta\sigma_{Ni}}{\Delta T} \tag{6.1}$$

Where λ_{si} is the magnetostriction coefficient for Ni ($\lambda_{si} \approx -3.10^{-5}$), M_s is the saturation magnetization of Ni ($M_s = 485emu.cm^{-3} = 485.10^3 J.T^{-1}m^{-3}$). From Figure 6.7(a) $(\Delta H_{me}/\Delta T) = 0.05T.K^{-1}$, consequently $(\frac{\Delta\sigma_{Ni}}{\Delta T}) = -5.10^8 Pa.K^{-1}$. This implies that the induced stress field per degree Kelvin in the Ni NW is 1000 times higher than the initial stress field.

We assume that lattice displacements at the interfaces are continuous, that corresponds with the condition of isostrain at the interface metal-polymer ($\epsilon_{Ni} = \epsilon_{PVDF}$). The increase of stress at the interface should mainly be due to differences in the Young's moduli. The tensile strength of bulk Ni is 230 GPa which is two orders of magnitude higher than in PVDF and PC. The resulting variation of the strain per degree Kelvin of a Ni NW is roughly $2.10^{-3}.K^{-1}$.

External heat (K)	θme (Deg)	Hme (T)
291	74	0,05
292	74	0,15
293	73	0,20
295	75	0,25
297	70	0,38

(a)   (b)
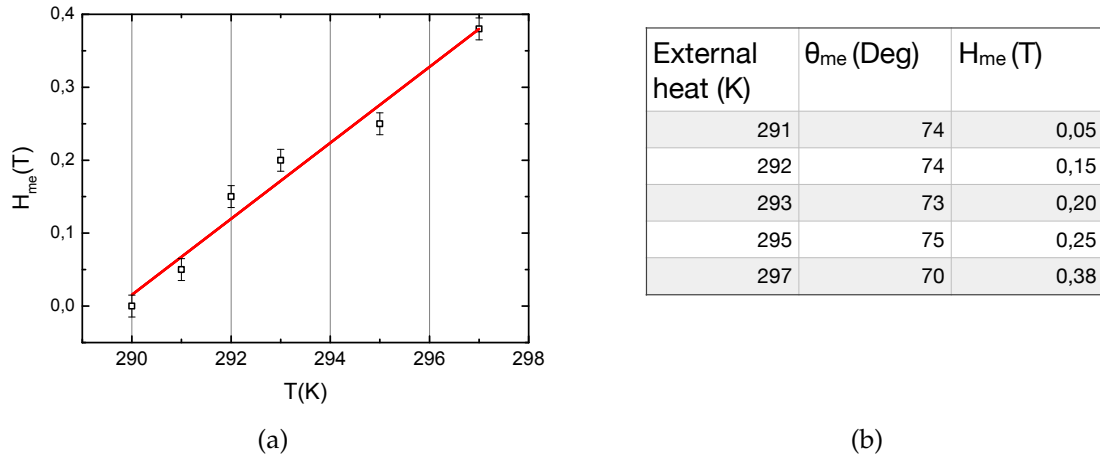
FIGURE 6.7: (a). Magnetoelastic field induced by the external stress on the Ni NW as a function of the temperature. The linear fit yields a slope of about $0.05 T.K^{-1}$; (b). Paramaters at various temperatures for the AMR fit. H_{me} is deduced from the equation 4.19

In comparison to research work on similar system constitutes by arrays of Ni NWs [60, 61], the strain found here is still larger by a factor 5-10. The possible explanation is that only few contacted NWs are measured such that the magnetoelactic anisotropy energy becomes very high enhancing the resulting stress.

To explain the obtained value of high strain in the Ni NW, we have recalculated the Young modulus of a Ni NW (9 μm length, 75 nm in diameter) as shown in section 4.5.3. The apparent elastic modulus calculated from equation 4.30 is 745 GPa. The resulting variation of the strain per degree Kelvin of the Ni NW is thus lowered to $6.10^{-4} K^{-1}$. We passed from $2.10^{-3}.K^{-1}$ to $6.10^{-4}.K^{-1}$, which shown the importance of taking into account the nano-object size in the calculations.

6.4 Angle dependence on the AMR amplitude of a single-contacted Ni nanowire

In the previous section a privileged angle, $\theta_{me} = 70°$, between the NW axis and H_{me} was found. In order to prove the validity of the calculation, we tilt the NW axis to come closer to this value. The goal is to investigate the orientation effect on the magnetoelastic field, under thermomechanical strain due to the dilatation of the surrounded polymer matrix. α_{irr} indicates the irradiation angle. 0°, 15°, and 45° are tested (Figure 6.8)
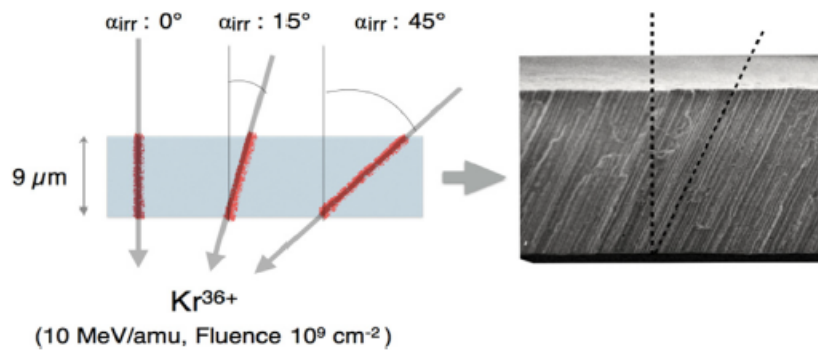
FIGURE 6.8: left: angle investigation: different angles have been tested: $0°$, $15°$ and $45°$. Irradiation under He atmosphere; right: membrane section (FE-SEM image).

Figure 6.9 displays curves where all the AMR amplitudes are plotted versus the angle of the Ni NW respect to the normal of the PVDF film surface. The phase shifts correspond accurately to the angles defined experimentally.
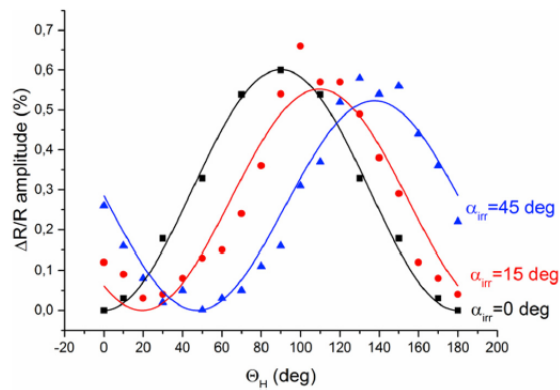
FIGURE 6.9: AMR amplitude versus the angle between the external field and the Ni NW axis hH at different Ni NW orientations (α_{irr} =0°, 15° and 45°) from the initial track etched PVDF membrane surface.

As described in the latter section, for a given $\Delta T \neq 0$ a not-in-plane magnetoelastic field is introduced ($\vec{H}_{me}$) in the PVDF.

$\vec{H}_{me}$ has two components perpendicular and parallel with respect to the wire axis (Figure 6.6). When the wire axis is tilted, $\vec{H}_{me}$ tends to align to $\vec{H}_d$ (along the NW axis) affecting the contribution of both components. These results demonstrate that when $\vec{H}_{me}$ is aligned to the wire axis, the co-planarity between $\vec{M}$, $\vec{H}$, $\vec{H}_{me}$, and $\vec{H}_d$ is recovered. The angle variation of the Ni NWs in respect with PVDF film surface (from $0°$ to $45°$) exhibits an exponential decay of the AMR amplitude variation. It means that the rotation of the system tends to diminish severely the anisotropic stress amplitude experienced by the Ni NW (Figure 6.10)
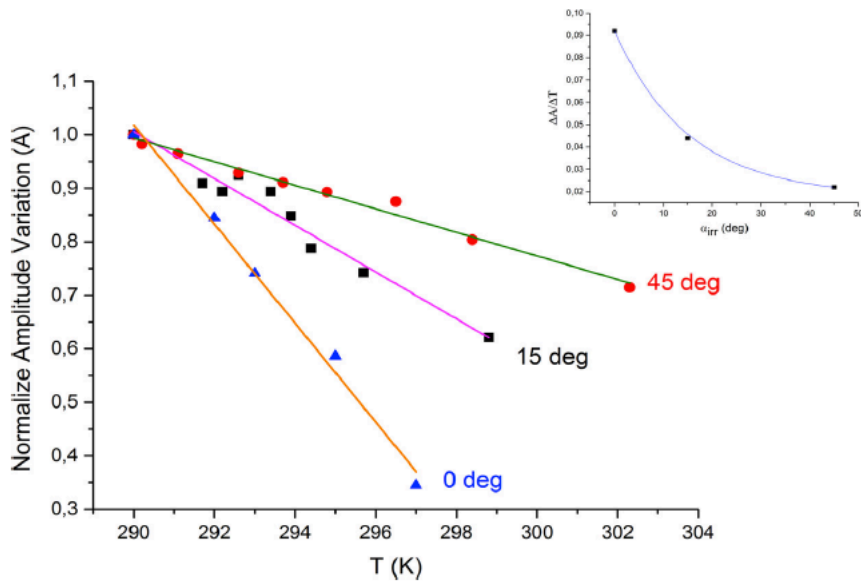
FIGURE 6.10: Normalized amplitude variation (A) versus the temperature T. *inset:* apparent Apparent exponential law linking $\Delta A / \Delta T$ to α_{irr}.

The AMR characterization has herein been confirmed by a study in rotating the Ni NW inside the PVDF matrix.

6.5 Conclusion

AMR has demonstrated to be a very sensitive technique to identify the physical constrains exerted on a single Ni NW. The analysis of the single Ni NW embedded in PC matrix shows a coercivity (width) decrease of the AMR signal with the temperature. The magnetization states of the Ni NW are described by the total ferromagnetic energy given by Zeeman coupling and anisotropic energy contributions. Finding the minimum of the total ferromagnetic energy ($dE/d\theta = 0$)

we are able to fit the AMR curves at room temperature (T_0). All the planes Π, containing $\vec{H}$ (fixed $\theta_H = 90°$ respect to the NW axis) $\vec{M}$ and $\vec{H}_d$, are equivalent around the NW axis (cylindrical symmetry). For $T \neq T_0$, a new term has been taken into account in the total energy expression: the magnetoelastic energy related with a magnetoelastic field ($\vec{H}_{me}$). The presence of $\vec{H}_{me}$ (proportional to the stress applied on the Ni NW) affects the coercivity of the AMR signal. Due to the amorphous structure of the PC matrix film, the resulting stress field around the Ni NW is isotropic. Therefore, $\vec{H}_{me}$ is also contained in the plane defined by $\vec{H}$, $\vec{M}$ and $\vec{H}_d$. The interaction PVDF film/Ni NW was investigated by (i) inverse piezoelectric effect and (ii) thermo-elastic deformation.

(i) An interdigitate gold mask was applied on the PVDF film. Exploiting the inverse piezoelectric effect of the PVDF, a resulting stress is transferred to the Ni NW. Contrary to the PC, the main effect on the AMR curves, is related to the decrease of the amplitute and coercivity of the signal. In an experimental point of view, the high level of noise (induced by the DC voltage), made the measurements difficult to achieve.

(ii) An alternative was represented by the thermo-elastic deformation of the PVDF. The decrease of the AMR amplitude was still confirmed for $T \neq T_0$. The presence of anisotropic stress field, around the Ni NW due to the bi-oriented PVDF film, generates a resulting stress with a particular direction in the 3-D space. As a consequence the $\vec{H}_{me}$ comes out of the plane Π breaking the cylindrical symmetry. In these conditions, The magnetization can no longer be aligned along the wire axis and keeps a non-zero angle ($\theta \neq 0$) even in the absence of an external magnetic field. The angle between the NW axis and the $\vec{H}_{me}$ is named θ_{me} and it was found around $73°$.

The latter result has been confirmed by rotating the NW axis in order to come closer to previous value of θ_{me}. AMR profiles as a function of the set-up angles (θ_H) show a perfect match with expected angles from irradiation. It has also been found that the maximum variation of the AMR with and without stress is linear for a given configuration. Such a behavior shows that there is a proportional and quantitative relationship between the stress and the AMR amplitude variation. When the wire axis is tilted, $\vec{H}_{me}$ tends to align to $\vec{H}_d$ (along the NW axis) affecting the contribution of both components. These results demonstrate that when $\vec{H}_{me}$ is aligned to the wire axis, the co-planarity between $\vec{M}$, $\vec{H}$, $\vec{H}_{me}$, and $\vec{H}_d$ is almost recovered.

Part III

Chapter 7

Materials and methods

The present chapter reports the irradiation conditions for poled β-PVDF film. In our study, we consider an irradiated and nanostructured PVDF films: in the first case, the samples were irradiated and the piezoelectric response directly analyzed; the nanostructuration of the PVDF films, instead, involves different preparation steps before the piezoelectric response measurement (7.2). A homemade device was realized to measure the output voltage as a function of the bending deformation for irradiated and nanostructured PVDF film (7.3). The electrical efficiency was measured to evaluate the effects of the irradiations and nanostructuration in PVDF film. (7.5)

7.1   SHI and e-beam irradiation

In this section, SHI and e-beam irradiations are presented. In particular, e-beam and SHI irradiations are performed to change the structure of the polymer (introducing defects). The piezoelectric response is then analyzed. Parts of the irradiated samples are used for the nanostructuration.

Electron irradiations were performed at SIRIUS facility (Laboratoire des Solides irradiés, France). Films were irradiated at room temperature under He atmosphere, with an accelerating voltage of 2.5 MeV and a machine current of 1.4 μA. The investigated doses were 5, 10, 25, 50, 100 kGy with a dose rate of 125 kGy.h^{-1}. The samples were irradiated step by step using a movable sample holder (speed rate 0.109 m.min^{-1}). The number of passages in front of the beam is calculated as a function of the final dose and the dose rate. All irradiated samples were stored at -20°Cunder N$_2$ atmosphere.

SHI are performed as described in section 5.2. In order to compare the effect of e-beam and SHI irradiation, the fluencies used during SHI irradiation are converted into adsorbed doses. The conversion equation has been introduced in section 3.1.1. According with the equation 3.3, fluencies 10^7, 10^8, and 10^9 have been estimated to correspond, under our experimental conditions, at 0.076 kGy,

0.76 kGy and 7.6 kGy respectively.

In order to ensure an electric contact during the piezoelectric measurement, gold layers were sputtered on both sides of the film with thickness corresponding to 100 nm. The dimension of the mask used to sputter gold was 3.5×1.5cm. The surfaces were not entirely covered with gold, but 2 mm non-covered edges were designed in order to avoid short-circuit between top and bottom side of the film. At this point, The samples are ready to be tested.

PVDF films, irradiated with SHI (fluence $5.10^8.cm^{-2}$), are instead used as base for the nanostructuration.

7.2   Nanostructuration steps

The nanostructuration steps described in this section, in principle, are the same used for the single-contacted Ni NW investigated in the last chapter. In particular, SHI and chemical etching are exactly the same, except for the etching time. In fact, different etching times were investigated: 20, 30, 40, 50, and 60 minutes.

Electrodeposition technique and electrolyte solution remain unchanged (potentiostat mode - electrolyte solution: 65g $NiSO_4$ and 15g H_3BO_3 in 500ml of water). A rectangular mask of 3.5×1.5cm was used to sputter 200nm of gold in one side of the PVDF film (Note that the thickness of the gold layer is 100 nm thicker respect to the previous case in section 7.1). The other side of the film is not covered with gold. Therefore, during the electrodeposition, there is no control on the growth of the Ni NWs inside the nanopores, it means that many NWs could reach the surface of the PVDF without any electrodeposition current peak, contrarily to the case shown in section 5.4.2. Three different electrodeposition times were chosen: 50, 100 and 150 seconds. Electrodeposition time higher than 150 seconds may provide a spread diffusion of the electrodeposited Ni on the surface of the PVDF film. It is important to avoid this phenomenon in order to reduce the eventual short circuit problem (between top and bottom electrode gold layers) during the piezoelectric measurement.

The sample is prepared as shown in Figure 7.1(a). The sputtered gold layer on the bottom of the PVDF film is in contact with the metallic support (dimension: 6.5×3cm) by silver paint. The sample is then sealed by Kapton tape in order to avoid the reduction of the electrolyte directly on the metallic support. The other side of the PVDF film (without gold layer) is exposed to the electrolyte. Therefore, the metallic support is connected with the potentiostat. The electrodeposition proceeds in the same conditions described in section 5.4.2.
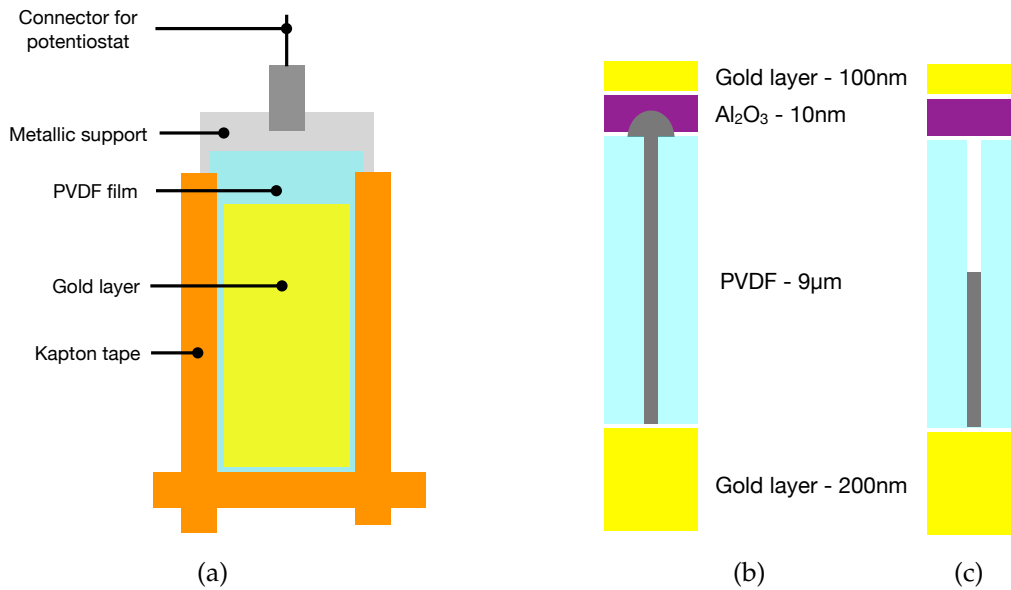
FIGURE 7.1: (a). Preparation sample for electrodeposition; (b). Cross-section of the PVDF film with electrodeposited Ni NW and multi-layer Al_2O_3/Au on the top; (c) intermediate electrodeposition time.

After electrodeposition, it needs a second electrode on top of the PVDF film to measure the piezoelectric response. Moreover, even if we consider 50 seconds as electrodeposition time, statistically, the probability of one NW to reach the surface of the film is not null. Covering directly the surface with a gold layer, the risk is to short-circuit the top and bottom gold layer, making ineffective the piezoelectric measurement. Therefore, to prevent a short-circuit, a layer of Al_2O_3 is deposited by Atomic Layer Deposition (ALD) on top of the PVDF surface. The thickness chose for Al_2O_3 is around 10nm. In fact, thicker Al_2O_3 layer improves the insulation but it reduces the flexibility of the polymer and the piezoelectric response. Instead, a thinner layer doesn't ensure the electrical insulation between gold layer and Ni NWs. Thus, independently of the electrodeposition time, all the samples used in this study were covered by Al_2O_3 layer. In the final step, a gold layer of 100nm is sputtered on the surface of the samples, and the Al_2O_3 is completely covered. Figure 7.1(b) and Figure 7.1(c) shown the cross-section of the PVDF film with electrodeposited Ni NW and the multi-layer Al_2O_3/Au on the top.

7.3 Experimental set-up

An experimental set-up was designed to measure the direct piezoelectric effect in view of energy harvesting objectives. It consists of two symmetrical parts

of PMMA housing with a pressure chamber (Figure 7.2). The PVDF film was sandwiched against two parts of the device in contact with the pressure chamber. Metallic spheres, incorporated inside the cell housing, contact each gold coatings. The sensing area is 0.785 cm2.
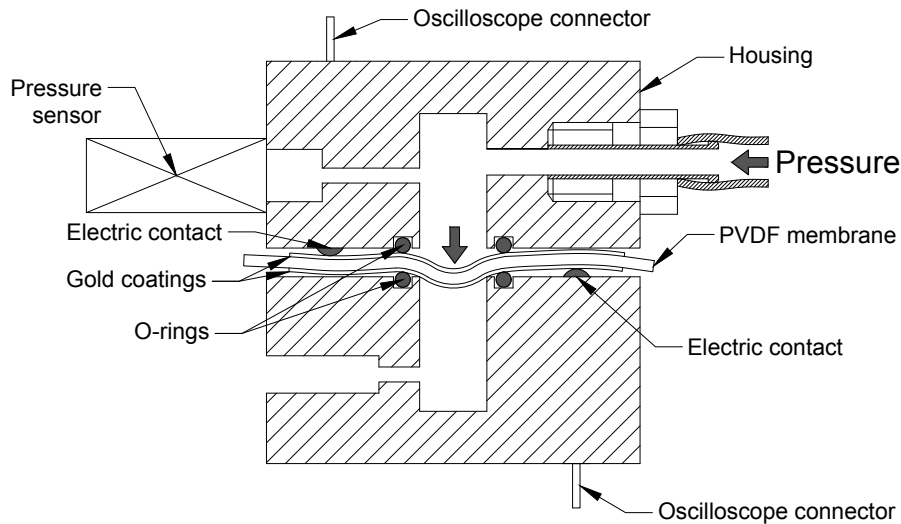
FIGURE 7.2: section of the pressure cell. Pressure chamber in contact with the PVDF film.

The air arrival pressure was set by a 3-ways solenoid-valve *SMC VDW250*. The current was supplied by *ISO-TECH DC power supply IPS 303DD*. The pressure signal is a periodic square-wave, where the frequency and width are fixed by *KEITHLEY 3390 waveform generator*. The pressure value is fixed directly by the compressed air cylinder (between 0.08 and 0.7Bar; note that the pressure is expressed in terms of relative pressure). The pressure variation inside cell was measured by pressure detector *GEMS pressure sensor* (output 0-5V; range 0-2.5bar). The pressure variation and the output voltage from the film deformation is registered by oscilloscope *PicoScope 4000 series* (input impedance = 1MΩ). The waveform generator and the oscilloscope were managed by computer using *matlab* Figure 7.3.
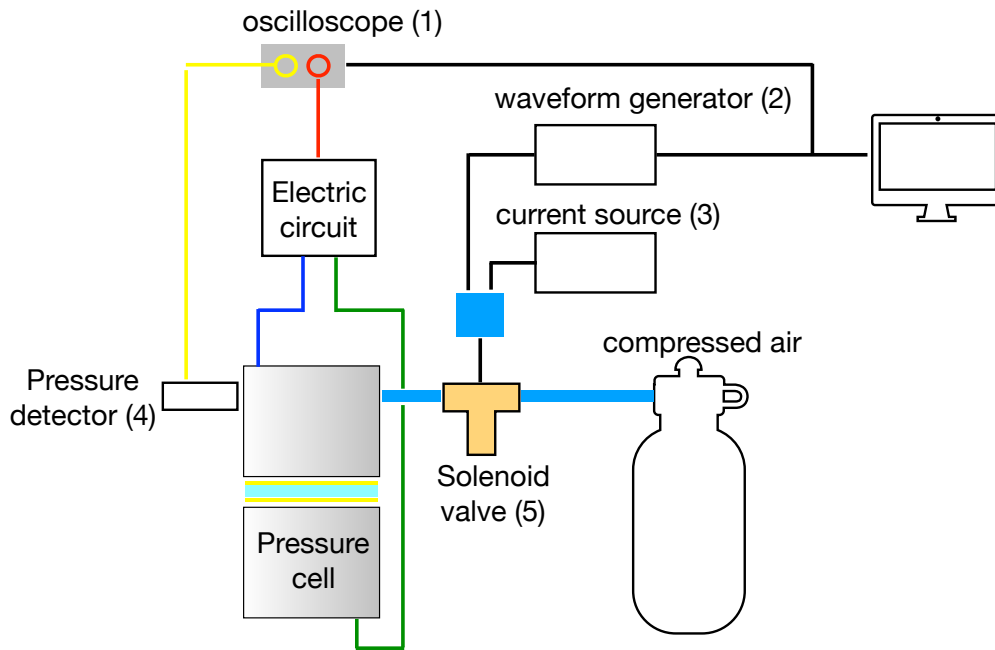
FIGURE 7.3: experimental set-up. (1) - PicoScope 4000 series; (2) - KEITHLEY 3390 waveform generator; (3) - ISO-TECH DC power supply IPS 303DD; (4) - GEMS pressure sensor; (5) - Solenoid valve SMC VDW250.

The PVDF film is connected to the electrical circuit in order to measure the output voltage. It consists of two resistances in series: R_1 and R_2 (Figure 7.4). R_2 is fixed at 1MΩ and it is in parallel with the impedance of the oscilloscope. This configuration allows to increase the resistance at values higher than 1MΩ. In fact, if we consider R_2 as the only resistance, The electrical measurement would be limited by the oscilloscope impedance.
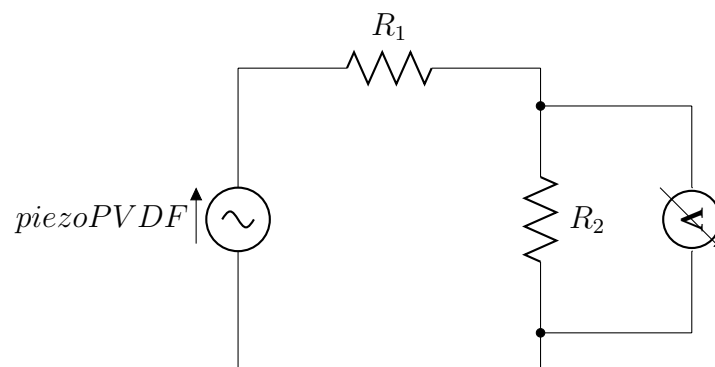
FIGURE 7.4: electric circuit used to measure the output voltage from the Piezo-PVDF film under bending stress condition

7.4   Output voltage function applied pressure

Fixing the output pressure from the compressed air cylinder, chronological events were registered starting from the opening to the closure of the solenoid-valve. When the solenoid-valve is open, the pressure suddenly increases inside the chamber. The pressure bends the film and the instantaneous electrical response takes the form of a positive (or negative, according with the poling direction) output voltage peak as seen in Figure 7.5. The change of pressure reaches its maximum and the electrical signal falls down to zero. The system is driven by a 3-ways solenoid-valve. The closure of the solenoid-valve results in an air depression, corresponding to a negative (or positive) output voltage peak.
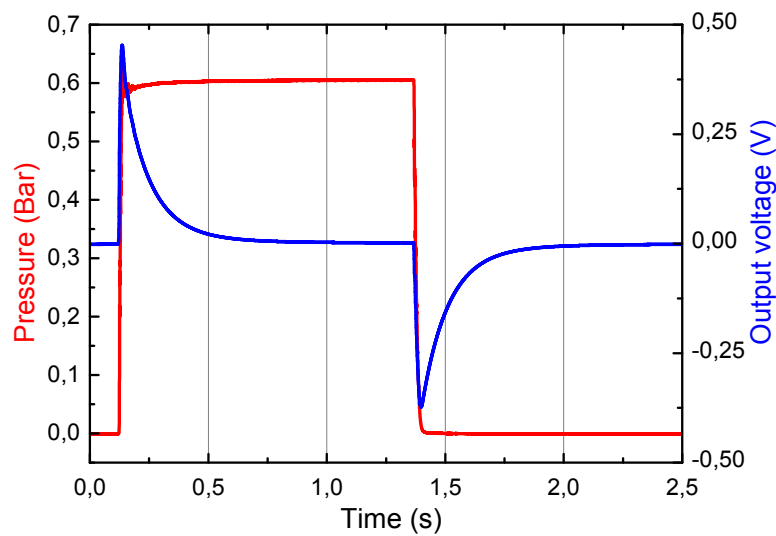
FIGURE 7.5: output voltage under cycling bending stress condition.
Frquency=0.4Hz; width=1.25s; ΔP=0.6bar; R_1=20MΩ

The output voltage is obtained considering the electric circuit in Figure 7.4, with R_1=20MΩ and R_2=1MΩ. The ΔP was fixed at 0.6bar, and the load pressure was applied with a frequency equal to 0.4Hz and width=1.25s.
The output voltage was measured for different ΔP: 0.082, 0.19, 0.29, 0.38, 0.5, 0.61 and 0.7 bar. The negative (or positive) output voltage peak is plotted function of the applied ΔP. Figure 7.6 shown the typical variation of the output voltage peak function of applied ΔP. The standard error, calculated for each point of the curve, is less than 0.2%.
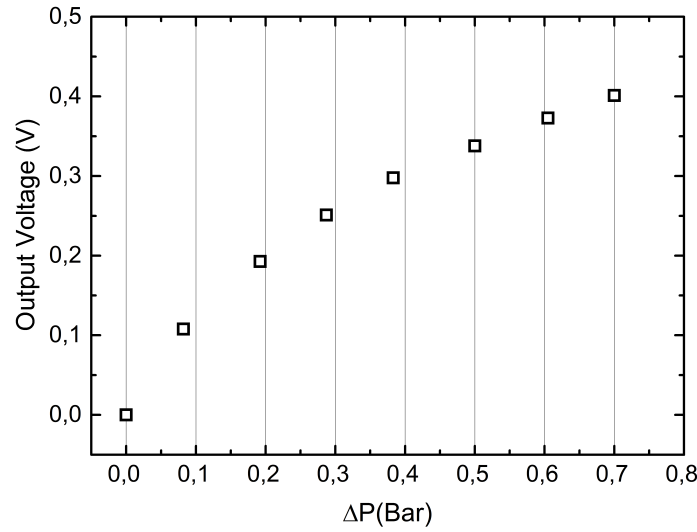
FIGURE 7.6: Output voltage *vs* applied ΔP

7.5 Electrical efficiency

The energy conversion efficiency can be estimated as the ratio between the total electrical energy (W_e) and the total mechanical energy (W_m) transferred onto the membrane during a bending and releasing cycle.

$$\eta = \frac{W_e}{W_m} \tag{7.1}$$

W_e is calculated as:

$$W_e = R_{tot} \int \left(\frac{U(t)}{R_\parallel}\right)^2 dt \tag{7.2}$$

Where U(t) is output voltage measure across $R_\parallel$; $R_\parallel$ is the equivalent resistance between the oscilloscope impedance (R_{osc}) and R_2:

$$R_\parallel = \frac{R_{osc}R_2}{R_{osc} + R_2} \tag{7.3}$$

R_{tot} is the total equivalent resistance:

$$R_{tot} = \left(\frac{R_{osc}R_2}{R_{osc} + R_2} + R_1\right) \tag{7.4}$$

The mechanical energy W_m is given by the total energy transfered to the PVDF film.

$$W_m = \frac{1}{T} \int P(t)V dt \tag{7.5}$$

P is the registered pressure in the pressure chamber function of the time, T is the duration of one cycle, and V is the volume of the tested film $5.8.10^{-10}.m^3$.

Chapter 8

Characterizations

In this chapter, we report the main techniques used to characterized the piezoelectric PVDF. The goal is to detect the structural changes after irradiation or nanostructuration steps. Fourier Transform Infrared Spectroscopy (FT-IR) and X-ray diffraction techniques allow to detect the different phases present in the PVDF (α, β, γ) (sections 8.1 and 8.2). Differential scanning calorimetry (DSC) consists in a thermic analysis of the polymer and, in particular, it focuses on the melting peaks of the crystalline phases (section 8.3). Field Emission Scanning Electron Microscopy (FESEM) is used to evaluate the size of the nanopores after chemical etching (section 8.4). Ellipsometry technique gives complementary information respect to the FT-IR (8.5). Dielectric measurements and elastic modulus are investigated to have further information about the electric and mechanical properties respectively (sections 8.6 and 8.7).

8.1 Fourier-transform infrared spectroscopy (FT-IR)

FTIR spectra of the polymer films were measured by a Nicolet IS50 spectrometer equipped with a DTGS detector. The sample compartment is continuously purged by a nitrogen flux. In order to improve the quality of the spectra in transmission mode, measurements were recorded positioning the samples at the Brewster's angle to eliminate interference fringes. The background acquisition was performed before each sample acquisition. Spectra were collected by cumulating 32 scans at a resolution of 2 cm^{-1}.

FTIR spectroscopy allows an accurate discrimination between α, β and γ crystalline phases. All FTIR bands related to α, β and γ are well attributed in the literature (Table 8.1). δ phase is more difficult to ascertain, as this phase is a polarized version of α phase, obtained when submitting an α-PVDF to a high electric field of about 250 MV.m^{-1} [62]. The pristine PVDF spectrum is constituted of the superimposition of the doublets of two kinds of CH_2 groups: those located in the crystalline zones (intense and narrow bands) and those located in the amorphous

zones (small and broad bands).

TABLE 8.1: crystal phases and their IR bands. Vibration modes: B=bending, W=Wagging, R=Rocking, AS=Asymmetric stretching, SS=Symmetric stretching, T=Twisting, S=Scissoring

Phase	Band (cm^{-1})	Vibration modes	Ref.
β	510	B (CF$_2$)	[63–65]
α	532	B (CF$_2$)	[49, 63, 66–69]
α	615	B (CF$_2$), B (CCC),W (CF$_2$)	[49, 64, 65]
α	766	B (CF$_2$), W (CF$_2$)	[49, 64, 66]
α	795	R (CH$_2$)	[49, 63, 66, 67, 69]
β	840	R (CH$_2$), AS (CF$_2$)	[49, 64, 65]
γ	882	SS (CC), SS (CF$_2$)	[63, 66]
α	976	T (CH$_2$)	[49, 63, 66, 67, 69]
β	1074	AS (CC), W (CF$_2$), W (CH$_2$)	[49, 64, 66]
α	1182	SS (CF$_2$), T (CH$_2$)	[64]
β	1286	SS (CF$_2$), SS (CC), B (CCC)	[64, 66, 70]
β	1431	B (CH$_2$)	[49, 64]

Between 1000 and 400 cm^{-1} wavenumber range, which corresponds to the polymer skeletal bending region, we have chosen absorption bands at 615 cm^{-1} and 840 cm^{-1} as signature of α-phase and β-phase respectively (Figure 8.1). Our initial polarized β-PVDF is mainly composed of β-phase and, to a lesser extent, of α-phase. The fraction of β-phase present in each sample can be easily calculated as follow:

$$F(\beta) = \frac{A_\beta}{1.26A_\alpha + A_\beta} \tag{8.1}$$

where A_α and A_β correspond to absorption bands at 760 cm^{-1} and 840 cm^{-1} for α and β phases, respectively. [59]
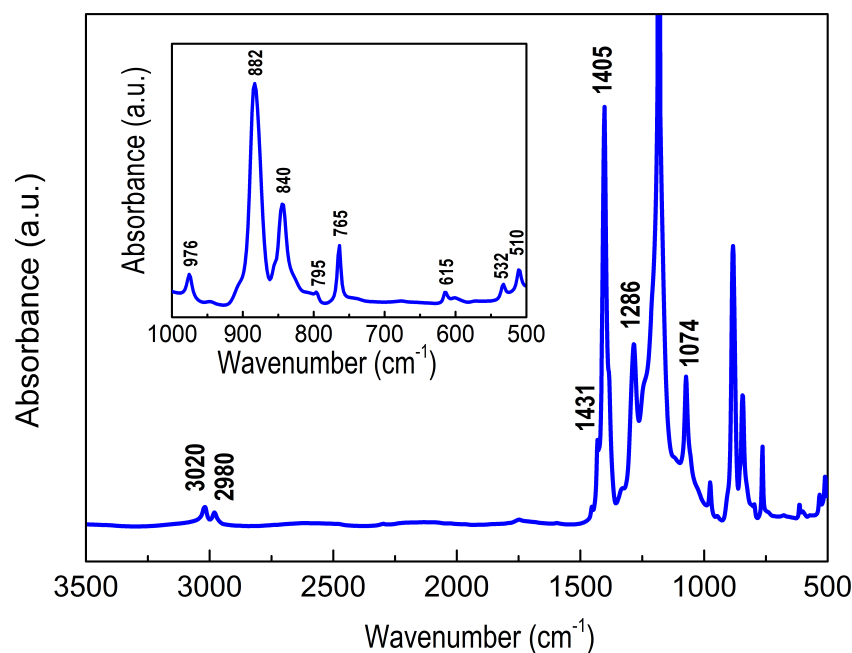
FIGURE 8.1: typical FT-IR spectrum of a neat PVDF film

8.2 X-Ray Diffraction (XRD)

We analyzed the bi-oriented PVDF films with the *X'Pert PANalytical Bragg-Brentano* diffractometer equipped with a linear detector (Ni filter) in the following conditions: from 14 to 70° in 2θ, step 0.02rad, 200 sec/step for a total time acquisition of 1h16. Wavelength type: Kα_1 (λ = 1.540598 monochromatic). The sample was placed on a glass plate (previously coated with a very thin film of grease to improve the adhesion). The amorphous contribution of the glass is subtracted to the final PVDF spectrum. The α and β peaks are tabulated in Diffraction Standards (JCPDS) by the International Centre for Diffraction Data (ICDD). In particular, 42-1650 and 42-1649 JCPDS have been chose respectively for beta and alpha peaks. The main peaks are presented in Table 8.2 We focus on the α and β phases, other phases such as γ and δ are negligible for this study because hardly accessible. In fact, in order to obtain γ phase needs high temperatures and very slow cooling rates from the melting state. [71] δ phase is obtained at high electric field (170 - 250 $MV.m^{-1}$) and it hasn't been carried out in our PVDF film.

TABLE 8.2: main XRD peaks located between 14 and 30°

	h	**k**	**l**	**d[Å]**	2 Theta [degree]	I[%]
	1	0	0	4.96	17.87	34.0
α	0	2	0	4.82	18.39	41
	1	1	0	4.41	20.12	100
β	2	0	0	4.29	20.69	100
	1	1	0	4.26	20.83	100

The more intense peaks are localized between 14° and 30°. For the bi-oriented PVDF film, the typical spectrum is presented in Figure 8.2. The fit was calculated using the α peak at 20.119° (020), and the two β peaks at 20.688° (200) and 20.828° (110). A broad peak is introduced to take into account the amorphous part of the polymer. During the fit, the position of peaks is fixed. The peak functions used are *pseudo-voigt* ones.
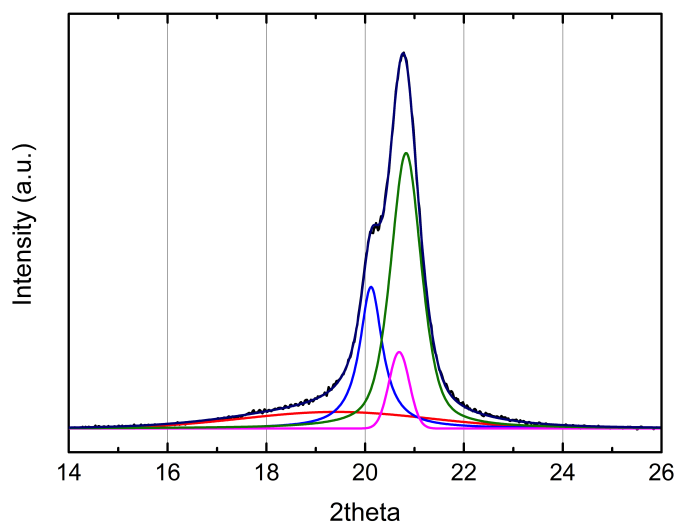
FIGURE 8.2: typical XRD spectrum for bi-oriented neat PVDF. Blue, magenta, green and red lines represent respectively: α (2θ=20.119), β (2θ=20.688), β (2θ=20.828) and the broad peak.

8.3 Differential Scanning Calorimetry (DSC)

The heat of fusion and melting temperature were measured by Perkin–Elmer Differential Scanning Calorimeter (DSC-7) at heating rate of 20°C.min^{-1}. The second run (after the first melting and recrystallization steps) has been analyzed.

Figure 8.3 shows the typical melting peak for neat PVDF. The degree of crystallinity was calculated using the relationship:

$$X_c(\%) = \frac{H_f}{H_{f0}}.100 \tag{8.2}$$

where H_f is the heat of fusion of the tested sample, and H_{f0}=104.7 J.g^{-1} is the heat of fusion of 100% crystalline α-PVDF. The melting peak was measured around 167°C. The corresponding degree of cristallinity was calculated around 36%.
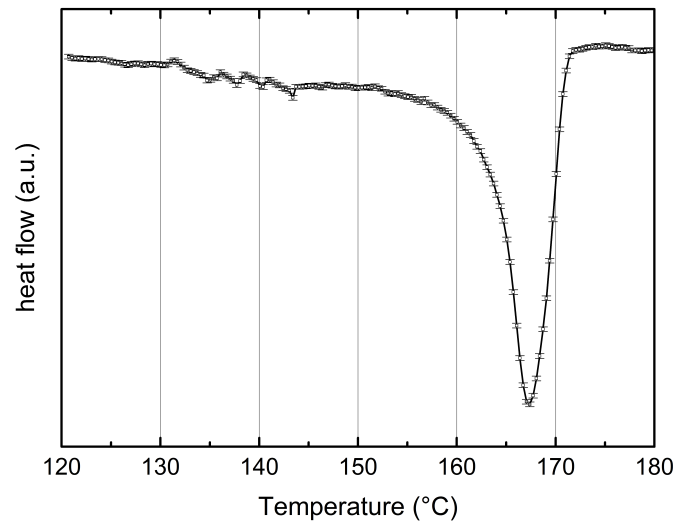
FIGURE 8.3: DSC melting peak of neat PVDF.

8.4 Field Emission Scanning Electron Microscopy (FE-SEM)

FESEM (*HITACHI S-4800*) was used to analyze the polymeric surface after chemical etching. The interaction of the electrons with the polymer surface generates an accumulation of charges making difficult to investigate the nano-pores size. For this reason, it is recommended to sputter a thin gold layer (15nm) on top of the film before performing the measurement of the diameter. The sample is sticked (with a conductive carbon tape) in an specific sample holder. Therefore, the sample holder was inserted in the microscope with a working distance of 20mm. The accelerating voltage and current were around 1kV and 10μA, respectively.
Figure 8.4(a) shows the surface of the PVDF after chemical etching. Due to the presence of adjacent latent tracks, the overlapping between two pores statistically occur. Cryofractures of the film were investigated in order to verify the complete

opening of the pores after etching. In particular, the PVDF film is immersed in liquid nitrogen (temperature lower than the PVDF glass transition around -35°C) for 5 minutes, afterwards it is broken in two pieces. The sharp fracture allows to maintain the structure of the nano-pores (Figure 8.4(b)).

(a)   (b)
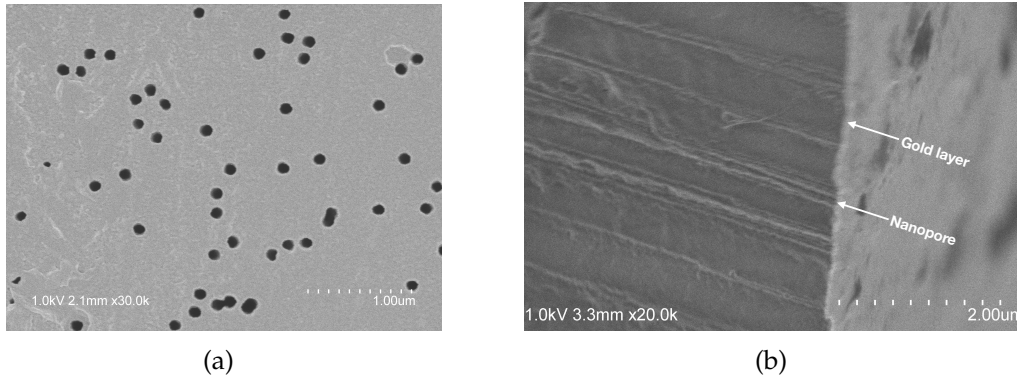
FIGURE 8.4: (a). FESEM image of the PVDF surface after chemical etching (fluence $5.10^8 . cm^{-2}$); (b). Cross-section of the PVDF .

Cryofracture of films track-etched with different angles $15°$, $30°$ and $45°$ were investigated. The irradiation angle is maintained after chemical etching as shown in Figure 8.5(b).

(a)   (b)
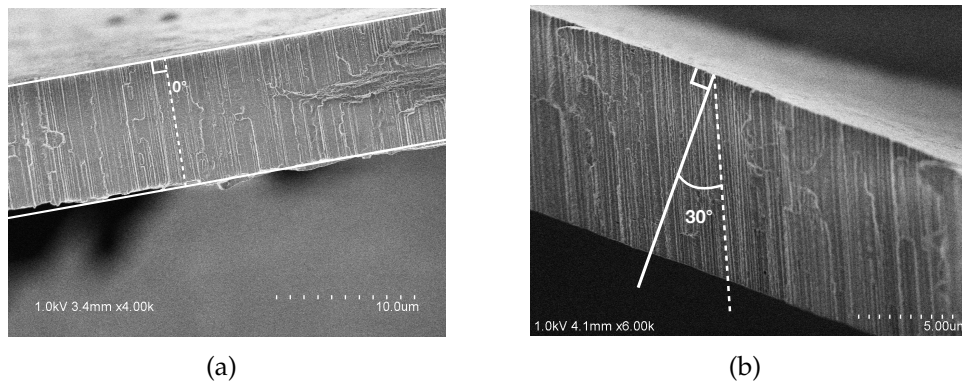
FIGURE 8.5: Cross section of track-etched PVDF. Nanopores perpendicular to the surface (a), and at $30°$ respect to perpendicular axis at the surface (b).

Figure 8.6 shows the linear variation of the PVDF nanopores radii function of the etching time. [72]
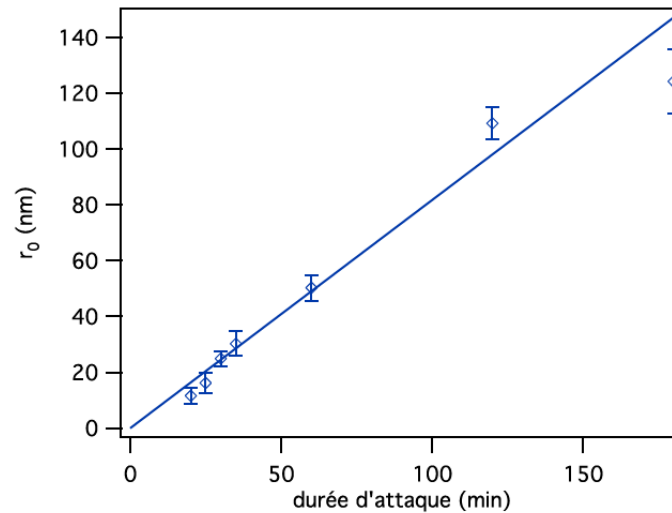
FIGURE 8.6: average radius *versus* etching time. Irradiation fluence $5.10^8.cm^{-2}$. Equation fit: $r_0 = (0.82 \pm 0.05)t$. [72]

8.5 Infrared spectroscopic ellipsometry

A Mueller ellipsometer is an optical instrument that measures the Mueller matrix of the studied sample. The Mueller matrix is a 4×4 matrix that describes how the polarization of an incident beam is transformed by the sample after being transmitted. A scheme of the IR Mueller ellipsometer is presented in Figure 8.7. The Mueller ellipsometer consists of two optical arms, with the sample placed between them. The entry arm includes an illumination source and a polarization state generator (PSG). The exit arm comprises the polarization state analyzer (PSA) and the detector. We used a commercial (iS10 by Thermo Fisher Scientific) Fourier transform infrared (FTIR) spectrometer equipped with a thermal Globar source for illumination, and a nitrogen-cooled IR detector. The PSG consists of a holographic grid linear polarizer (by Specac) followed by a double Fresnel rhomb (by M. Delfour). The double Fresnel rhomb provides a quasi-achromatic retardation within the measured spectral range. The different polarization states are generated by rotating the double Fresnel rhomb about an axis perpendicular to the polarizer surface. The angle between the double Fresnel rhomb and the grid polarizer determines the polarization state. The PSA also consists of a double Fresnel rhomb and a holographic wire grid linear polarizer. The PSA generates different analysis configurations by rotating the double Fresnel rhomb about an axis perpendicular to the surface of the polarizer (optical axis). In order to measure a Mueller matrix, the instrument needs to perform a minimum of 16 independent measurements. To do so, the instrument generates four consecutive polarization states and analyzes each state with four consecutive analysis configurations.
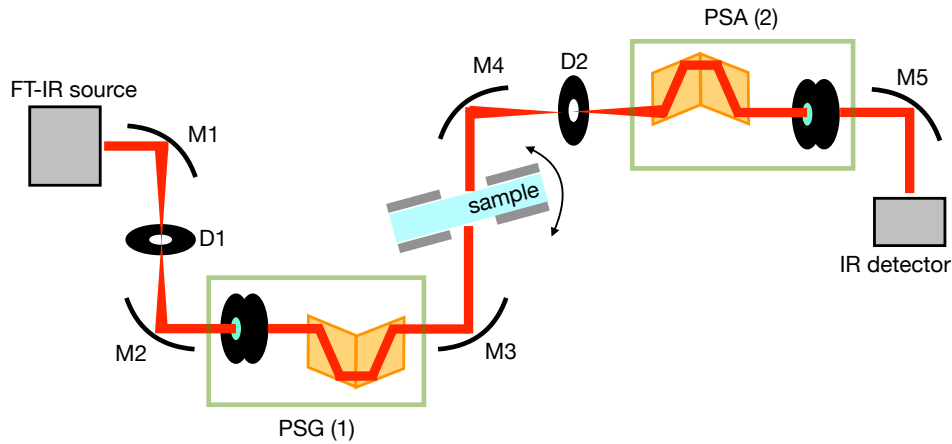
FIGURE 8.7: schema of the IR Mueller ellipsometer. (1) polarization state generator in the entry arm; (2) polarization state analyzer in the exit arm; D1-D2: diaphragms; M1-M5 mirrors.

The light beam is directed through the Mueller ellipsometer by a series of coated gold mirrors (M1 to M5). [73] The differential Mueller matrix formalism describes the evolution of the polarization and depolarization properties of a continuous medium along the path-length traveled by light through it. For a nondepolarizing medium, such is the case for the PVDF film, the decomposition of the Mueller matrix, **m**, contains the six elementary polarization properties fully characterizing the medium: linear dichroism (LD) and birefringence (LB), 45°-linear dichroism (LD') and birefringence (LB'), and circular dichroism (CD) and birefringence (CB). [74]

$$m = \begin{pmatrix} 0 & LD & LD' & CD \\ LD & 0 & CB & -LB' \\ LD' & -CB & 0 & LB \\ CD & LB' & -LB & 0 \end{pmatrix} \tag{8.3}$$

The PVDF film is mounted on a specific sample holder with two degree of freedom: rotation around y (φ angle) and z (θ angle) axis, respectively (Figure 8.8). The first step consists to orient the sample perpendicular to the IR beam (θ=0). The birefringence axis was found for small rotation of φ around φ=0. The birefringence axis is the direction where the sum of the dipoles, in a molecule, is zero.

Fixing the configuration of zero birefringence, the angle of incidence (θ) change from -30° to 30° in 5° steps. $\theta = 0°$ corresponds to illuminate the sample at normal incidence.

Considering the system such as polarized PVDF film, the presence of the oriented dipoles results in a total dichroism different from zero (<D>≠0). In the chapter results (9), we will show how for some FT-IR peaks the rotation (around z-axis)
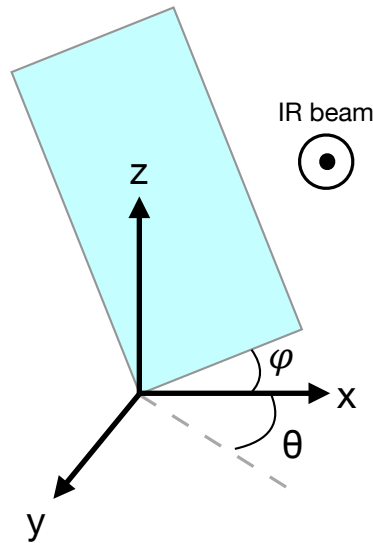
FIGURE 8.8: orientation of the PVDF film respect to IR beam: rotation around y (φ angle) and z (θ angle) axis.

affects the intensity of the peaks.

8.6 Dielectric measurement

The dielectric measurements were performed at université du Maine (IMMM, Prof. M. Tabellout). The sample were prepared with two concentric electrodes: one on the bottom (diameter=2cm) and one on the top (diameter=1cm). The films were tested in frequency between 0.1Hz and 10MHz at 30°C.

Figure 8.9 shows the typical dielectric permittivity (ϵ') and dielectric loss (ϵ'') of a polarized PVDF film. The dielectric permittivity was evaluated taking the mean value between 0.1 and 10kHz. The corresponding value for neat PVDF is ϵ'=12.3. The dielectric loss in Figure 8.9 shown a peak around 5MHz relative to the glass transition relaxation of PVDF (α relaxation). [75]
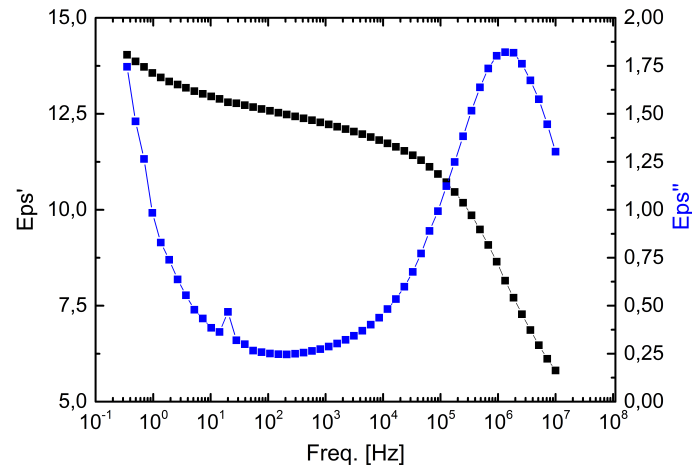
FIGURE 8.9: ϵ' and ϵ'' function of frequency.

8.7   Elastic modulus

The elastic modulus was evaluated by uniaxial tensile test. The PVDF film (dimension: 40mm×20mm×9μm) is fixed between two collets. The tested sample length (L_0) is equal to 20 mm . The remaining part (10 mm for each side) is clamped in the collets. The PVDF film is stretched in an uniaxial direction as shown in Figure 8.10. The measurement is performed at constant strain rate (2mm.min^{-1}).
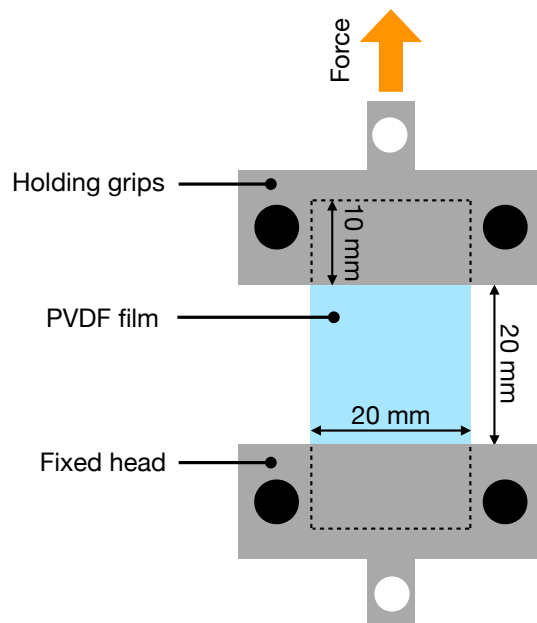
FIGURE 8.10: collets for tensile test measurement.

During this process, the elongation of the film is recorded against the applied force. From the elongation measurement, we are able to evaluate the strain,ϵ, using the following equation: $\epsilon = L - L_0/L_0$, where L_0 and L are the initial and

final length, respectively. The stress is calculated as following: $\sigma = F/A$, where F is the applied tensile force and A is the nominal cross-section area of the sample. Figure 8.11 shows the stress-strain curve obtained by tensile test. The Young modulus is evaluated by linear fitting of the curve in the elastic region (between 5 and 30MPa). The Young modulus is around 2.5 GPa. The fracture strength for the neat PVDF is around 80 MPa.
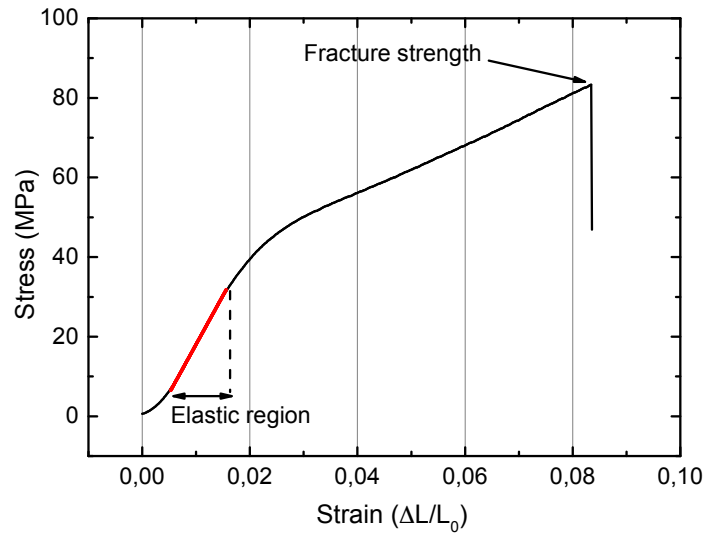
FIGURE 8.11: Stress *vs* strain of neat PVDF film.
fit function: $\sigma = -6,475 + 2454,45\epsilon$

Chapter 9

Results and discussions

The goal of this work is to realize a piezoelectric nanostructured PVDF for harvesting energy applications. The track-etched technique is the main step of the nanostructuration. Two different radiation sources (SHI and e-beam) are explored to study the impact of structural defects in the piezoelectric response of the bi-oriented PVDF film. The chapter is divided in two parts:

- In the first part, I'll investigate the piezoelectric response after the radiation step (section 9.1). PVDF film undergoes significant structural changes in the investigated doses range. The large amount of defects, such as crosslinks and chain scissions, affects crystallinity, elastic modulus, permettivity and piezo-response. All these structural changes are analyzed by different characterization techniques, as described in section 9.2.

- In the second part, the preliminary results of the nanostructured PVDF film with electrodeposited Ni NWs are presented (section 9.3). The following approach of piezo-generators based on metallic NWs embedded in nanoporous piezoelectric PVDF membranes will be addressed in order to meet to the best to the energetic requirements. The nature, diameter and fluence of various metallic nanowires electrodeposited in nanoporous piezoelectric PVDF film and the device designs with environmental vibration sources have to be investigated and combined to optimize the electrical generation capacity of generators based on PVDF membranes. In the present PhD work, as it is pioneer, we have chosen to work on a unique system with Ni NWs of 50nm of diameter at the fluence of 5.10^8 cm^{-2} embedded in β-PVDF film of $9\mu m$ thick. In this chapter, we are combining all previous results in terms of radiation effects to complement the hybridization expected effect from state-of-the-art on the resulted piezoelectric response of these novel materials.

9.1 Conservation of the piezoelectric effect under radiation sources

The preservation of the piezoelectric response under SHI irradiation (fluence equals to $10^9 cm^{-2}$) was shown by Chung *et al.* [55] High fluences (>$10^{10}.cm^{-2}$), contrinutes to depolarize the latent tracks with a consequently decreasing the piezoelectric coefficient d_{33}. [28]

Radiation has shown to be a competitive way to modify the structural and physical properties of the piezoelectric polymer. Zhang *et al.* reported an exceptionally high electrostrictive response for the copolymer P(VDF-TrFE) following e-beam irradiation in the range of $0.4 - 1MGy$. At room temperature, under an electric field of $150MV.m^{-1}$, the longitudinal strain reaches more than 4%. Clearly, materials with such high electrostrictive strain are attractive for actuator, and transducer applications. [18]

The latter study concerning irradiation effect in copolymer pointed out how structural defects change the elasticity of the polymer in the inverse piezoelectric effect. As piezoelectricity is a reversible phenomenon, it is tempting to exploit irradiation in polarized PVDF to enhance the direct piezoelectric response in view of harvesting energy application.

Using the pressure cell, described in section 7.3, we are able to measure the output voltage function of the applied pressure. Figure 9.1 shows the characteristic curve for reference (non-irradiated) PVDF at different change of pressure (ΔP). These curves are obtained measuring the output voltage at the external resistance of $500k\Omega$ connected in parallel with the piezoelectric PVDF. The application load frequency is 10 Hz.
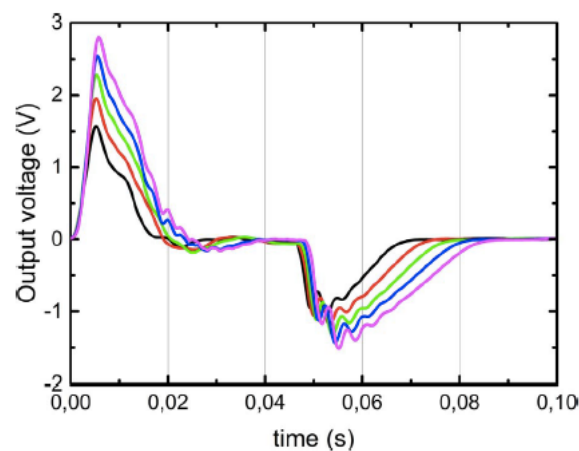
FIGURE 9.1: output voltage at various air pressures variation. Black line (ΔP=0.08bar); red line (ΔP=0.18bar), green line (ΔP=0.28 bar), blue line (ΔP=0.38 bar), magenta line (ΔP=0.48bar).

Polarized PVDF reference is tested to prove the feasibility in the harvesting energy context. Figure 9.2 shows the complete set-up to harvest energy. In particular, the PVDF film is bended using compressed air as described in chapter 7. The output voltage is rectified by a diode bridge. The output current is stored in a capacitance, and it is used to light two LEDs.
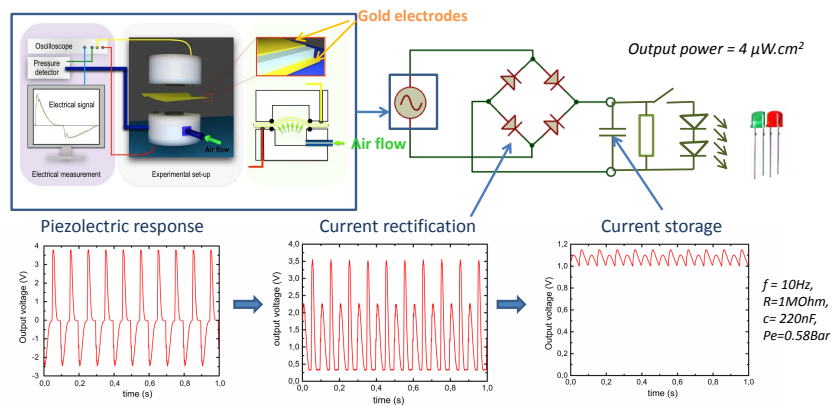
FIGURE 9.2: electrical circuit used to harvest energy from a piezoelectric PVDF film.

In this study, we investigate the effect of the e-beam and SHI (irradiation performed as in section 7.1). The investigated irradiation doses are in a range between 0 and 100kGy. Referring to the positive output voltage peak, the response is plotted as a function of the applied pressure (Figure 9.3). The standard error, indicated in Figure 9.3, is relative to the PVDF reference. All the other points, which are inside the error bar, correspond to the irradiated sample. Therefore, the piezoelectric response is preserved under these two irradiation source conditions.
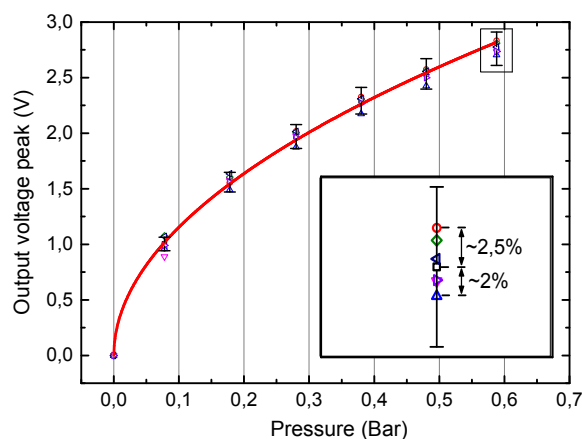
FIGURE 9.3: irradiated polarized PVDF films output voltages at various pressures – PVDF reference: (□); electron irradiated doses: 5kGy (○), 25kGy (△), 100kGy (▽) ; SHI irradiated doses: 0.076 kGy (◇), 0.76 kGy (◁), 7.6 kGy (▷).

The quasilinear response in Figure 9.3 could be due to local curvatures of the clamped film. In fact, in our device, the film is clamped over a circle and stress is exerted by means of the difference of hydrostatic pressure applied on both sides. Prior to apply pressure, inevitably the membrane is not fully extended but a bit loose with some local curvatures that cancel in average. Thus, in a first stage, the pressure extends the film to the shape of a spherical cap with uniform local curvature. Only then, the pressure radially stretches the membrane. Thus, the deformation is in two stages: the first stage is mainly a bending (change of curvature at constant area); whereas the second stage mixes bending and radial stretching (change of area). Now, it is important to notice that bending the membrane is easier than stretching it. Also, during the first stage the center of mass of the membrane moves, thus due to the fundamental principle of dynamics the first stage takes less time as the pressure increases.

The electrical efficiency was estimated as in section 7.5. The external circuit is formed by an external resistance of $500k\Omega$ connected in parallel with the piezoelectric PVDF. Note: R_{osc} is taken into account in the final resistance R=$500k\Omega$.
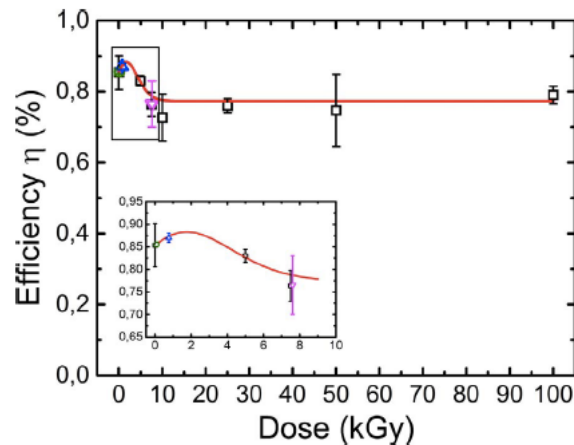
FIGURE 9.4: efficiency *versus* irradiated doses. Electron irradiated doses: 0, 5, 10, 25, 50, 100 kGy (□); SHI irradiated doses: 0.076 kGy (□), 0.76kGy (△), 7.6kGy (▽).

The conversion efficiency was found to be around 0.8% with a slight positive variation between 15-20kGy as shown in Figure 9.4 . These results were unexpected as the PVDF film should have undergone significant structural changes from 5 to 100 kGy due to the large amount of defects such as crosslinking, chain scissions and radicals. All of these combined structural changes lead to slight modifications of the electrical efficiency and correlatively preserve the piezoelectric properties of the material.

9.2   Irradiated samples characterizations

In order to investigate deeper the role of the irradiations in the piezoelectric PVDF film a list of characterizations will be presented. The crystallinity is studied by DSC and XRD techniques. Ellipsometry and FT-IR are used to investigate dichroism and crystalline phases, respectively. Permittivity and elastic modulus measurement allow to determine the irradiation effects on the piezoelectric and mechanical properties of the PVDF.

9.2.1   DSC and XRD

DSC technique was used to detect the crystallites size and the crystalline content in PVDF bulk. In Figure 9.5(a) is shown the endothermic peak of the PVDF crystalline part for different irradiation doses. The trend observed shows a shift of the melting peak with the irradiation doses. The bimodal shape observed from 10 kGy for the irradiated samples, suggests that the crystallite size significantly decreases. Globally, the overall degree of crystallinity remains around 35%. The dose-gel of PVDF is known to be in the range of 9.9-35.1 kGy. [24]. According to Figure 9.5(b), the gel dose can be arranged around 15–20 kGy in our thin polymer films. Below gel dose, chain scissions predominantly occur. The irradiation thus creates shorter polymer chains and reduces the number of entanglements per molecule which, in turn, increase molecular mobility. As a result, the crystallinity content increased from 35% to 43%. Above gel dose, crosslinking of PVDF reduces the mobility of the polymer chains.
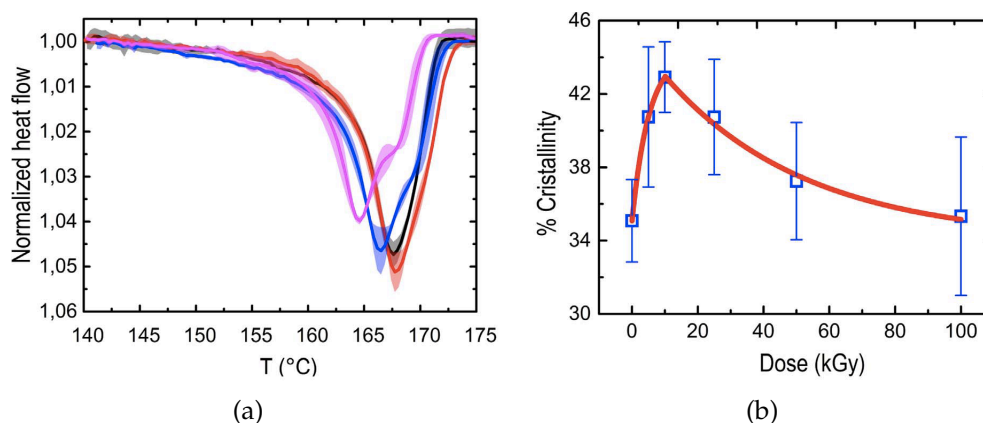
FIGURE 9.5: (a). Differential Scanning Calorimetry spectra registered at 20°C.min^{-1} - focus in the PVDF melting peaks region between 140°C and 175°C at e-beam irradiation doses of 0 (black line), 5 (red line), 10 (blue line) and 100 kGy (magenta line). Curve shadows represent error bar variations. (b). Degree of crystallinity *versus* irradiated doses.

The variation of crystallization in the PVDF, after irradiation, drives us toward the second characterization technique: X-ray diffraction. Due to the discrimination between phases, we are able to evaluate which phase increases at fixed irradiation dose. The XRD spectra of the irradiated samples were fitting by *pseudo-voigt* function as described in section 8.2. The area corresponding to the crystalline peaks were measured. We indicate with A_α and A_β the areas of the α and the total β (peak area (110) + (200)) phase, respectively. As shown in Table 9.1 the α and β crystalline fraction ((A_α/A_{tot})% and (A_β/A_{tot})%) were found around 26% and 74%. If we look deeper, at 5 kGy of irradiation dose the β fraction goes from 71% to 76%, and, the α phase is reduced to 23% starting from 28%. For higher doses, slight variation of β fractions were observed. However, whatever the dose investigated in the range 5-100 kGy, the β fraction is higher than the reference at 0kGy.

TABLE 9.1: Variation of α and β crystallinity fraction function of
irradiation doses

Irr. Dose (kGy)	(A_α/A_{tot})%	(A_β/A_{tot})%
0	28.7	71.3
5	23.8	76.2
10	24.6	75.4
25	27.1	72.9
50	27.1	72.9
100	25.5	74.5

Comparing the data obtained by DSC and XRD, we can conclude that an increase of the crystallization was observed at low range doses (5-20 kGy). The increasing of crystallization is related to β phase.

9.2.2   FT-IR and ellipsometry

FT-IR spectroscopy allows an accurate discrimination between α, β crystalline phases as already discussed in section 8.1. We have chosen absorption bands at 615 cm^{-1} and 840 cm^{-1} as signature of α-phase and β-phase, respectively. A comparative study was performed based on the intensity variation of the FT-IR peaks function the radiation dose.

As displayed in Figure 9.6 the slight increase of the β-phase up to 10 kGy is accompanied by a decrease in the α-phase of the same magnitude. At 100 kGy β-phase attributed peak at 840 cm^{-1} comes back to its initial value. It confirms that the β-phase content is globally not affected by irradiation and its growth is even more favorized at very low doses. This can be due to the chain scission effect, predominant at low doses below 10 kGy, which enhances the polymer chains mobility. The FT-IR technique confirms the trend observed by XRD.
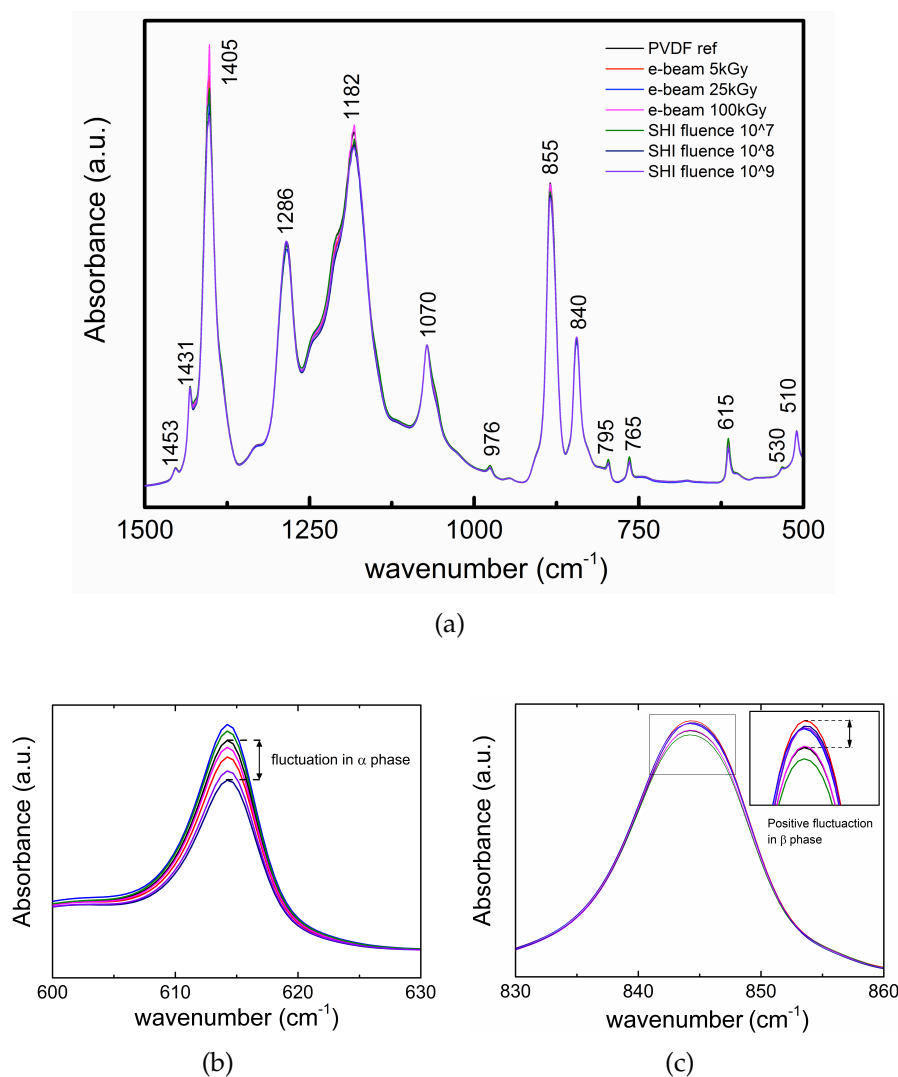
FIGURE 9.6: (a). FT-IR spectra in transmission mode of polarized bi-oriented polarized PVDF treated at various doses using electrons (normalized band was 1070 cm^{-1}): 0 kGy (black line), 5 kGy (red line), 25 kGy (blue line) and 100 kGy (magenta line) and using SHI at doses of 0.076 kGy (green line), 0.76 kGy (cyan line) and 7.6 kGy (violet line). (b). 615 cm^{-1} α peak. (c) 840 cm^{-1} β peak.

Ellipsometry is a sensitive technique to detect the orientation of the dipole in the PVDF film. As introduced in section 8.5, the presence of the oriented dipoles results in a total dichroism different from zero (<D>$\neq$0). The rotation around z-axis (θ angle) changes the orientation of the dipole respect to the incident IR beam. The dichroism matrices M_{12} and M_{13} were analyzed. M_{12} is Linear Dichroism (LD) which is defined as the difference between absorption of polarized light parallel and perpendicular to an orientation axis. M_{13} represents the linear dichroism along the $+45°$ and $-45°$.

M_{12} and M_{13} spectra are shown in Figure 9.7 function of θ (from $\theta = 0°$ to $\theta = 30°$, step $\theta = 5°$) for the PVDF reference (0 kGy).
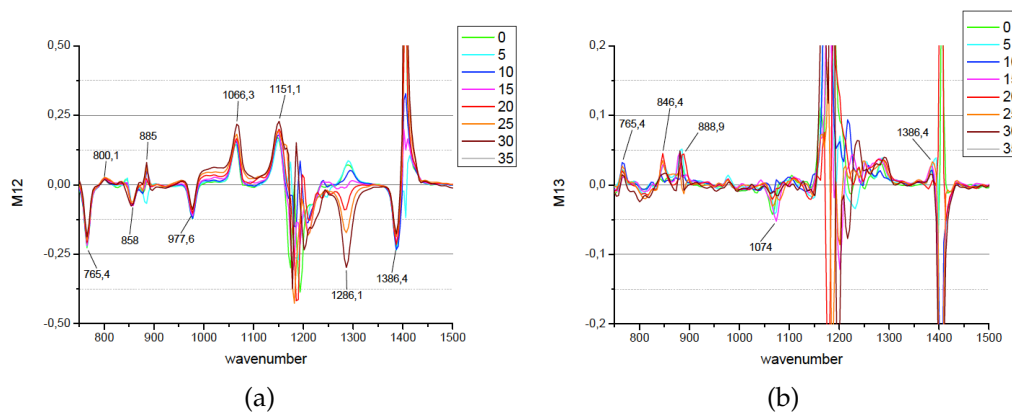
FIGURE 9.7: spectra dichroism matrix: (a) M_{12} and (b) M_{13} for PVDF reference. β peak of interest: 1286 cm^{-1}. Huge intensity variation in M_{12} function of θ angle (range 0 - 30deg)

Intensity variations of the peaks at $844.cm^{-1}$ and $1286.1.cm^{-1}$ were observed. As we already shown in FT-IR section 8.1, these two peaks belong to β-phase. In particular, $844cm^{-1}$ and $1286cm^{-1}$ are related to the asymmetric and symmetric stretching of CF_2 respectively. Finally the intensity variation of the peak at $1286cm^{-1}$ is more accentuated than the peak at $844cm^{-1}$. The dichroism of the CF_2 symmetric stretching has been previously exploited by Sakata *et al.* in order to determine the orientation of the dipoles in the β phase. [70] Due to the randomly orientation of the dipoles, no intensity variations were observed in the remaining peaks shown in Figure 9.7(a). These peaks are related to α (peaks at $763.cm^{-1}$ and $976.cm^{-1}$) and amorphous phase. Unlike the β phase, α phase doesn't show a preferential orientation of the dipoles. M_{13} is shown in Figure 9.7(b). The different polarization directions of the light not allow an interaction with the dipole of β phase. No peaks were observed at $844cm^{-1}$ and $1286cm^{-1}$.

In conclusion, the analysis of the strong angular dependence of dipoles with the polarized light leads to determine the orientation of the dipoles. Combining the information of the linear dichroism M_{12} and M_{13}, the resulting orientation of the β dipoles is perpendicular to the film surface.

Regarding the irradiated PVDF films (in the range doses 5-100kGy), the maximum intensity peak at $1286cm^{-1}$ ($\theta = 30°$) not shows relevant variation. Therefore, the irradiation doesn't affect the orientation of the dipoles or its density (Figure 9.8). The orientation of the dipoles was calculated around $89° \pm 5°$ respect to surface of the film for all the irradiated and non-irradiated samples. Note that a direct comparison of the irradiated samples with the M_{12} spectrum in Figure 9.7(a) is not possible. In fact, due to a rotation φ equals to $90°$, the PVDF reference shows a positive peak at θ equals to $0°$, $5°$, and $10°$. An in-plane interaction

has also been found between the IR-beam and the asymmetric and symmetric stretching CF_2.
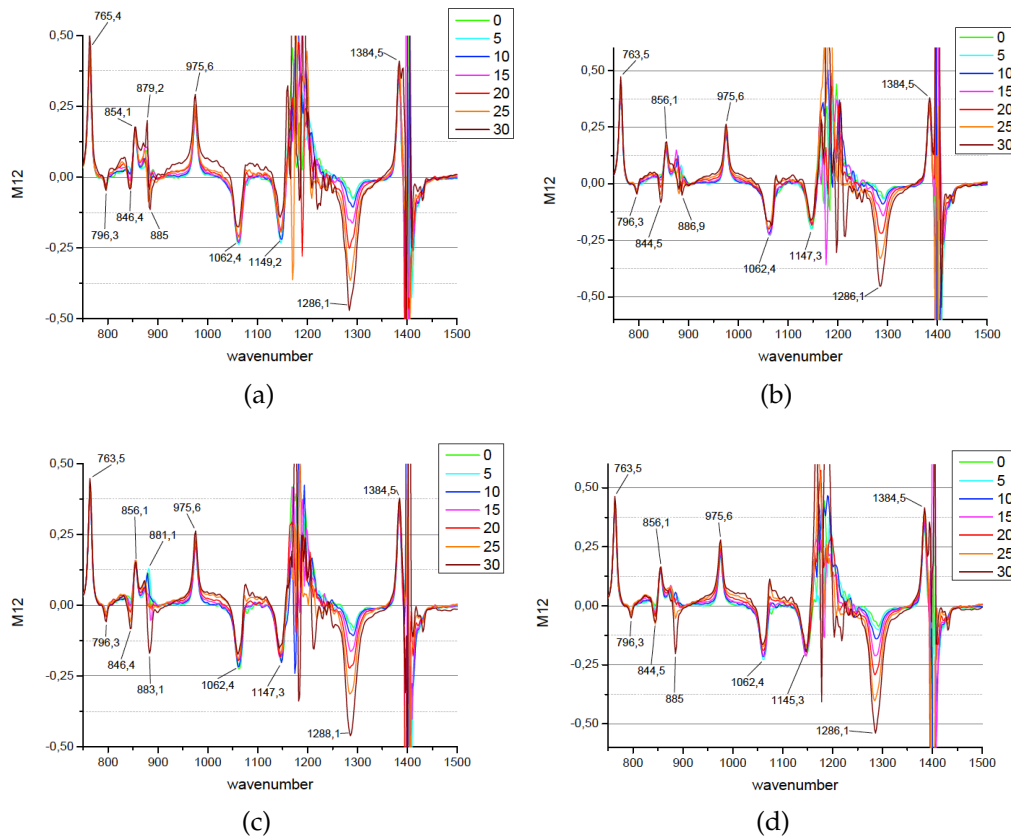
FIGURE 9.8: spectra dichroism matrix M_{12} function of θ angle (range 0 - 30*deg*) for irradiated PVDF. Irradiation doses: (a). 5kGy; (b). 10kGy; (c). 50 kGy; (d). 100kGy.

9.2.3   Dielectric and elastic modulus measurement

The slight increase of crystallinity around 10 kGy, confirmed by fluctuation in XRD and FT-IR spectra, has driven us to investigate deeper the mechanical and electrical properties of the polymer after irradiation. The piezoelectric response results of the β-phase crystallites polarization. It thus reflects the dipole orientation of the crystallites and their mobility in the material. Therefore, dielectric permittivity, elasticity and remanent polarization components are the three major parameters describing the system.

Measurements of the dielectric permittivity, ϵ', were performed at room temperature on the irradiated samples. As shown in Figure 9.9(a), no evident variations were reported for the irradiated and non-irradiated PVDF in term of ϵ'. The dielectric loss ϵ'' (Figure 9.9(b)) shown the PVDF glass transition relaxation peak, which remains stable around 5MHz for all the irradiated samples.
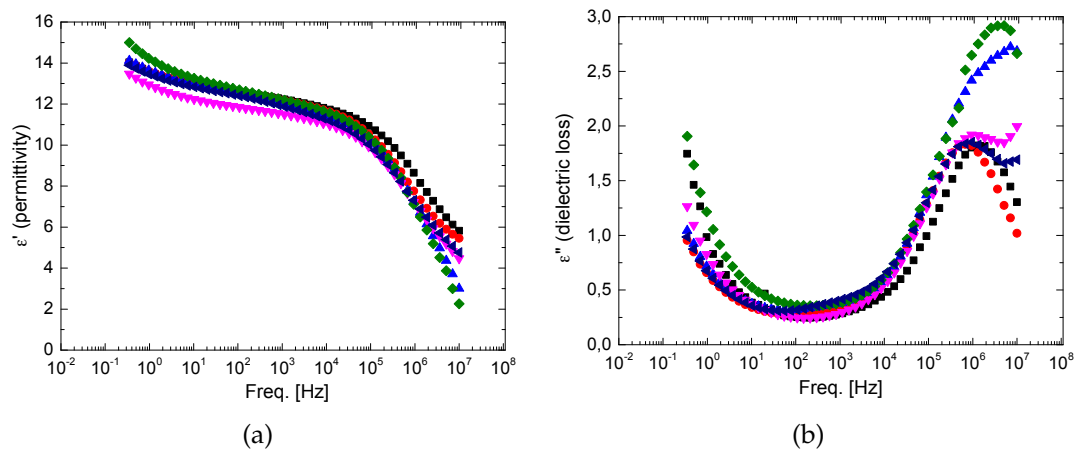
FIGURE 9.9: (a). Dielectric permittivity (ϵ'); and (b) dielectric loss (ϵ'') at e-beam radiation doses (kGy): 0 (■), 5 (●), 10 (▲), 25 (▼), 50 (◆), 100 (◀)

The electric displacement, D, is proportional to the dielectric permittivity of the PVDF as described in section 2.1. The irradiation not affect dipoles density. As PVDF undergone significant structural changes in the studied dose range, the elasticity of the polymer should be affected. Measurement of the elastic modulus were performed for the irradiated samples.

As shown in Figure 9.10 the increase of smaller crystallites, in the PVDF irradiated at 10kGy, have an effect on the elastic modulus: respect to the rest of the tested irradiated samples it comes out of the error bar of the reference. This result confirms that, below the gel dose, chain scissions predominantly occur leading to shorter polymer chains and a higher molecular mobility. The consequence is the slight increase of β-phase crystallites content. Together with the elastic modulus increase a slight increase of the efficiency is thus enhanced below 10 kGy (Figure 9.4). The measured value is around 2.95GPa.

No relevant variation of the fracture strength were observed on the irradiated samples.
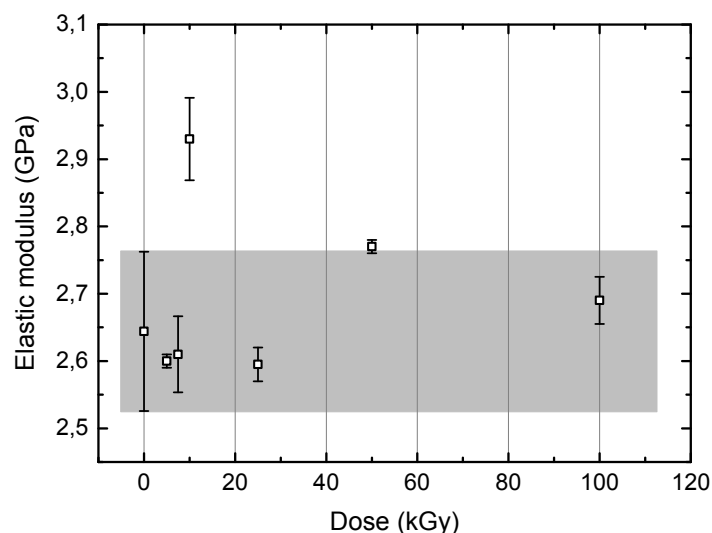
FIGURE 9.10: elastic modulus *versus* e-beam radiation doses (kGy).

In order to give an idea of the significant structural change in the doses range 5-100kGy, we illustrate the irradiation effects in a copolymer P(VDF-TrFe)(70/30). As shown in Figure 9.11(a), the fracture strength of the P(VDF-TrFe) is function of the radiation dose. The initial value, 40MPa for the P(VDF-TrFe) reference (non-irradiated), is reduced to 11MPa at dose equals to 100kGy. After 25kGy, the copolymer became brittle and the fracture occurred in the elastic region (Figure 9.11(b)). The young modulus undergoes a slight decrease until 50 kGy. The decrease became more evident at 100kGy. Contrary to the PVDF, the copolymer P(VDF-TrFe) doesn't show an increase of the elastic modulus at 10 kGy or at other doses.

(a)

(b)
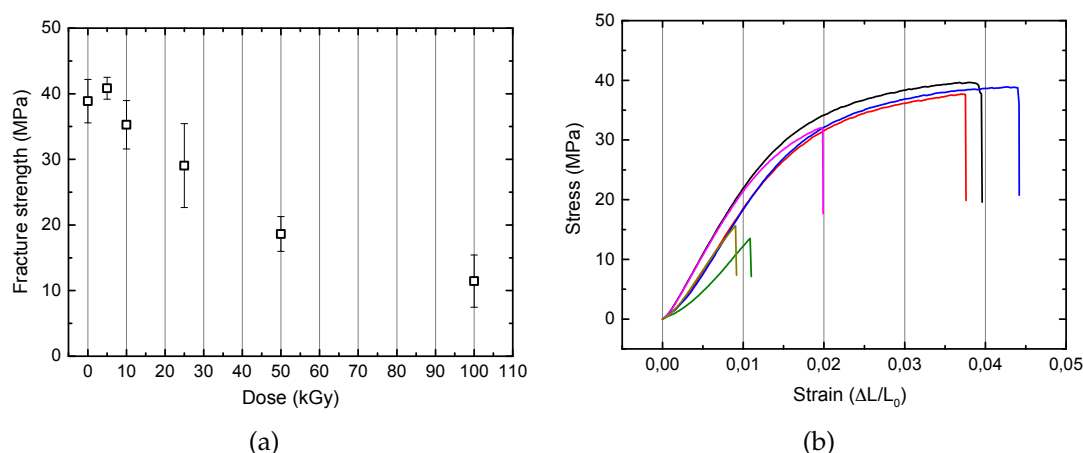
FIGURE 9.11: (a). Fracture strength (MPa) *versus* e-beam radiation doses (kGy) of a copolymer P(VDF-TrFe)(70/30); (b). Stress-Strain curves of an irradiated copolymer P(VDF-TrFe)(70/30) at different doses (kGy): 0 (black line), 5 (red line), 10 (blue line), 25 (magenta line), 50 (olive line), 100 (green line).

The results obtained for the copolymer pointed out the outstanding radiation resistance of the PVDF.

9.3 Nanostructuration effect on the piezoelectric response

In this section, we report the main results obtained in term of piezoelectric response, for the nanocomposite PVDF/Ni NWs. The nanostructuration steps are described in section 7.2.

In the previous sections, it has been illustrated how the radiation for a given energy, fluence and doses doesn't affect the piezoelectric response of the PVDF. Going deeper in the nanostructuration steps, chemical etching of the film results in a dramatic decrease of the piezoelectric response efficiency. Figure 9.12 shows a net decrease of the efficiency with the etching time.
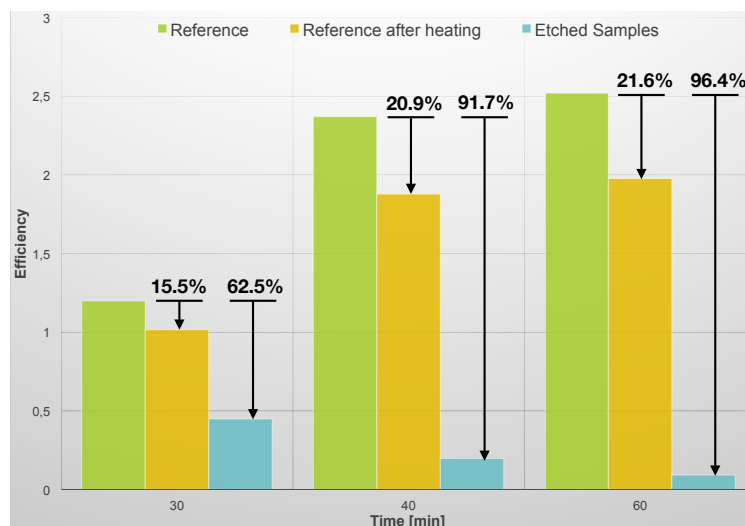
FIGURE 9.12: chemical etching impact on the electric efficiency. Etching times: 30, 40 and 60 minutes. PVDF Reference (■), temperature (■) and chemical etching (■) impact on the electrical efficiency.

Three aspects contributes to the decreasing of the piezoelectric efficiency:

- Temperature effect: the samples were maintained at 65°C din the etching solution for 30, 40 and 60 minutes. A parallel experiment was provided using water. In this case, only the effect of temperature on the piezoelectric response was considered. Temperature reduces the electrical efficiency by 20% (Figure 9.12).

- The nanopores diameter relative to 30 and 60 minutes of etching correspond around to 60 and 120 nm, respectively. Considering the fluence of

$5.10^8.cm^{-2}$, the volume reduction after chemical etching was equal to -1.40% and -5.7% for 30 and 60 minutes etching, respectively.

- The creation of new surfaces (nanopores) could contribute to destabilize the dipole orientation. The structural modification of the PVDF, due to the presence of the nanopores, interrupts the periodic arrangement of the crystallinity phase.

Note that in Figure 9.12 the green columns (PVDF references without etching) show different value of efficiency. The PVDF references, used in my experiments, show significant variation of remanent polarization due to an inhomogeneity in the commercial film. In Figure 9.13, we report an etching time corresponding to 30 minutes with an additional column related to the efficiency of the nanocomposite PVDF/Ni NWs.
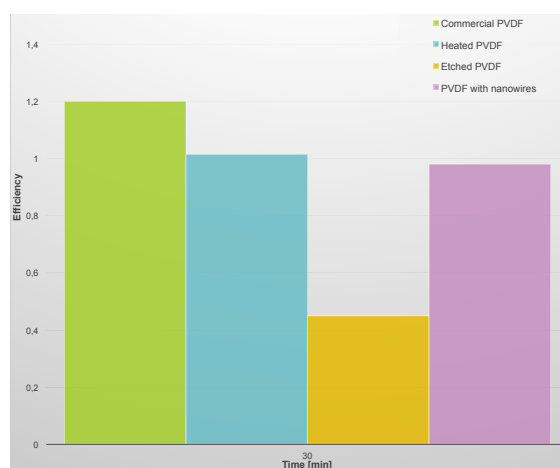
FIGURE 9.13: chemical etching impact on the electric efficiency. Etching time: 30 minutes. PVDF Reference (■), temperature (■), chemical etching (■) and Ni NWs (■) impact on the electrical efficiency.

The nanowires are electrodeposited as described in section 7.2. The presence of Ni NWs lead to restore the drastic decrease due to the chemical etching. The thermal effect is not recovered.

The presence of the nanowires increases the efficiency for all the electrodeposition time: 50, 100, and 150 seconds. The results are shown in Figure 9.14. The maximum is reached at 100 seconds. A further increase of the electrodeposition time (150 seconds) decreases the efficiency.
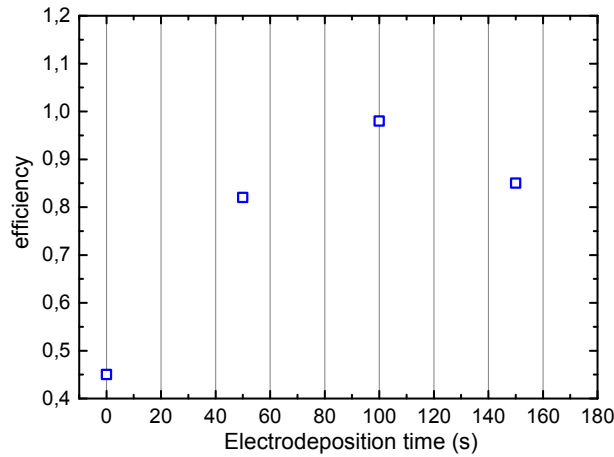
FIGURE 9.14: electrical efficiency *versus* electrodeposition time (s).

The presence of the Al_2O_3 layer and Ni NWs in the nanocomposite leads to frequency dependence ϵ' at low frequency range (0-10Hz). As shown in Figure 9.15, the presence of nanopores doesn't not affect the constant permittivity in the range of 10-100kHz respect to the neat PVDF ($\epsilon' \simeq 12$). Moreover, Al_2O_3 contributes to increase the *static permittivity*. The static permittivity is defined as the permittivity at null frequency. A further increases of the static permittivity comes from the Ni NWs. Considering the electrodeposition times 50, 100, and 150 s, $\epsilon'(0)$ reaches a maximum at 100 seconds of electrodeposition time, afterwards it starts to decrease. This variation reflects the trend observed in Figure 9.14. The Ni NWs allow a slight increase the constant permittivity (until $\epsilon' \simeq 18$) in the range 10-100kHz.
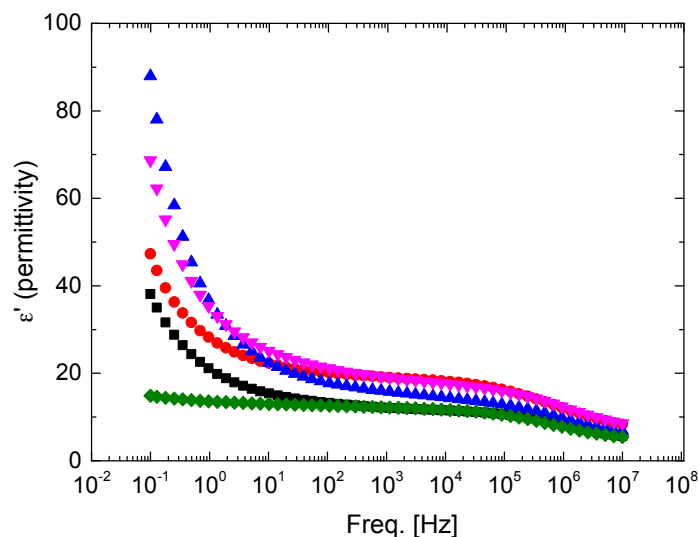
FIGURE 9.15: dielectric permittivity (ϵ') for nanostructured samples. PVDF reference (♦), nanoporous PVDF/Al_2O_3 layer (■), Electrodeposition times of the Ni NWs: 50 (●), 100 (▲), 150 seconds (▼).

As observed in chapter 2, the permittivity constant is proportional to the dipole density in the PVDF. Therefore, the net increases of the piezoelectric response, after chemical etching, could be related to the presence of the Ni NWs.

9.4   Conclusion

In the first part of this chapter, we irradiated bi-oriented piezoelectric PVDF film with SHI and e-beam sources in a range between 0 and 100kGy. Respect to the non-irradiated PVDF film, whatever the accelerated particles composing the irradiation beam, the irradiated PVDF film exhibits a similar output voltage peak and electrical efficiency for doses below 100 kGy. The remarkable conservation of the piezoelectric response of polarized PVDF thin films is of great interest for many researchers developing devices using this piezoelectric polymer devoted to space environment.

These results were unexpected as the PVDF film should have undergone significant structural changes from 5 to 100 kGy due to the large amount of defects such as crosslinking, chain scissions and radicals. Due to chain scissions, between 5 and 10kGy, the degree of crystallinity exhibits an unexpected 8% increase. At higher doses (up to 100 kGy), this increase is followed by a decrease of similar amplitude. The overall degree of crystallinity remains around 35%. The increase of crystallinity is related to the β phase, as confirmed by the XRD and FT-IR techniques. Despite the increase of the β phase, no enhancement of the piezo-response was remarked. Two possible explanations:

- The sensitivity of the instrument is not enough to detect the variation of the piezo-response after irradiation.

- A new poling step needs to polarize the additional β phase.

As shown by ellipsometry and dielectric measurement the dipole density, in the PVDF, is not affected by radiations (according with the conservation of the piezoelectric response). At irradiation dose equal to 10kGy, PVDF exhibits a high value of the Young modulus (2.95 GPa), related with the increase of the chain scissions and smaller crystallite content.

The radiation resistance of the piezoelectric response allows the nanostructuration of the PVDF film using SHI irradiation. The chemical etching step, in the nanostructuration process, results in a dramatic reduction of the piezoelectric response. The electrodeposition of Ni NWs leads to restore the electrical efficiency

lost during the chemical etching step. An increase of the static and constant permittivity could explain the presence of an interfacial polarization between PVDF and Ni NWs, resulting in a higher electric efficiency.

Conclusion

The versatility of the track-etching technique has allowed to investigate deeper the direct and inverse piezoelectric effect of a polarized Poly(vinylidene fluoride) (PVDF) film in building nanostructured hybrid Nickel nanowires (Ni NWs)/ PVDF membrane. Different steps are involved. Swift heavy ions irradiation (SHI) first generates, in PVDF film, cylindrical local damage zones (so-called latent-tracks). By subsequent chemical etching, the latent tracks are revealed. Finally, the resulting nanoporous PVDF membrane was used as a template to grow Ni NWs by electrodeposition.

Acting on the electrodeposition technique, a single Ni NW may be contacted. The magnetic properties of the Ni NW, such as anisotropic magneto resistance (AMR), are exploited to investigate the response of the magnetization to a mechanical deformation of the PVDF matrix. In particular, the deformations were induced either by thermo-mechanical or an electro-mechanical (inverse piezoelectric effect) stress. The sensitivity of the single NW has allowed to determine the amplitude and direction of a mechanical stress exerted at the nano-scale by the PVDF matrix.

The outstanding resistance of the direct piezoelectric response of polarized PVDF film to radiation, such as SHI and e-beam, (doses range < 100kGy) was reported. Beyond the conservation of the piezoelectric response, in this dose range, irradiation defects had a significative impact on the polymer material: chain scissions resulting in a clear decrease of crystallites size, an increase of β-phase crystallinity for doses inferior to the gel dose (herein 10 kGy) and the formation of crosslinking with a sharp increase of Young modulus at the PVDF gel-doses. All these defects compensate their antagonistic effects towards the globally unchanged piezoelectric response.

From the last few years, 1D-and 2D-nanostructure systems, such as semiconductor nanowires (NWs) presenting piezoelectric properties and multilayered piezoelectric PVDF composite have recently emerged as excellent candidates to fabricate novel ultra-compact and efficient piezoelectric generators.

Motivated by the high radiation resistance of the PVDF in terms of piezoelectric response, the idea was to exploit Ni NWs array embedded in the polarized PVDF membrane to study the influence of the Ni NWs on the piezoelectric response in

view of harvesting energy application. The presence of the Ni NWs array leads a non-negligible increase of the piezoelectric efficiency. Related to the presence of the NWs, an increase of the dielectric permittivity in the nanostructured PVDF was also reported. An interfacial polarization between the Ni NWs and the PVDF matrix could explain the higher efficiency value respect to nanoporous PVDF, without NWs.

Although the presence of the Ni NWs array contributes to the increase of the piezoelectric response after chemical etching, it is not sufficient to obtain a piezo-electric nanostructured material competitive enough respect to the commercial piezoelectric PVDF. One possible solution could be to change the nature of the NWs. In particular, semi-conductor NWs having piezoelectric properties today exhibit a serious potential to improve the scavenging of mechanical energy and to convert it into electrical energy. Indeed, the generation of electrical energy from the mechanical deformation of ZnO NWs has been demonstrated in 2006 by the Prof. Wang from the Georgia Institute of Technology in USA.
ZnO is also a good candidate for the electrodeposition in the track-etched po-larized PVDF film. Contrary to the Ni NWs array, a further contribution at the global piezo-potential may arise from ZnO NWs array.
Bismuth NWs could also be of great interest in combining piezoelectrical re-sponse of ion-beam nanostructured PVDF film with other energy harvesters. I recently proposed a project to exploit the track-etched PVDF as a template for thermoelectric NWs. The hybrid nanogenerator combines two effects. On the one hand, based on the Seebeck effect, the Bismuth NWs will be able to harvest electrical energy as long as a temperature difference is maintained across the de-vice. On the other hand, spontaneous polarization in the PVDF pyroelectric film will allow recovering electrical charge by time-dependent temperature variation.

In conclusion, the flexibility and piezoelectric properties of the PVDF makes this polymer unique. Nevertheless, the use as electrical generators has been rather limited due to their relatively low power output. Today, with the decrease of energy consumption of portable electronic devices, this limitation becomes less critical and the concept of harvesting renewable energy in human surrounding gains a renewed interest. However, the size of the conventional piezoelectric generators often represents a major limitation to their integration into small-scale devices.
In my thesis, I propose a new approach to the nanostructuration of the PVDF us-ing the track-etching technique. The nanostructuration of the PVDF is the only

way to obtain a more competitive material with a higher output power density leading to an easier integration in portable devices. This thesis work represents the first step toward a more efficient nanostructured PVDF. In fact, alternative solution, to the Ni NW, may be found using ZnO and Bi NWs respectively in the piezoelectric and thermoelectric context.

Bibliography

[1] Kawai, H. *Japanese Journal of Applied Physics* **1969**, *8*, 975.

[2] Cha, S.; Kim, S. M.; Kim, H.; Ku, J.; Sohn, J. I.; Park, Y. J.; Song, B. G.; Jung, M. H.; Lee, E. K.; Choi, B. L.; Park, J. J.; Wang, Z. L.; Kim, J. M.; Kim, K. *Nano Letters* **2011**, *11*, 5142–5147.

[3] Fang, J.; Wang, X.; Lin, T. *Journal of Materials Chemistry* **2011**, *21*, 11088–11091.

[4] Lee, H. Y.; Choi, B. *Smart Materials and Structures* **2013**, *22*, 115025.

[5] Chang, C.; Tran, V. H.; Wang, J.; Fuh, Y.-K.; Lin, L. *Nano Letters* **2010**, *10*, 726–731.

[6] Shenck, N. S.; Paradiso, J. A. *IEEE Micro* **2001**, *21*, 30–42.

[7] Taylor, G. W.; Burns, J. R.; Kammann, S. A.; Powers, W. B.; Welsh, T. R. *IEEE Journal of Oceanic Engineering* **2001**, *26*, 539–547.

[8] Sohn, J. W.; Choi, S. B.; Lee, D. Y. *Proceedings of the Institution of Mechanical Engineers, Part C: Journal of Mechanical Engineering Science* **2005**, *219*, 429–436.

[9] Potkay, J. A.; Brooks, K. *2008 2nd International Conference on Bioinformatics and Biomedical Engineering* **2008**, 1580–1583.

[10] Nakajima, T.; Okaya, K.; Ohta, K.; Furukawa, T.; Okamura, S. *Japanese Journal of Applied Physics* **2011**, *50*, 09ND14.

[11] Tsangaris, G. M.; Psarras, G. C.; Kouloumbi, N. *Journal of Materials Science* **1998**, *33*, 2027–2037.

[12] Jain, A.; K. J., P.; Sharma, A. K.; Jain, A.; P. N, R. *Polymer Engineering & Science* **2015**, *55*, 1589–1616.

[13] Amoresi, R. A. C.; Felix, A. A.; Botero, E. R.; Domingues, N. L. C.; Falcão, E. A.; Zaghete, M. A.; Rinaldi, A. W. *Ceramics International* **2015**, *41*, 14733–14739.

[14] Ferry, M.; Ngono-Ravache, Y.; aymes-chodur, C.; Clochard, M. C.; Coqueret, X.; Cortella, L.; Pellizzi, E.; Rouif, S.; Esnouf, S., *Ionizing Radiation Effects in Polymers*, 2016.

[15] Chailley, V.; Balanzat, E.; Dooryhee, E. *Nuclear Instruments and Methods in Physics Research Section B: Beam Interactions with Materials and Atoms* **1995**, *105*, 110–114.

[16] Clough, R. L. *Nuclear Instruments and Methods in Physics Research Section B: Beam Interactions with Materials and Atoms* **2001**, *185*, 8–33.

[17] Aymes-Chodur, C.; Betz, N.; Porte-Durrieu, M. .-.-C.; Baquey, C.; Le Moël, A. *Nuclear Instruments and Methods in Physics Research Section B: Beam Interactions with Materials and Atoms* **1999**, *151*, 377–385.

[18] Zhang, Q. M.; Bharti, V.; Zhao, X. *Science* **1998**, *280*, 2101.

[19] Giegerich, U.; Wust, J.; Jungnickel, B. J. *IEEE Transactions on Dielectrics and Electrical Insulation* **2000**, *7*, 353–359.

[20] Jean-Mistral, C.; Basrour, S.; Chaillout, J.-J. *Smart Materials and Structures* **2010**, *19*, 085012.

[21] Sodano, H. A.; Liu, Y.; Tian, G.; Wang, Y.; Lin, J.; Zhang, Q.; Hofmann, H. F. *Journal of Intelligent Material Systems and Structures* **2008**, *20*, 575–585.

[22] Vatansever, D.; Hadimani, R. L.; Shah, T.; Siores, E. *Smart Materials and Structures* **2011**, *20*, 055019.

[23] Pae, K. D.; Bhateja, S. K.; Gilbert, J. R. *Journal of Polymer Science Part B: Polymer Physics* **1987**, *25*, 717–722.

[24] Betz, N.; Petersohn, E.; Le Moël, A. *Nuclear Instruments and Methods in Physics Research Section B: Beam Interactions with Materials and Atoms* **1996**, *116*, 207–211.

[25] Adem, E.; Rickards, J.; Burillo, G.; Avalos-Borja, M. *Radiation Physics and Chemistry* **1999**, *54*, 637–641.

[26] Nasef, M. M.; Saidi, H.; Dahlan, K. Z. M. *Polymer Degradation and Stability* **2002**, *75*, 85–92.

[27] Petersohn, E.; Betz, N.; Le Moël, A. *Nuclear Instruments and Methods in Physics Research Section B: Beam Interactions with Materials and Atoms* **1996**, *107*, 368–373.

[28] Hillenbrand, J.; Angert, N.; Hartnagel, H. L.; Neumann, R. *Nuclear Instruments and Methods in Physics Research Section B: Beam Interactions with Materials and Atoms* **1999**, *151*, 123–128.

[29] Spohr, R.; Bethge, K., *Ion Tracks and Microtechnology: Principles and Applications*; Vieweg+Teubner Verlag: 1990.

[30] Gervais, B.; Bouffard, S. *Nuclear Instruments and Methods in Physics Research Section B: Beam Interactions with Materials and Atoms* **1994**, *88*, 355–364.

[31] Balanzat, E.; Betz, N.; Bouffard, S. *Nuclear Instruments and Methods in Physics Research Section B: Beam Interactions with Materials and Atoms* **1995**, *105*, 46–54.

[32] Betz, N. *Nuclear Instruments and Methods in Physics Research Section B: Beam Interactions with Materials and Atoms* **1995**, *105*, 55–62.

[33] Cuscito, O.; Clochard, M. .-.-C.; Esnouf, S.; Betz, N.; Lairez, D. *Nuclear Instruments and Methods in Physics Research Section B: Beam Interactions with Materials and Atoms* **2007**, *265*, 309–313.

[34] Clochard, M. .-.-C.; Berthelot, T.; Baudin, C.; Betz, N.; Balanzat, E.; Gébel, G.; Morin, A. *Journal of Power Sources* **2010**, *195*, 223–231.

[35] Bessbousse, H.; Zran, N.; Fauléau, J.; Godin, B.; Lemée, V.; Wade, T.; Clochard, M.-C. *Radiation Physics and Chemistry* **2016**, *118*, 48–54.

[36] Koukharenko, E.; Li, X.; Nandhakumar, I.; Frety, N.; Beeby, S. P.; Cox, D.; Tudor, M. J.; Schiedt, B.; Trautmann, C.; Bertsch, A.; White, N. M. *Journal of Micromechanics and Microengineering* **2008**, *18*, 104015.

[37] Ferain, E.; Legras, R. *Nuclear Instruments and Methods in Physics Research Section B: Beam Interactions with Materials and Atoms* **2009**, *267*, 1028–1031.

[38] Siddiqui, S.; Kim, D.-I.; Duy, L. T.; Nguyen, M. T.; Muhammad, S.; Yoon, W.-S.; Lee, N.-E. *Nano Energy* **2015**, *15*, 177–185.

[39] Yaman, M.; Khudiyev, T.; Ozgur, E.; Kanik, M.; Aktas, O.; Ozgur, E. O.; Deniz, H.; Korkut, E.; Bayindir, M. *Nat Mater* **2011**, *10*, 494–501.

[40] Jung, W.-S.; Do, Y.-H.; Kang, M.-G.; Kang, C.-Y. *Current Applied Physics* **2013**, *13*, S131–S134.

[41] Kumar, B.; Kim, S.-W. *Nano Energy* **2012**, *1*, 342–355.

[42] *Journal of Applied Physics* **2003**, *93*, 8793–8841.

[43] Dang, Z. .-.-M.; Lin, Y. .-.-H.; Nan, C. .-.-W. *Advanced Materials* **2003**, *15*, 1625–1629.

[44] He, F.; Lau, S.; Chan, H. L.; Fan, J. *Advanced Materials* **2009**, *21*, 710–715.

[45] Defay, E., *integration of ferroelectric and piezoelectric thin films: concepts and application for microsystems*; ISTE Ltd, Wiley: 2011.

[46] Li, Q.; Wang, Q. *Macromolecular Chemistry and Physics* **2016**, *217*, 1228–1244.

[47]   Mohammadi, B.; Yousefi, A. A.; Bellah, S. M. *Polymer Testing* **2007**, *26*, 42–
       50.

[48]   Chelakara Satyanarayana, K.; Bolton, K. *Polymer* **2012**, *53*, 2927–2934.

[49]   Cui, Z.; Hassankiadeh, N. T.; Zhuang, Y.; Drioli, E.; Lee, Y. M. *Progress in
       Polymer Science* **2015**, *51*, 94–126.

[50]   Ranjan, V.; Yu, L.; Nakhmanson, S.; Bernholc, J.; Nardelli, M. B. *Acta Crys-
       tallographica Section A* **2010**, *66*, 553–557.

[51]   De Jong, M.; Chen, W.; Geerlings, H.; Asta, M.; Persson, K. A. *Scientific Data*
       2015, *2*, 150053.

[52]   Mouhat, F.; Coudert, F.-X. *Physical Review B* **2014**, *90*, 224104–.

[53]   Trautmann, C.; Bouffard, S.; Spohr, R. *Nuclear Instruments and Methods in
       Physics Research Section B: Beam Interactions with Materials and Atoms* **1996**,
       116, 429–433.

[54]   Deshayes, S.; Maurizot, V.; Clochard, M.-C.; Berthelot, T.; Baudin, C.; Déléris,
       G. *Radiation Physics and Chemistry* **2010**, *79*, 208–213.

[55]   Pham, D.-C.; Biziere, N.; Melilli, G.; Pajon, R.; Lacour, D.; Bouvot, L.; Tabell-
       out, M.; Lairez, D.; Drouhin, H.-J.; Clochard, M.-C.; Wegrowe, J.-E. *Materials
       Research Express* **2014**, *1*, 045017.

[56]   Bailey, W. J., *Contemporary Topics in Polymer Science*; v. 4; Springer US: 2012.

[57]   Sussner, H. *Physics Letters A* **1976**, *58*, 426–428.

[58]   Wang, J.; Li, H.; Liu, J.; Duan, Y.; Jiang, S.; Yan, S. *Journal of the American
       Chemical Society* **2003**, *125*, 1496–1497.

[59]   Salimi, A.; Yousefi, A. A. *Polymer Testing* **2003**, *22*, 699–704.

[60]   Piraux, L.; Hamoir, G.; Lee, M.-W.; Ferain, E.; Jonas, A. M.; Huynen, I.; Med-
       ina, J. D. L. T. *Applied Physics Express* **2011**, *4*, 115001.

[61]   Piraux, L.; Hamoir, G.; Encinas, A.; De La Torre Medina, J.; Abreu Araujo, F.
       Journal of Applied Physics **2013**, *114*, 123907.

[62]   Li, M.; Wondergem, H. J.; Spijkman, M.-J.; Asadi, K.; Katsouras, I.; Blom,
       P. W. M.; de Leeuw, D. M. *Nat Mater* **2013**, *12*, 433–438.

[63]   Kochervinskii, V. V. *Russian Chemical Reviews* **1996**, *65*, 865.

[64]   Peng, Y.; Wu, P. *Polymer* **2004**, *45*, 5295–5299.

[65]   Lanceros-Méndez, S.; Mano, J. F.; Costa, A. M.; Schmidt, V. H. *Journal of
       Macromolecular Science, Part B* **2001**, *40*, 517–527.

[66] Yang, D.; Tornga, S.; Orler, B.; Welch, C. *Journal of Membrane Science* **2012**, *409*, 302–317.

[67] Tashiro, K.; Itoh, Y.; Kobayashi, M.; Tadokoro, H. *Macromolecules* **1985**, *18*, 2600–2606.

[68] Bormashenko, Y.; Pogreb, R.; Stanevsky, O.; Bormashenko, E. *Polymer Testing* **2004**, *23*, 791–796.

[69] Le Bouëdec, A.; Betz, N.; Esnouf, S.; Le Moël, A. *Nuclear Instruments and Methods in Physics Research Section B: Beam Interactions with Materials and Atoms* **1999**, *151*, 89–96.

[70] Sakata, J.; Mochizuki, M. *Thin Solid Films* **1991**, *195*, 175–184.

[71] Martins, P.; Lopes, A. C.; Lanceros-Mendez, S. *Progress in Polymer Science* **2014**, *39*, 683–706.

[72] cuscito, O. elaboration de membranes PVDF-beta par attaque de traces et fonctiannalisation specifique des nanopres., Ph.D. Thesis, ecole polytechnique, 2008.

[73] Ndong, G.; Lizana, A.; Garcia-Caurel, E.; Paret, V.; Melizzi, G.; Cattelan, D.; Pelissier, B.; Tortai, J.-H. *Applied Optics* **2016**, *55*, 3323–3332.

[74] Agarwal, N.; Yoon, J.; Garcia-Caurel, E.; Novikova, T.; Vanel, J.-C.; Pierangelo, A.; Bykov, A.; Popov, A.; Meglinski, I.; Ossikovski, R. *Optics Letters* **2015**, *40*, 5634–5637.

[75] Chanmal, C.; Jog, J. *Express Polymer Letters* **2008**, *2*, 294–301.

Appendix A

Résume these

La polyvalence de la technique de track-etching a permis d'étudier plus avant l'effet piézoélectrique direct et indirect d'un film polarisé en poly(fluorure de vinylidène) PVDF en créant des membranes nanostructurées hybrides de nanofils de nickel (Ni NWs)/PVDF.

Le procédé de fabrication de la membrane hybride nécessite plusieurs étapes: i) irradiation aux ions lourd et formation de traces latentes dans le polymère, ii) révélation des traces latentes par attaque chimique, iii) dépots d'électrodes en or et iv) électrodéposition des nanofils de nickel. La diamètre final du nanofil est autour de 60 nm. Sa longueur maximale correspond à l'épaisseur de la membrane. Elle peut être variée suivant le temps d'électrodéposition.

Les propriétés magnétiques du nanofil de nickel, telle que la magnétorésistance anisotrope (AMR), ont été exploitées afin d'étudier la réponse de l'aimantation à la déformation mécanique de la matrice PVDF. En particulier, les déformations ont été induites soit par contrainte thermomécanique, soit par contrainte électro-mécanique (effet piézoélectrique indirect). L'état d'aimantation dans le nanofil de nickel est décrit par l'équation de l'énergie ferromagnétique total comprenant le couplage de Zeeman, l'énergie d'anisotropie et l'énergie magnéto-élastique. Dans le cas d'une température différente de la température ambiante ou d'un champ électrique appliqué à la membrane piézoélectrique, la minimisation de l'énergie totale permet de retrouver l'amplitude et la direction d'application de la contrainte mécanique exercée à l'échelle nanométrique par la matrice PVDF sur le nanofil unique. L'angle d'application de la contrainte a été trouvé autour de 73 degré, ce qui correspond à la condition de contrainte anisotrope autour du nanofil. Le résultat a été confirmé en tournant l'axe du nanofil vers la direction d'application de la contrainte. Plus le nanofil est proche de 73 degré, plus la condition d'anisotropie se réduit.

Une résistance exceptionnelle de la réponse piézoélectrique directe du film PVDF polarisé à l'irradiation, telle que l'irradiation aux ions-lourds accélérés et

aux électrons (domaine de doses < 100kGy) a été observée. Mise à part la conservation de la réponse piézoélectrique, les défauts engendrés par l'irradiation dans ce domaine de doses (scissions de chaines et réticulations) ont eu un impact significatif sur la structure du matériau polymère. L'ensemble de ces défauts, les uns prépondérants en-dessous de la dose-gel (aux alentours de 10kGy), les autres au-dessus, forme une compensation d'effets antagonistes qui mènent à une réponse piézoélectriquectrique globalement inchangée. Les plus courtes chaines polymères, obtenues à faible dose (en-dessous de la dose-gel du PVDF), permettent la réorganisation du polymère et, par conséquent, une augmentation de la phase cristalline. Les techniques de caractérisation, tel que la calorimétrie différentielle à balayage et la diffusion des rayons X, ont montré que l'augmentation de la cristallinité est relatif à la phase beta responsable de la piézoélectricité du polymère. Malgré la phase beta additionnelle, la réponse piézoélectrique du polymère reste constante puisqu'il n'y a pas eu de repolarisation des échantillons.

Stimulé par la grande résistance du PVDF à l'irradiation en termes de réponse piézoélectrique, l'idée a été d'exploiter, en vue d'une application dans la récupération d'énergie, le réseau de nanofils de nickel inclus dans la membrane en PVDF polarisé pour étudier l'influence des nanofils de nickel sur l'efficacité piézoélectrique. La présence du réseau de nanofils de nickel mène à un accroissement non-négligeable de l'efficacité piézoélectrique par rapport aux membranes juste attaquées (membranes poreuses vides). En effet, la présence de nano-pores et la température d'attaque chimique (65°C) mène à une diminution considérable de l'efficacité piézoélectrique du polymère. Reliée à la présence des nanofils, une augmentation de la permittivité diélectrique dans le PVDF nanostructuré a également été enregistrée. Une polarisation interfaciale entre les nanofils de nickel et la matrice PVDF pourrait expliquer cette valeur accrue par rapport au PVDF nanoporeux sans nanofils.

Titre : Synthèse de films hybrides en Ni/PVDF piezoélectriques nanostructurés par faisceau d'ions lourds accélérés: une étude de la réponse piezoélectrique directe et indirecte

Mots clés : piezoélectricité, magnetoresistance, irradiation, nanofils, récupération d'énergie

Résumé : La polyvalence de la technique de track-etching a permis d'étudier plus avant l'effet piezoélectrique direct et indirect d'un film polarisé en poly(fluorure de vinylidène) PVDF en créant des membranes nanostructurées hybrides de nanofils de nickel (Ni NWs)/PVDF. Les propriétés magnétiques du nanofil de nickel, telle que la magnétorésistance anisotrope (AMR), ont été exploitées afin d'étudier la réponse de l'aimantation à la déformation mécanique de la matrice PVDF. La sensibilité d'un nanofil unique a permis de déterminer l'amplitude et la direction de la contrainte mécanique exercée à l'échelle nanométrique par la matrice PVDF induites par contrainte thermo-mécanique ou électromécanique. La résistance exceptionnelle de la réponse piezoélectrique directe du film PVDF polarisé à l'irradiation, telle que l'irradiation aux ions-lourds accélérés et aux électrons (domaine de doses < 100kGy) a été observée. Mis à part la conservation de la réponse piezoélectrique, les défauts engendrés par l'irradiation dans ce domaine de dose (scissions de chaines, augmentation de phase cristalline β, réticulations) ont eu un impact significatif sur la structure du matériau polymère. Stimulé par la grande résistance du PVDF à l'irradiation en termes de réponse piezoélectrique, l'idée a été d'exploiter, en vue d'une application dans la recuperation d'énergie, le réseau de nanofils de nickel inclus dans la membrane en PVDF polarisé pour étudier l'influence des nanofils de nickel sur la l'efficacité piezoélectrique. La présence du réseau de nanofils de nickel mène à un accroissement nonnégligeable de l'efficacité piezoélectrique. Une polarisation interfaciale entre les nanofils de nickel et la matrice PVDF pourrait expliquer cette valeur accrue par rapport au PVDF nanoporeux sans nanofils.

Title : Piezoelectric nanostructured Ni/PVDF hybrid film synthesized from swift-heavy ions irradiation: a direct and indirect piezoelectric response study

Keywords : piezoelectricity, , magnetoresistance, irradiation, nanowires, harvesting energy

Abstract : The versatility of the track-etching technique has allowed to investigate deeper the direct and inverse piezoelectric effect of a polarized Poly(vinylidene fluoride) (PVDF) film in building nanostructured hybrid Nickel nanowires (Ni NWs)/ PVDF membrane. The magnetic properties of the Ni NW, such as anisotropic magneto resistance (AMR), are exploited to investigate the response of the magnetization to a mechanical deformation of the PVDF matrix. The sensitivity of the single NW has allowed to determine the amplitude and direction of a mechanical stress exerted at the nano-scale by the PVDF matrix induced by thermo-mechanical or an electro-mechanical. The outstanding resistance of the direct piezoelectric response of polarized PVDF film to radiation, such as SHI and e-beam, (doses range < 100kGy) was reported. Beyond the conservation of the piezoelectric response, in this dose range, irradiation defects (chain scissions, increase of the crystalline β -phase, crosslinking) had a significant impact on the polymer material. Motivated by the high radiation resistance of the PVDF in terms of piezoelectric response, the idea was to exploit Ni NWs array embedded in the polarized PVDF membrane to study the influence of the Ni NWs on the piezoelectric response in view of harvesting energy application. The presence of the Ni NWs array leads a non-negligible increase of the piezoelectric efficiency. An interfacial polarization between the Ni NWs and the PVDF matrix could explain the higher efficiency value respect to nanoporous PVDF, without NWs.